ENHANCING THERMOPHOTOVOLTAICS VIA SELECTIVE THERMAL EMITTERS AND RADIATIVE THERMAL MANAGEMENT

A Dissertation

Submitted to the Faculty

of

Purdue University

by

Zhiguang Zhou

In Partial Fulfillment of the

Requirements for the Degree

of

Doctor of Philosophy

December 2019

Purdue University

West Lafayette, Indiana

THE PURDUE UNIVERSITY GRADUATE SCHOOL
STATEMENT OF DISSERTATION APPROVAL

Dr. Peter Bermel, Chair

School of Electrical and Computer Engineering

Dr. Andrew Weiner

School of Electrical and Computer Engineering

Dr. Minghao Qi

School of Electrical and Computer Engineering

Dr. Amy Marconnet

School of Mechanical Engineering

Approved by:

Dr. Dimitrios Peroulis

Head of Electrical and Computer Engineering

To my family

ACKNOWLEDGMENTS

When I first started my study at Purdue six years ago, little did I know about the challenge I was facing. In retrospect, I was fortunate to work, from the very beginning, with someone who is truly willing to provide guidance and care. Here, I'd like to extend my sincere gratitude to my thesis advisor, Prof. Peter Bermel, for his mentorship and unconditional supports. His focus on practical applications shapes my taste of research. His unwavering academic integrity enhances my ideals of scientific study. Over the years, he provided detailed guidance, as well as sufficient degree of freedom for independent research. I also want to thank him for offering the best advice and support on my career path, especially when facing difficulties and tough choices. It is truly my privilege to be able to work with Prof. Bermel.

I want to thank Prof. Andrew M. Weiner, Prof. Minghao Qi and Prof. Amy Marconnet for joining my committee and providing constructive suggestions and technical supports to my research. In addition, your classes and lectures better prepared me in related areas.

Next, I would like to acknowledge my collaborators. I want to thank Prof. Muhammad A. Alam, Prof. Vladimir M. Shalaev, Prof. Haiyan Wang, Prof. Gary J. Chen from Purdue University. Prof. Yi Cui from Stanford University, Dr. Myles A. Steiner and Dr. Timothy Silverman from National Renewable Energy Laboratory and Dr. Urcan Guler at United Technologies Research Center. Some of the most critical results in my research would not be acquired without your help.

I also want to say a big thank you to my colleagues and lab mates. The friendships we built over the years are what I cherish most.

To my lab mates from Bermel's group - Yubo Sun, Ze Wang, Dr. Enas Sakr, Dr. Haejun Chung, Dr. Roman Shugayev, David Kortge, Allison Perna, Elizabeth Grubbs, Sayan Roy, Oluseye Akomolede, Haimabati Dey, the weekly group meeting

is what I look forward to most. The inspiring discussions and collaborations are invaluable.

To my colleagues and peers - Hao Tian, Harsha Reddy, Xin Jin, Reza Asadpour, Omar Yehia, Tianran Liu, Cindy Karina, Dr. Menglong Hao, Dr.Pingge He, Dr. Xingshu Sun, Dr. Xufeng Wang, Xuejing Wang, Dr. Shengyu Jin, Md. Tahir Patel, Md. Ryyan Khan, I'm grateful to have so much support from so many ingenious minds outside my own group.

To my ECE and Birck family - Matt Golden, Elisheba VanWinkle, Mary Jo Totten, Kyle Corwin, Dan Hosler, Dave Lubelski, Kenny Schwartz, Jerry Shepard, Bill Rowe, Guy Telesnicki, Joon Park, Tim Miller, thanks for your help in all aspects of my life at Purdue and Birck Nanotechnology Center.

Finally and most importantly, I want to thank my family. To my parents and grandparents, I want to thank them for their strongest supports. My deceased grandfather, as an engineer himself and a provider to the family, is always my role model. I must thank my beloved wife for her enduring love. She is my source of comfort and courage. She stood by my side in the best days of our lives as well as the darkest hours. This work would never be done without her.

TABLE OF CONTENTS

Page

Page

LIST OF TABLES

LIST OF FIGURES

Figure Page

Figure Page

Figure Page

Figure Page

Figure Page

Figure Page

Figure Page

Figure Page

ABSTRACT

Zhou, Zhiguang. Ph.D., Purdue University, December 2019. Enhancing Thermophotovoltaics via Selective Thermal Emitters and Radiative Thermal Management. Major Professor: Peter Bermel.

Thermal radiation is a fundamental heat transfer process, with certain basic aspects still not fully understood. Furthermore, tailoring its properties has potential to affect a wide range of applications, particularly thermophotovoltaics (TPV) and radiative cooling.

TPV converts heat into electricity using thermal radiation to illuminate a photovoltaic diode, with no moving parts. With its realistic efficiency limit up to 50% (heat source at 1200 °C), TPV has garnered substantial interest. However, state-of-the-art TPV demonstrations are still well below theoretical limits, because of losses from generating and efficiently converting or recycling thermal radiation. In this thesis, tailored integrated photonic crystal structures are numerically simulated to enhance the efficiency of solar TPV. Next, a high-temperature thin-film Si-based selective absorber and emitter is designed, fabricated and experimentally characterized. It exhibits great potential to open up new applications, as it lends itself to large-scale production with substantial mechanical flexibility and excellent spectral selectivity for extended time periods, even when operating under high operating temperatures (600 °C) for up to 6 hours, with partial degradation after 24 hours. To perform this high-temperature characterization, an emittance measurement setup has been built; its performance agrees well with numerical simulations.

Second, a unique passive cooling mechanism known as radiative cooling is developed to reduce the operating temperature of the photovoltaic diode. The significant effect of radiative cooling as a complement for an all-passive-cooling TPV system

is proposed and numerically analyzed under a range of conditions. Furthermore, an outdoor experiment has been performed to demonstrate the effect of radiative cooling on a concentrating photovoltaic system, which can potentially be applied to the thermal management of a TPV system. In summary, this work paves the way towards the development of reliable, quiet, lightweight, and sustainable TPV and radiatively cooled power sources for outdoor applications.

1. INTRODUCTION

Human activities, including transportation and manufacturing, produce a huge amount of waste heat. According to a study by Lawrence Livermore National Laboratory, 68% of the raw energy was wasted in 2018 [1]. However, a substantial amount of the waste can be recycled or managed for applications such as power generation and thermal management. To convert heat into electricity, various technologies have been developed. A promising candidate among them is thermophotovoltaics (TPV). TPV converts heat into electricity via thermal radiation and photovoltaic effect. Since its first introduction by Henry Kolm [2] in 1956 and by Pierre Aigrain in 1961 [3], TPV has attracted a lot of research effort in achieving higher performance. Furthermore, the technology of TPV can be extended to harvesting energy from the ultimate renewable heat source, the sun. The technology known as solar TPV (STPV), converts most of the solar spectrum into heat and then generate electricity via TPV mechanism [4]. While controlling thermal radiation is critical for TPV performance, thermal management of the PV diode is equally important, as the conversion efficiency and reliability of a PV diode degrades with temperature. Fortunately, there exists a passive cooling method known as radiative cooling. By properly utilizing the transmission window of the sky, radiative cooling can be an important complimentary cooling strategy for thermal management.

In this chapter [1], TPV and STPV systems and their basic concepts will be discussed in detail. This includes principles of selective thermal emitters and selective

[1] Adapted from:

- Z. Zhou, E. Sakr, Y. Sun, and P. Bermel, "Solar thermophotovoltaics: Reshaping the solar spectrum," *Nanophotonics*, vol. 5, no. 1, 2016.
- X. Sun, Y. Sun, Z. Zhou, M. A. Alam, and P. Bermel, "Radiative sky cooling: Fundamental physics, materials, structures, and applications," *Nanophotonics*, vol. 6, no. 5, 2017.

solar absorbers, photovoltaic effect and system integration of TPVs. Following that is a review of radiative cooling, including development of radiative coolers and their applications in various scenarios.

1.1 Thermophotovoltaics (TPV) and Solar Thermophotovoltaics (STPV)

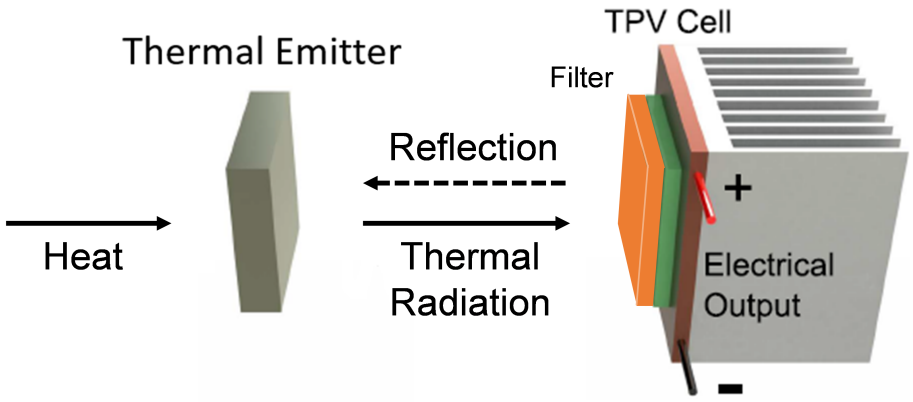

Fig. 1.1. The schematics of a typical TPV system that consists of a thermal emitter that converts input heat into thermal radiation, a PV diode (TPV cell) that converts above-bandgap radiation into electricity and a filter that recycles the low energy radiation. Adapted from [5]

A TPV system, as shown in Fig. 1.1, typically consists of three components: (1) A thermal emitter, (2) A band-pass filter and (3) A low bandgap (E_g) PV diode. The thermal emitter is typically in direct contact with the heat source. At elevated temperature, thermal emitters give away thermal radiation P_{rad}, following Planck's law:

$$P_{rad} = A\int_0^\infty d\lambda \epsilon(\lambda) I_{BB}(\lambda, T) = A\int_0^\infty d\lambda \frac{2\pi hc^2}{\lambda^5}\frac{\epsilon(\lambda)}{e^{\frac{hc}{\lambda kT}}-1}, \tag{1.1}$$

where A is the surface area of the thermal emitter with emittance $\epsilon(\lambda)$, and T is its

temperature. $I_{BB}(\lambda, T)$ is the blackbody spectrum at T; λ is the wavelength; h is the Planck constant; k is the Boltzmann constant; c is the speed of light in vacuum.

Typically, photons of thermal radiation carry a broad band distribution of energy (as indicated by Eq. 1.1). However, only those above the E_g of the PV diode can be converted into electricity P_{pv}. The conversion efficiency of a TPV system can be defined as:

$$\eta_{tpv} = \frac{P_{pv}}{P_{rad}} \tag{1.2}$$

To minimize wasted energy and therefore increase the conversion efficiency, spectrally selective emitters that exhibits enhanced thermal radiation above PV diode bandgap (increase P_{pv} in Eq. 1.2) and suppressed radiation below (decrease P_{rad} in Eq. 1.2) are introduced. In addition, a band-pass filter placed between the emitter and the PV diode can further reduce the loss due to sub-bandgap radiation. The filter not only blocks the transmission of sub-bandgap photons, but also reflects them back to the emitter where reabsorption happens. Such mechanism is known as photon recycling in TPV systems. As a result, the recycled power P_{re} should be subtracted from P_{rad}, leading to:

$$\eta_{tpv} = \frac{P_{pv}}{P_{rad} - P_{re}} \tag{1.3}$$

For effective photon recycling, it is essential to minimize the distance between the emitter and the filter. Because the view factor from the emitter to the filter determines the recycled power P_{re}. In most reported TPV structures, the filter is attached to the PV diode, as shown in Fig. 1.1.

PV diodes convert the incoming radiation into electricity via photovoltaic effect. The converted power can be calculated as:

$$P_{pv} = I_{sc} V_{oc} FF, \tag{1.4}$$

where I_{sc} is the short-circuit current (current at 0 voltage); V_{oc} is the open-circuit voltage (voltage at 0 current) and FF is the fill factor, the ratio of peak output power to the product of I_{sc} and V_{oc}. P_{pv} calculated by Eq. 1.4 is therefore the peak output power from the PV diode.

Common solar cell diodes (e.g. Si PV diode with $E_g = 1.1$ eV) are not optimal for TPV applications. This is because the peak wavelength of a typical thermal emitter at a temperature of 1500 K would be around 1.9 μm (0.65 eV). However, a bandgap too low suppresses the energy of the converted electrons, resulting in V_{oc} being too low. It is found that low-bandgap PV diodes with an optimal bandgap around 0.7 eV [6], such as GaSb or InGaAs, are preferred for TPV systems.

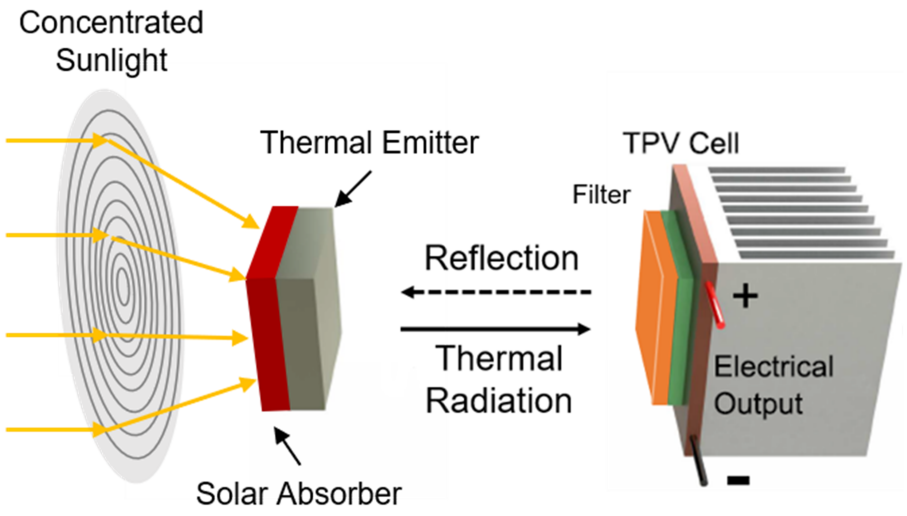

Fig. 1.2. The schematics of a typical solar thermophotovoltaic (STPV) system. In addition to components generally used in TPVs, a solar concentrator is placed at the front to focus the incident sunlight. Furthermore, a selective solar absorber, converting concentrated sunlight into heat, is attached to the thermal emitter.

One specific category of TPV systems is solar TPV (STPV), a technology that uses solar energy as heat source. In such systems, a solar absorber converts solar irradiance into heat, as shown in Fig. 1.2. The thermal emitter is in direct contact

with the solar absorber, so that heat is conducted at minimal loss. In order to reach high operating temperature, thus high efficiency, solar concentration is very necessary. In most STPV systems, solar concentrators like Fresnel lenses are placed in front of the solar absorber, as shown in Fig. 1.2. Given that there are two more components added to the system, the conversion efficiency of STPV is expressed as:

$$\eta_{stpv} = \eta_o \eta_t \eta_{tpv}, \tag{1.5}$$

where η_o is the optical efficiency of the solar concentrator; η_t is the thermal transfer efficiency of the solar absorber, quantifying how much incident solar irradiance can be converted into heat.

The theoretical efficiency limit of such a TPV system is set by the Carnot limit, and the corresponding STPV efficiency can be as high as 85% under full solar concentration [7]. However, the best TPV efficiency reported to date is about 29.1% [8] and the world record of STPV efficiency is only 6.8% [9]. The large discrepancy in efficiency is mainly due to (1) sub-bandgap photon from the emitter; (2) sub-optimal view factor from the emitter to the PV diode; (3) loss at the PV diode and (4) thermal re-radiation loss at the solar absorber (for STPV systems specifically). Most of the loss mechanism listed can be alleviated via engineering. Therefore, TPV is still a field of research full of challenges and potentials.

1.1.1 Selective Thermal Emitters

One approach to improve the TPV performance is reducing sub-bandgap loss by using spectral-selective emitters [10]. As shown in Fig. 1.3, the emittance spectrum $\epsilon(\lambda)$ of the thermal emitter should meet three requirements: (1) near-zero emittance for sub-bandgap photons, (2) near-unity emittance for photons with energy higher than the bandgap (E_g) of the PV diode and (3) low emittance for photons with energy much higher than E_g. The first requirement reduces sub-bandgap loss. The second enhances the power that can be potentially generated from the PV diode. The third

reduces thermalization loss from the PV diode. Therefore, an ideal selective emitter should have a top-hat shaped emittance spectrum that has peak value of 1 within a narrow bandwidth [11]. Because most thermal emitters operate at $1000 - 2000$ K, thermalization loss usually has less impact on the efficiency than sub-bandgap loss. Therefore, it is more important to have high selectivity (sharp cut-off in emittance spectrum) that matches with E_g. The bandwidth of such top-hat emittance spectrum has an optimal value. For example, it is found that when the emitter is at 2000 K and an ideal PV diode is used, the optimal bandwidth is 0.07 eV [11].

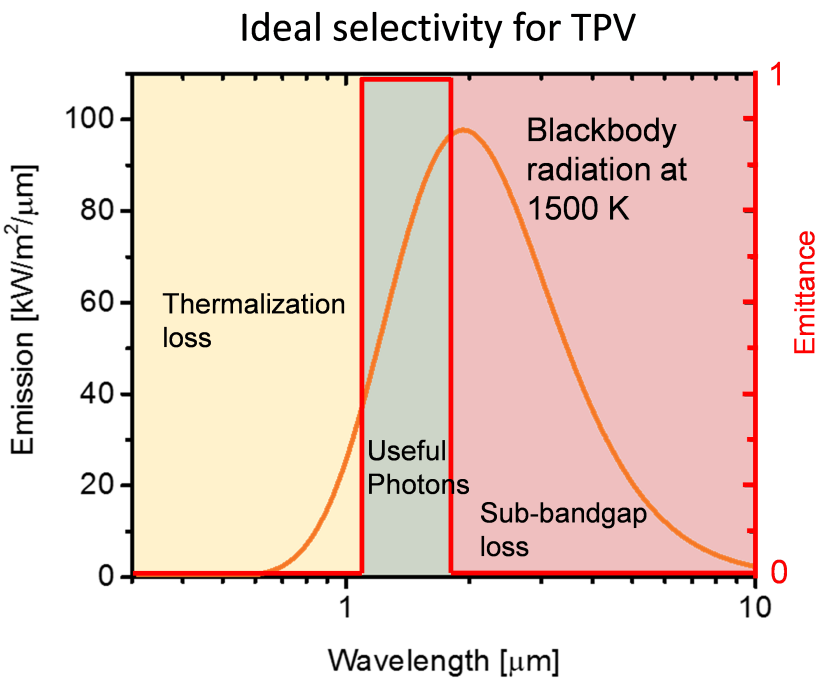

Fig. 1.3. Ideal emittance of a selective thermal emitter. For energy below the bandgap of the PV diode, $\epsilon(\lambda)$ should be close to zero to minimize sub-bandgap loss. For a bandwidth above the bandgap, $\epsilon(\lambda)$ should be close to unity to maximize the converted electric power. For energy much above the bandgap, $\epsilon(\lambda)$ should be close to zero as well to minimize thermalization loss.

Rare-earth Thermal Emitters

To date, significant efforts have been put into the pursuit of highly selective thermal emitters that can improve TPV efficiency. Among many different types of thermal emitters, rare-earth emitters are developed in early stage of TPV research thanks to their intrinsic selective emission [12]. Oxides based on rare-earth elements, such as Er_2O_3 and Yb_2O_3, have been fabricated and characterized [13–15]. It has been found that Yb_2O_3 can be paired with Si PV diode [14] (as shown in Fig. 1.4 (a)) while Er_2O_3 matches better with lower bandgap PV diodes such as Ge [13].

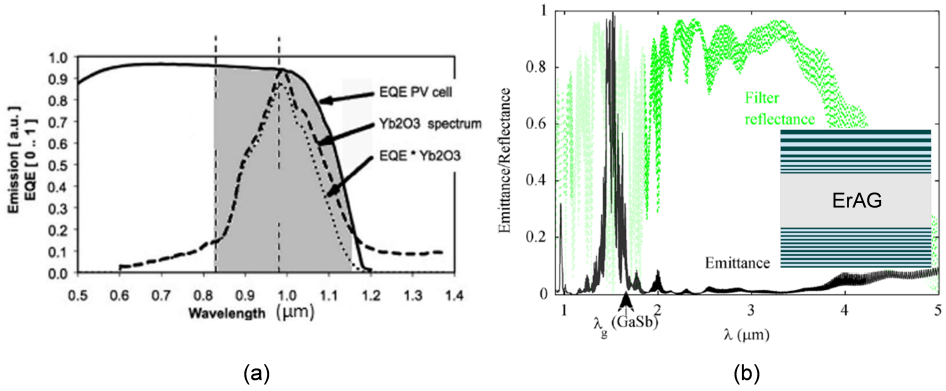

Fig. 1.4. Rare-earth based selective thermal emitters. (a) the thermal emittance of a Yb_2O_3 thermal emitter in comparison with the external quantum efficiency (EQE) of a Si PV diode [14]. (b) The calculated thermal emittance (black curve) of a 1D photonic crystal (PhC) integrated Er doped aluminum garnet (ErAG) emitter. The reflectance of the multilayer at the front is shown in green curve for comparison. The inset shows the schematics of the emitter cross-section. Panel (b) is adapted from [16].

In addition to oxides, rare-earth doped selective emitters [17, 18] have been developed as well. However, rare-earth based thermal emitters still exhibit large parasitic emission due to host materials or substrates. In order to further improve the spectral selectivity, photonic structures that can tailor the bulk emission property are proposed to be integrated [16]. Significant improvement has been reported, as shown in Fig. 1.4 (b), when the metallic back reflectors is replaced by a less lossy quarter-wave

stack (QWS), and a chirped dielectric filter that has ultra-wide stop band is added on top [16]. Other than suppressing parasitic emissions, enhancement of above-bandgap emission can be achieved via the metasurface back reflector proposed in Ref. [18], following generalized Snell's law [19].

Nanophotonic Thermal Emitters

Other than bulk materials, artificial photonic structures have been developed to tailor the emittance of bulk materials by modifying the photonic density of states [20, 21]. For example, photonic crystal (PhC) emitters [11, 22–25], metamaterial emitters [26] and plasmonic emitters [27, 28] have been designed and characterized to have strong selectivity.

1D PhCs have been proposed to be used as top or bottom layer similar to the rare-earth thermal emitter discussed above. It is found that such additional 1D structures can improve bulk emission properties for semiconductor materials, such as Si (shown in Fig. 1.5 (a) and (b)) and Ge, and make them suitable for TPV applications [23]. 2D PhCs, such as a square lattice of micro/nano-scale air holes on metallic bulk material (shown in Fig. 1.5 (c)), are extensively studied as a promising candidate for thermal emitters [20]. It should be noted as well, as shown in Fig. 1.5 (c), that the thermal emittance of 2D PhC can be adjusted by changing structural parameters like hole depth, hole radius and periodicity [20]. 3D PhCs, though more complicated in terms of fabrication, have also been demonstrated as efficient thermal emitters [29, 30].

Metamaterial is another potential candidate among nanophotonic thermal emitters [31]. Certain plasmonic resonances supported by the structure give rise to perfect absorption at corresponding wavelengths. This in turn leads to near-unity emittance at those wavelengths, following Kirchhoff's law of thermal radiation [32]. By including a series of sub-cells that have slightly different structures into one unit cell of a large array, multiple resonance peaks are stacked together. As shown in Fig. 1.5 (d),The net result is a band of high emittance followed by a clear cut-off [26].

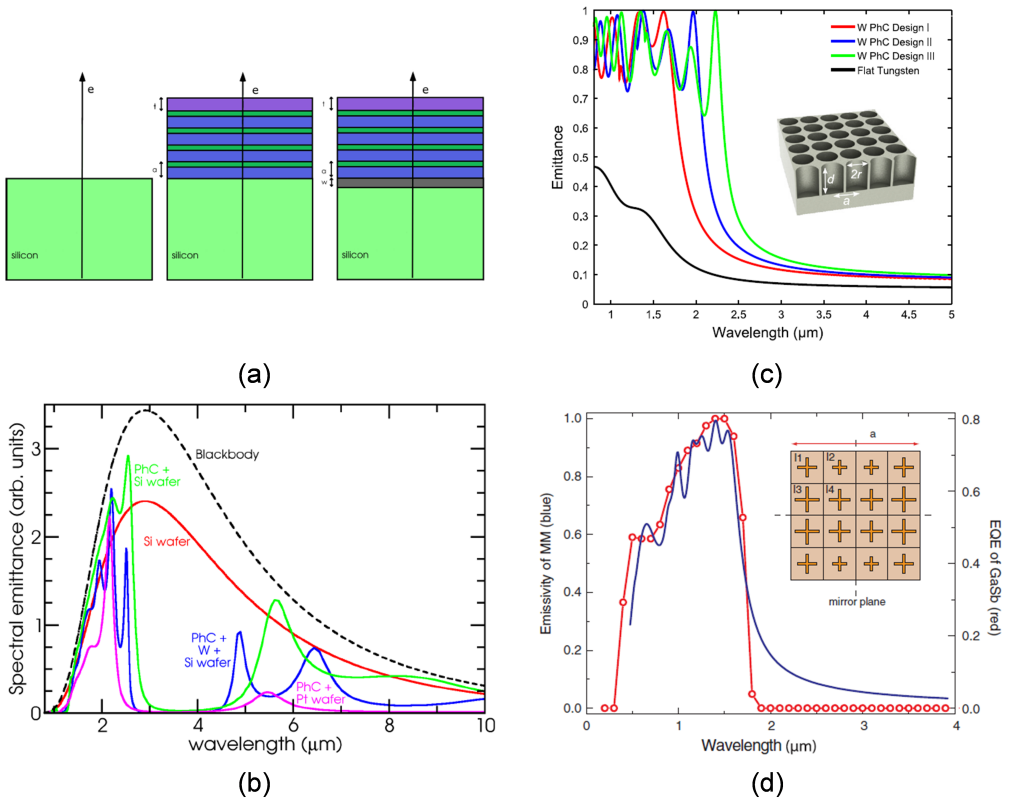

Fig. 1.5. Nanophotonic selective thermal emitters. (a) Schematics of Si selective emitter enabled by 1D PhC front layers. (b) The resulting emittance spectrum of the structures depicted in (a). Panel (a) and (b) reproduced from [23]. (c) Simulated emittance spectrum from various W 2D PhC (design I: $r = 0.45$ μm, $a = 1.10$ μm, $d = 1.50$ μm; design II: $r = 0.55$ μm, $a = 1.30$ μm, $d = 2.10$ μm; design III: $r = 0.625$ μm, $a = 1.40$ μm, $d = 2.80$ μm), showing great degree of freedom in tuning cut-off frequencies by varying PhC structures. Panel (c) reproduced from [20]. (d) Emittance spectrum (blue curve) form a metamaterial based thermal emitter (unit cell shown in inset). It matches well with the EQE spectrum (red curve) of a GaSb PV diode. Panel (d) reproduced from [26].

A critical requirement of thermal emitters is performance stability under high temperature. Such constraints limit the materials to be used. Specifically, refractory metals, such as tungsten (W), tantalum (Ta) and molybdenum (Mo) have garnered interests [6,29,33,34]. Though the melting points of bulk refractory metals are higher

than the operation temperature of TPV or STPV, the degradation of nanophotonic structures made of them can happen at a much lower temperature. Such degradation may include oxidation [35], recrystallization [36, 37] and surface diffusion [38, 39]. As a result, the optical performance including peak wavelengths and spectral selectivity may change. Therefore, enhancing the thermal stability of thermal emitters is a critical challenge. In existing literature, there are several strategies addressing this challenge. For example, protective layers of hafnium oxide or silicon dioxide conformally coated over the nano-structures can effectively prevent surface diffusion [35, 40, 41]. In addition to refractory metals, refractory plasmonic materials like titanium nitride (TiN) are proved to be promising for high-temperature applications [42].

1.1.2 Selective Solar Absorbers

As mentioned in Section 1.1, one specific application of TPV is STPV. Concentrated solar radiation is first converted into heat by a solar absorber. As its temperature increases, part of the absorbed power is dissipated back to the environment through thermal radiation. Such re-radiation loss is one of the main bottle necks of STPV efficiencies. To capture the physics of the energy conversion at the solar absorber, a figure of merit known as the thermal conversion efficiency (η_t) is developed:

$$\eta_t(T) = \overline{\alpha}(T) - \frac{\sigma\overline{\epsilon}(T)T^4}{CI_{solar}}, \tag{1.6}$$

where T is the temperature of the solar absorber; C is the solar concentration factor; I_{solar} is the intensity of the unconcentrated sunlight; σ is the Stefan-Boltzmann constant; $\overline{\alpha}(T)$ is the spectrally averaged solar absorptance defined as:

$$\overline{\alpha}(T) = \frac{\int d\lambda \alpha(\lambda, T) I_{AM1.5D}(\lambda)}{\int d\lambda I_{AM1.5D}(\lambda)}, \tag{1.7}$$

where $\alpha(\lambda, T)$ is the absorptance of the solar absorber, and $\alpha(\lambda, T) = \epsilon(\lambda, T)$ under

thermal equilibrium according to Kirchhoff's thermal radiation law [32]. $I_{AM1.5D}(\lambda)$ is the AM1.5D direct and circumsolar intensity spectrum. AM1.5D, with its total intensity of 900 W/m^2, is highly representative of the direct part of the solar spectrum that can be utilized for concentration.

$\overline{\epsilon}(T)$ is the spectrally averaged thermal emittance defined as:

$$\overline{\epsilon}(T) = \frac{\int d\lambda \epsilon(\lambda, T) I_{BB}(\lambda, T)}{\int d\lambda I_{BB}(\lambda, T)}, \tag{1.8}$$

where $I_{BB}(\lambda, T)$ is defined in Eq. 1.1.

Apparently from Eq. 1.6, high thermal transfer efficiency (η_t) requires high solar absorptance and low thermal emittance, especially when the applications are at high temperature and low solar concentration. To achieve this, as shown in Fig. 1.6, a spectrally selective solar absorber should be used. The emittance spectrum of a selective solar absorber should exhibit high emittance in the solar spectrum range and low emittance beyond, so that both high $\overline{\alpha}(T)$ and low $\overline{\epsilon}(T)$ are achieved at the same time. This is possible because a typical selective absorber operates at a temperature much lower than the sun, ensuring that the solar spectrum $I_{AM1.5D}(\lambda)$ and absorber blackbody radiation $I_{BB}(\lambda, T)$ are separated. As temperature increases, $I_{BB}(\lambda, T)$ overlaps more with $I_{AM1.5D}(\lambda)$, and it becomes harder to achieve high η_t. In this case, solar concentration (C) can be increased to compensate the thermal re-radiation loss, as shown in Eq. 1.6. However, as a matter of fact, it is preferred to keep low solar concentration (< 100 sun) in real applications, as high concentrations require more complicated dual-axial solar tracking. Therefore, a better solution is to make solar absorbers more selective. In the next few sections, different types of selective solar absorbers are reviewed in detail.

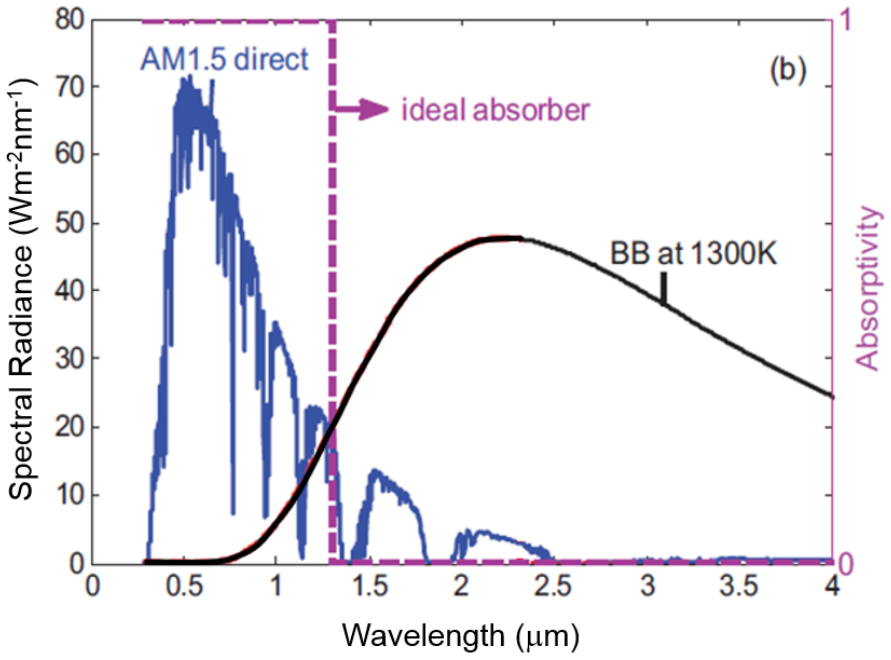

Fig. 1.6. Absorptance (absorptivity) of an idea selective solar absorber (purple dashed curve). Its steep cut-off in the overlapping region of solar spectrum (blue curve) and blackbody emission spectrum (black curve) ensures both strong solar absorption and weak thermal re-radiation loss [33].

Metal-dielectric Composite Selective Solar Absorbers

Metal-dielectric composite solar absorbers consist of at least a cermet layer and a back reflector. Cermets are composite materials with metallic nanoparticles embedded in ceramic binders, such as alumina (Al_2O_3) [43], silicon dioxide (SiO_2), aluminum oxynitride (AlON) [44] and zirconium dioxide (ZrO_2) [45]. It is found that the absorptance spectrum of cermets can be tuned by the metallic nanoparticles [46]. To enhance solar absorption, a multi-layer structure of cermets with gradually increasing particle concentrations has been proposed [47]. Using a $Al^{sp} - AlON$ (Al sputtered in AlON binder) cermet solar absorber, a simplified double-layer structure yields $\eta_t = 86\%$ under 1 sun illumination and a temperature of 353 K [44]. For higher

temperature applications, it has been proposed through theoretical calculations that a graded-index multilayer consisting of W particles in alumina binder (shown in Fig. 1.7) can achieve up to $\eta_t = 85\%$ under 100 suns at 1000 K [48].

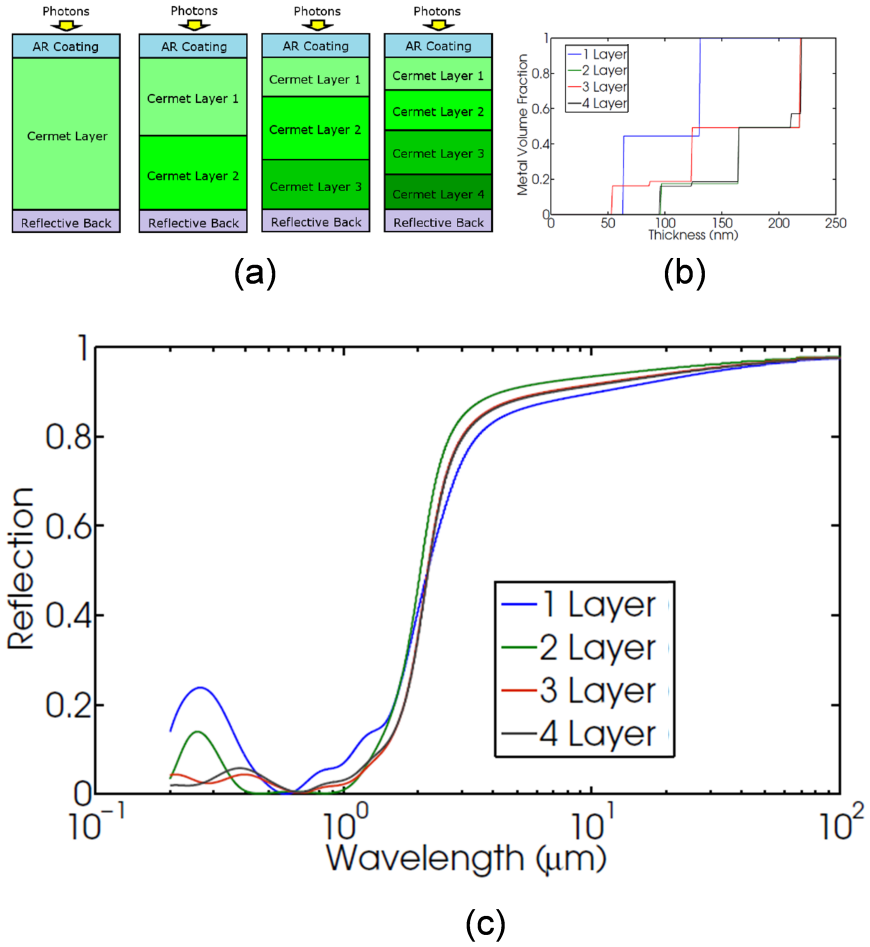

Fig. 1.7. Metal-dielectric composite selective solar absorber. (a) Schematics of cermet-based selective solar absorbers (W particles in alumina). (b) Varying metal volume fraction across the multilayer structure in (a). (c) Calculated reflectance (1 - absorptance) spectrum of the selective solar absorber depicted in (a). Panel (a) - (c) adapted from [48].

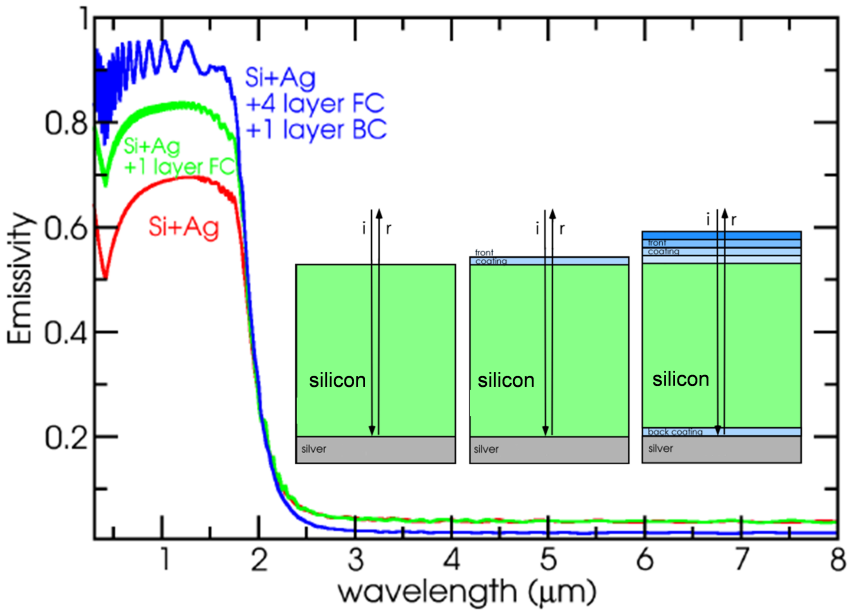

Fig. 1.8. Si-based semiconductor-metal tandem selective solar absorber. Calculated absorptance (emissivity) spectra of Si-Ag tandem absorber structures schematically depicted in the inset. Adapted from [23].

Semiconductor-metal Tandem Selective Solar Absorbers

Semiconductor is another type of material that has natural selective absorption, with strong absorption above the bandgap and low absorption below. In fact, when lightly doped and highly polished on surface, semiconductors are almost transparent to sub-bandgap photons. Similar to metal-dielectric composite absorbers, a back reflector (typically low-loss metal) is deposited on the back side of the semiconductor, forming a tandem. Some typical semiconductor materials used for solar absorbers are crystalline silicon (c-Si), amorphous silicon (a-Si) [49], germanium (Ge) and lead sulfide (PbS) [50–52]. A common issue of those semiconductor materials is the strong reflection at top surface due to their high refractive index. To reduce the reflection and therefore enhance above-bandgap absorption, an anti-reflection coating (ARC) is added on top. As shown in Fig. 1.8, by adding a four-layer front coating and a one-

layer back coating to a Si-Ag tandem solar absorber, the theoretical thermal transfer efficiency η_t can be as high as 82.2% at 1000 K and 100 suns concentration [23]. A simplified structure using 300 μm-thick commercialized double-side-polished Si wafer has been fabricated and characterized at operating temperatures. At 490 °C, a $\eta_t = 51.5\%$ has been reported [53]. More importantly, it has been found that the intrinsic carrier concentration, which increases with temperature, may greatly hamper the performance of semiconductor-metal tandem solar absorber. An effective solution is significantly reducing the thickness of semiconductor layer [53]. Therefore, using semiconductor thin films instead of wafers can be a very interesting approach to make high-performance selective solar absorber, as will be discussed in detail in Chapter 5.

Nanophotonic Selective Solar Absorbers

Following Kirchhoff's thermal radiation law, strong selectivity in emittance is equivalent to strong selectivity in absorptance under thermal equilibrium. Therefore, nanophotonic structures that are proved to be effective as thermal emitters can be borrowed for making solar absorbers. For example, a 2D planar plasmonic structure (shown in Fig. 1.9 (a) and (b)) has been proposed to be used as a selective solar absorber and a selective thermal emitter simultaneously [27]. While its absorption peak in visible range collects concentrated sunlight, its IR peak provides thermal emission towards the PV diode [27]. 1D multilayer stack [54] and 1D grating structures [55] have both been studied as selective solar absorbers and shown great selectivity. As shown in Fig. 1.9 (c) and (d), 2D square-lattice PhCs on Ta has been successfully fabricated and characterized to have $\eta_t = 66.4\%$ at 1000 K under 100 suns concentration [33]. Further improvement may be achieved by an integrated PhC structure that combines a 1D multilayer stack with a 2D PhC [56]. For applications where high solar concentration is available, a nanoimprinted PhC based on Ta has been fabricated, showing $\eta_t = 82.8\%$ at 1500 K under 1000 suns concentration [57].

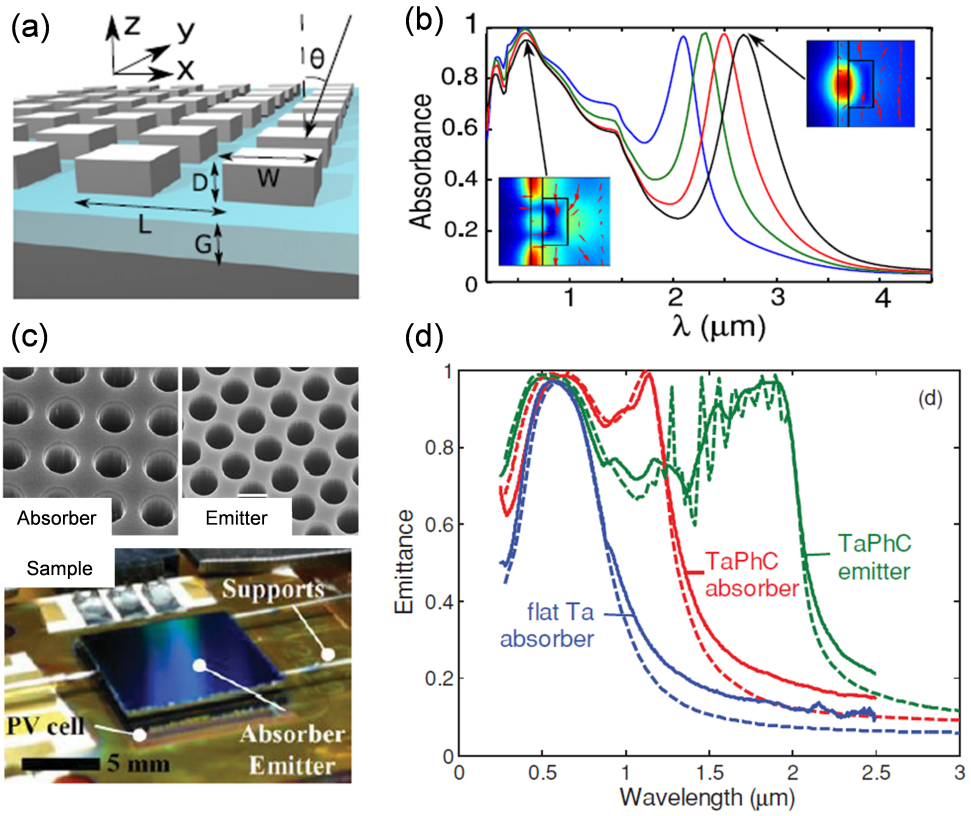

Fig. 1.9. Nanophotonic selective solar absorbers. (a) A 2D planar plasmonic selective solar absorber with refractory metal square patterns on dielectric thin film (blue region). (b) The calculated absorptance spectra of different structural parameters (width (W), depth (D), period (L) and dielectric thickness (G)). The strong visible absorption peak and mid-IR peak make it a unique selective surface that can serve as a solar absorber and an emitter simultaneously. Panel (a) and (b) are adapted from [27]. (c) 2D Ta PhC selective solar absorber and thermal emitter as a monolithic component. (d) The measured emittance spectra for both the emitter and the absorber in comparison with a flat Ta substrate. Panel (c) and (d) are adapted from [33].

Solar absorbers are expected to operate at a temperature similar to thermal emitters, especially in an STPV system. Therefore, they face the same challenge of thermal stability as thermal emitters. The approaches to enhance reliability of nanophotonic

structures discussed in the preceding section can be borrowed and applied to selective solar absorbers.

1.1.3 Photovoltaic Energy Conversion

The last of the three main components of a TPV system is the PV diode. It absorbs the thermal radiation from the emitter and then converts it into electricity. When photons above the bandgap is incident on the PV diode, a portion of them are converted into electron-hole pairs. Such conversion ratio is quantified as the external quantum efficiency ($EQE(\lambda)$), a wavelength dependent quantity that's typically high above the bandgap and low otherwise. The generated short-circuit current I_{SC} can be calculated as:

$$I_{SC} = qA_e F_{e-pv} \int d\lambda \left(\frac{\lambda}{hc}\right) \epsilon(\lambda) I_{BB}(\lambda, T) EQE(\lambda), \tag{1.9}$$

where A_e is the surface area of the emitter; F_{e-pv} is the view factor from the emitter to the PV diode (assume no filter implemented); $\epsilon(\lambda)$ is the emittance of the emitter, and the emitter operates at temperature T.

Assuming there's minimal series resistance and shunt resistance, the I-V curve of a PV diode under illumination follows the ideal diode equation:

$$I = I_0 \left(e^{\frac{qV}{nkT_{pv}}} - 1\right) - I_{SC}, \tag{1.10}$$

where I_0 is the dark current that is determined by the property and temperature of the PV diode; n is the ideality factor; T_{pv} is the temperature of the PV diode. The open-circuit voltage V_{OC} can then be derived as:

$$V_{OC} = \frac{nkT_{pv}}{q} \ln\left(\frac{I_{SC}}{I_0} + 1\right), \tag{1.11}$$

The converted power calculated by Eq. 1.4 corresponds to the maximum power point

on the I-V curve. To find this point, or equivalently the fill factor FF, an empirical equation is commonly used:

$$FF = \frac{v_{OC} - \ln(v_{OC} + 0.72)}{v_{OC} + 1}, \tag{1.12}$$

where v_{OC} is the normalized open-circuit voltage defined as $v_{OC} = (q/nkT_{pv})\, V_{OC}$. The I_{sc}, V_{OC} and FF calculated by Eq. 1.9, 1.11 and 1.12 can be fed into Eq. 1.4 to calculate the converted electric power.

Based on the physics of photovoltaic energy conversion, it is clear that TPV performance is strongly dependent on the properties of PV diodes. In fact, various types of PV diodes have been used in TPV research to find the best candidate. There are a few that garnered most of the interest.

Crystalline Si PV diode, as one of the most commonly used PV materials, has its strength in relatively high quality (high EQE above bandgap and low I_0) and inexpensive fabrication. However, the greatest challenge of using c-Si PV diode is the mismatch between its $EQE(\lambda)$ and the thermal emission spectrum of the emitter. It has been shown that pairing a Yb_2O_3 thermal emitter with a Si PV diode gives a TPV conversion efficiency of only 2.4% [58]. Using 2D PhC thermal emitter made of W in conjunction with highly effective photon recycling, the TPV conversion efficiency has been estimated to be 26.2% when emitter is at 1573 K [6].

A better alternative is germanium (Ge). Its lower bandgap ($E_g = 0.66$ eV) helps reducing sub-bandgap loss significantly. One challenge with Ge is its relatively high density of states in the conduction band, leading to high intrinsic carrier concentration and thus high dark current I_0 [59]. It has been demonstrated that a lightly doped Ge PV with both front and rear passivated is suitable for TPV applications when paired with Er_2O_3 thermal emitter [60].

GaSb PV diodes, with a low bandgap of $E_g = 0.72$ eV, are far more commonly used in TPV systems compared with the aforementioned two. It has been calculated that a TPV conversion efficiency of 30% is possible for a blackbody thermal emitter

with a temperature higher than 1300 K, if an ideal filter that matches the bandgap is used [61], which is consistent with the 27% efficiency reported in Ref. [62] where a W emitter has been used. Fraas also extensively studies GaSb PV diodes for TPV applications. He pointed out that the cost of production can be substantially lowered if the production volumes surpasses 1 MW [63].

$In_xGa_{1-x}As$ is a ternary composite that allows bandgap tuning via varying indium composition. The range of bandgap is 0.4 - 1.4 eV. While fabrication cost for InGaAs is high, its performance is outstanding. It has been shown that a lattice-matched InGaAs (E_g = 0.74 eV) has a broadband high EQE (above 90%), which is highly favorable for TPV applications [64]. Furthermore, the wide range of allowed bandgap gives rise to tandem PV that can better utilize different portions of the thermal radiation spectrum from the emitter. It has been demonstrated that a tandem PV consisting of epitaxially grown 0.74 eV lattice-matched $Ga_{0.47}In_{0.53}As$ and 0.63 eV lattice-mismatched $Ga_{0.36}In_{0.64}As$ gives promising performance as a TPV diode [65].

1.1.4 System Integration

Critical components of a TPV or STPV system have been reviewed in the preceding sections. High-performance TPVs/STPVs rely not only on high performance components, but also on optimal system integration. In this section, we review some of the most critical factors of TPV system integration.

For STPV specifically, it is important to find the optimal area ratio between thermal emitter and solar absorber ($\beta = A_{emitter}/A_{absorber}$). For a given solar concentration, there exists an optimal area ratio β that gives highest conversion efficiency η_{stpv}. This can be understood in the following way: as β increases, the temperature of absorber/emitter assembly decreases. As a result, TPV conversion efficiency η_{tpv} drops while thermal transfer efficiency η_t increases. Therefore, there is an optimal β corresponding to an optimal operating temperature. For example, when the solar concentration is 1000 suns, the optimal β is 16 [11].

For a general TPV system, thermal management is another challenge. First, any heat transfer between thermal emitter and PV diode, other than radiative heat transfer, should be suppressed. Therefore, there should be a vacuum gap (¡ 10^3 Torr [66]) that separates the thermal emitter and the PV diode. Such vacuum environment can also alleviate reliability issues of thermal emitters when operating at high temperature. Second, a high view factor from the emitter to the PV diode is required. To reach a view factor > 0.9, a separation of $< 5\%$ of the edge length should be maintained (e.g., when both the emitter and the PV diode are 10 mm$\times$10 mm, a separation < 500 μm is needed) [67]. This requirement imposes a challenge of aligning thermal emitters and PV diodes. Though precision translation stage is capable of maintaining a 300 μm gap [66], a much less structurally complicated solution is needed in order to make TPV ready for real applications like portable power generator. Third, the PV diode under such high heat load, with at least one face encapsulated in vacuum, imposes a great challenge for cooling. In order to keep the PV diode operates close to room temperature, active cooling methods like running coolant or forced air cooling are used in existing literature. However, for a power generating system, it is preferred to have only passive cooling. Furthermore, one of the most attractive features of TPV is its noiseless operation. The cooling strategy should not cause extra noise if possible. In this context, new passive cooling methods other than conduction or convection warrant research effort. In the next few sections, a unique, passive cooling method known as radiative cooling will be reviewed in detail.

1.2 Radiative Cooling

Radiative cooling is a strategy to dissipate excess heat into remote heat sinks (such as the clear sky) via thermal radiation [68]. Its crucial value is that it can lower the operating temperature of a broad range of solid-state devices without requiring any input energy. It functions on the ground by enhancing radiation at wavelengths that are highly transmitted [69]; for the sky, this transparency window extends from

8 to 13 μm [70]. The earliest adoption of radiative cooling has been traced back to the courtyard architectures of ancient Iran [71]. In the modern era, the first scientific studies found that certain materials have potential for limited selectivity, notably polymeric materials [72,73], titanium dioxide [74–76], silicon nitrides [77], and silicon monoxide (SiO) [78]. While cooling to 40 °C below ambient with SiO is theoretically possible [78], the temperature difference is much smaller in experiments [69]. Although the natural materials listed above can enhance radiative cooling, achieving the best possible radiative cooling requires a combination of high and flat emittance throughout the sky transparency window. No simple bulk material has been reported to provide this ideal emittance spectrum, and thus, theoretically maximal radiative cooling power.

Fortunately, with the emergence of new classes of selective infrared (IR) emitters [11,20,79], based on photonic design principles [80], interest in radiative cooling has increased substantially in the last several years. Recent calculations first indicated, for instance, that 2D nanophotonic structures can provide a cooling power in excess of 100 W/m^2 at reasonable temperatures [81]. A 1D stack of hafnia and silica, consisting of seven bilayers, was shown to be sufficient to achieve cooling below ambient temperatures in experiment [82]. Before this recent resurgence of interest, research efforts focused on looking for the best cooling material for below-ambient cooling at night. Most materials investigated previously were bulk materials or composite materials. Some were found to be satisfactory for nocturnal applications. However, the capability of daytime radiative cooling under direct sunlight, especially below ambient, was never fulfilled until very recently. The development of nanophotonics is certainly a major driving force behind the recent resurgence of radiative cooling research. It is found that minimal absorption of direct sunlight and high emittance within the atmospheric window can both be satisfied by nanophotonic designs. As will be discussed later in Section 1.2.1, the capability of daytime radiative cooling, compared with nighttime cooling, gives rise to more applications and research opportunities in different fields. In related work, it was shown that this approach can

be applied to solar cells to theoretically achieve meaningful temperature reductions. Theoretically, the temperature for bare silicon cells can be up to 17.6 °C in unconcentrated sunlight [83], with an actual 13 °C cooling effect observed in experiment [84]. Similarly, despite their lower self-heating, GaAs nanowire-based photovoltaics (PV) could potentially experience a radiative cooling-induced temperature drop of 7 °C [85], which could improve their performance by 2.6% absolute efficiency in the near-earth orbit [86]. For encapsulated commercial solar panels, the cover glass (typically soda-lime glass) is already a decent broad-band radiative cooler. Hence, a temperature decrease of only 1 - 2 K is achievable by radiatively cooling commercial solar panels, which can still extend the lifetime significantly by suppressing thermally activated degradation [87].

The resulting drop in efficiency associated with excess heating can be tremendous, potentially, over 50% of the relative performance [88]; thus, it is critical to develop new strategies for cooling that are nearly or fully passive, as opposed to active, to preserve overall system efficiencies and to substantially decrease operating temperatures, improving performance for a wide range of devices. In the best case, this additional cooling power could result in below-ambient operation, potentially enabling significant improvement in performance and reliability.

Given these significant benefits, it seems appropriate to consider what other systems could potentially benefit the most from this radiative cooling approach. The most appealing applications would presumably combine considerable self-heating and significant needs for energy efficiency. Within this group, solid-state electronics stand out as particularly relevant, since they can experience substantial radiative heating outdoors during the daytime, along with electric power injection and subsequent thermal dissipation. Concentrating photovoltaics (CPV) and thermophotovoltaics (TPV) are likely to see even greater benefits from these approaches than standard PV, because of their greater heat fluxes [23].

1.2.1 Fundamental Physics of Radiative Cooling

The temperature of the cosmic microwave background radiation is around 3 K [89], while the ground-level temperature on earth is close to 300 K. This enormous temperature difference is kept by the atmosphere, where most thermal radiation from the ground is blocked. However, there exists several transmission bands, through which certain portion of radiated energy may escape. Such atmospheric transmission windows are determined by the atmospheric absorption spectrum [69, 90–96], which features a strong water vapor absorption band centered around 6 μm and beyond 20 μm, as well as a carbon dioxide absorption band that peaks around 15 μm. These absorption bands leave behind an atmospheric transmission window from 8 to 13 μm, as depicted in Fig. 1.10. Furthermore, the atmospheric emittance is not only wavelength dependent, but also zenith angle dependent, as expressed by the following equation [69]:

$$\epsilon_a(\theta, \lambda) = 1 - [1 - \epsilon_a(0, \lambda)]^{1/\cos\theta}, \tag{1.13}$$

where $\epsilon_a(\theta, \lambda)$ denotes the atmospheric emittance at any arbitrary zenith angle θ. The angular dependence is shown in Fig. 1.10 as well.

Developing radiative coolers for various applications requires rigorous engineering and design. In this subsection, we review the physics of radiative cooling by the steady-state energy balance equation and summarize the design considerations for radiative coolers.

When a radiative cooler of surface area A is exposed to the sky, the cooling power P_{cool} is the net outgoing radiative energy flux, defined as:

$$P_{cool}(T) = P_{rad}(T) - P_{atm}(T_{atm}), \tag{1.14}$$

where $P_{rad}(T) = A \int d\Omega \cos\theta \int_0^\infty d\lambda I_{BB}(T, \lambda)\epsilon(\lambda, \theta)$ is the thermal emission of the ra-

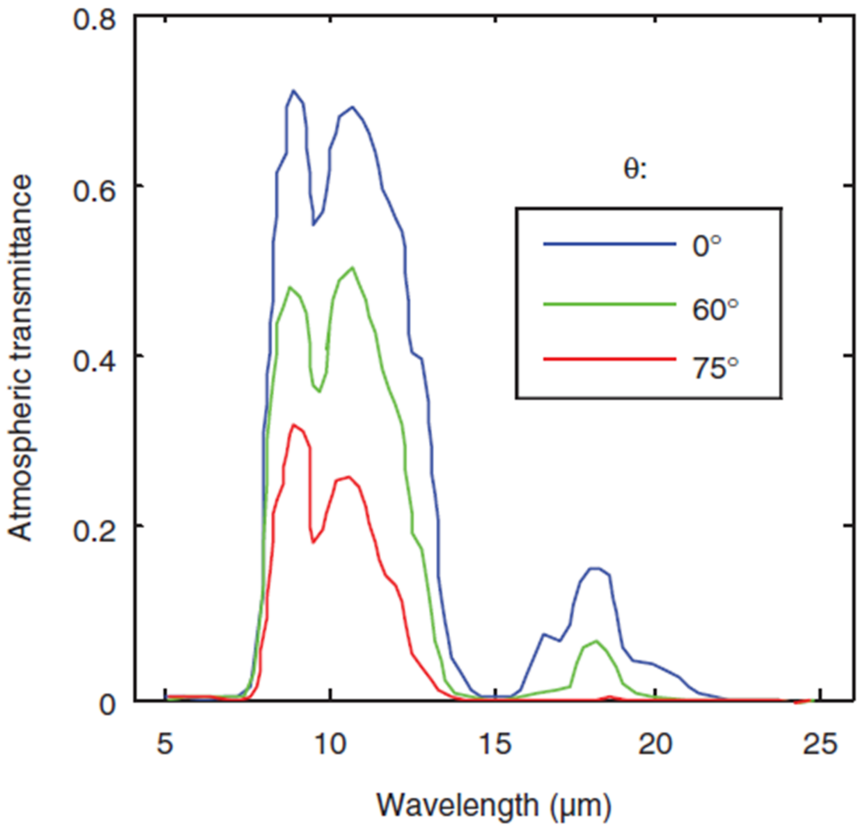

Fig. 1.10. The atmospheric transmittance spectrum at zenith angles of 0°, 60°, and 75°; it is highest in the 813 μm transparency window. Results are adapted from [69].

diative cooler with operating temperature of T, and $\int d\Omega \cos\theta$ is the integration of the solid angle over the hemisphere. The atmospheric radiation at a temperature T_{amb} is given by $P_{atm} = A \int d\Omega \cos\theta \int_0^\infty d\lambda I_{BB}(T_{amb}, \lambda)\epsilon(\lambda, \theta)\epsilon_{atm}(\lambda, \theta)$, where $\epsilon_{atm}(\lambda, \theta)$ denotes the spectral and angular atmospheric emittance that can be calculated by Eq. 1.13. The balance of radiative cooling power with other energy fluxes (e.g. incident solar power, convective, and conductive heat transfer) determines the temperature achievable.

When designing a practical, efficient radiative cooling system, one must also con-

sider other heat transfer pathways. Generally, the net power of the cooling system P_{net} is defined as:

$$P_{net} = P_{cool} - P_{abs,sun} - P_{non-radiative}, \tag{1.15}$$

where P_{cool} denotes the radiative cooling power, $P_{nonradiative}$ corresponds to non-radiative heat transfer (i.e. convection and conduction) and $P_{abs,sun}$ is the total absorbed solar power only relevant for daytime applications. Initially, nighttime radiative cooling appeared much more promising thanks to the absence of solar irradiance, and constituted the focus of the early work [97–101]. Enabled by recent advances in photonic design, daytime radiative cooling below ambient temperature has been demonstrated by Rephaeli et al. [81]. According to Eq. 1.15, solar absorption and non-radiative heat transfer, in cases where $T < T_{amb}$, act as parasitic cooling losses, thereby reducing the overall cooling effect. Remarkably, it has been experimentally demonstrated that significant temperature reduction more than 40 K below ambient can be reached by radiative cooling within 1 hr with considerably reduced parasitic heat transfer (e.g. no convection in the vacuum chamber and sun shade to block solar irradiance). [102]. The lowest temperature measured is far lower than the previous non-optimized experimental demonstration [82]. For systems with greater heat loads (e.g. CPV and TPV), it is also expected that the temperature will quickly reach steady state due to significant heating, for example, temperature varies instantaneously with solar irradiance in Ref. [103]; in such cases, radiative cooling can still serve as a complementary passive cooling method to reduce overall system temperature.

Radiative cooling can be categorized as either below-ambient or above-ambient, depending on specific applications. The target cooling temperature of a radiative cooler determines the desired spectral emittance profile; namely, a broadband cooler is needed for above-ambient cooling, while a selective cooler is needed for below-ambient cooling. As shown in Fig. 1.11 (green curve), the broadband cooler should

have emittance close to one throughout the IR spectrum, and negligible absorptance in the solar spectrum for daytime cooling. On the contrary, a spectrally selective cooler will have emittance close to unity only in the atmospheric window ($8-13$ μm) and minimal emittance elsewhere (yellow curve in Fig. 1.11). Next, we will interpret such design requirements into the temperature and spectrum dependence of $P_{cool}(T)$.

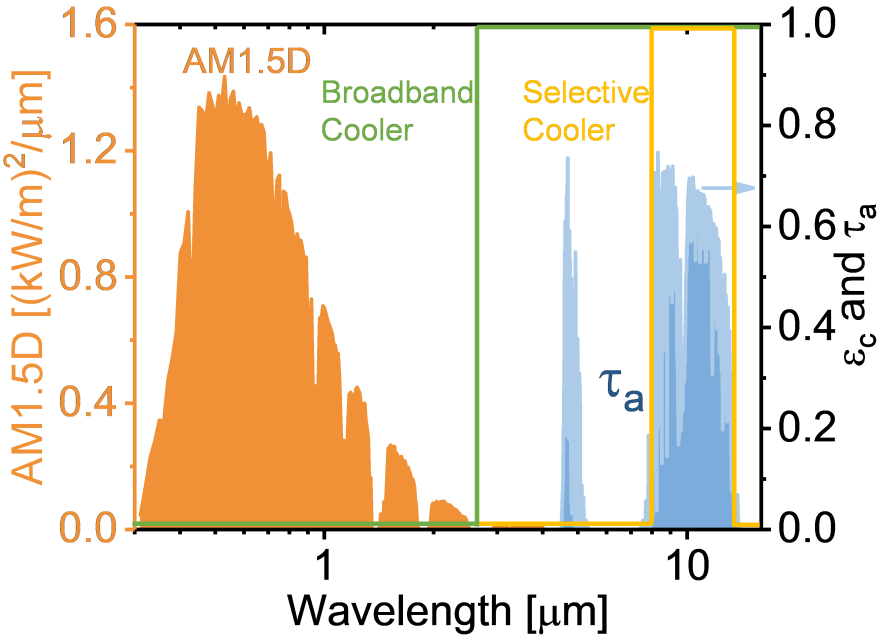

Fig. 1.11. Ideal emittance spectrum (ϵ_c) of radiative coolers for above-ambient cooling and below-ambient cooling. For above-ambient cooling, a spectral-selective cooler (yellow curve) that has high emittance only within the atmospheric window (blue shaded region) should be used. For below-ambient cooling, a broadband cooler (green curve) with high emittance across a broad range of IR wavelengths and minimal absorption of the solar spectrum should be used.

$P_{cool}(T)$ must be positive to ensure net cooling of a system. For above-ambient cooling (i.e. $T > T_{amb}$), the thermal radiation outside the atmospheric window from the cooler to the ambient (i.e. above-ambient cooling) becomes beneficial and adds up to higher total cooling power $P_{cool}(T)$; thus, a broadband design is preferable

to deliver more cooling gain. For below-ambient cooling (i.e. $T < T_{amb}$), parasitic thermal emission outside $8-13$ μm from atmosphere heats up the cooler, resulting in a negative cooling power for the broadband design. In contrast, a spectral selective cooler that can eliminate such undesired absorption of radiation from ambient and maximize $P_{cool}(T)$ is the best for below-ambient cooling. An interesting feature of radiative cooler is that at $T = T_{amb}$, the net thermal radiation outside the $8-13$ μm wavelengths from the coolers to the ambient becomes zero; essentially, both designs deliver the same cooling power. To summarize, cooler designs should be adopted for different applications. Note that the discussion above only considers the primary atmospheric window from 8 to 13 μm, and has neglected the secondary atmospheric window that exists between 16 and 22 μm. Our simulation has shown that, with the presence of the secondary window, full-spectrum radiation coolers can generate $10-20$ W/m^2 more cooling power than the selective radiative coolers only focusing on $8-13$ μm. The secondary window, however, contributes only about 10% of the total cooling power at near-ambient temperature due to much lower transmittance (see Fig. 1.10) and deviation from the wavelength range (i.e. around 10 μm) wherein IR blackbody radiation peaks. Since the impact of the secondary window on radiation cooling is fairly insignificant, it can be neglected in general. In the next section, we describe specific materials and structures that are suitable for either type of cooling.

1.2.2 Review of Radiative Cooler

To achieve effective radiative cooling, cooling structures should have emittance spectra $\epsilon(\theta, \lambda)$ that match the ideal specifications discussed in Section 1.2.1. Fortunately, emittance properties approaching these ideals can be found in bulk materials suitable for massive production. They have been extensively studied in pioneering works of the 1970s and 1980s [68, 69, 72, 73, 77, 78, 97, 104–110]. Similar to bulk materials, gaseous materials such as ethylene and ammonia have also been proposed to be radiative coolers [109, 111, 112]. Furthermore, several works also focused on using

pigmented foils that are highly reflective in the solar spectrum and transparent in the atmospheric window, such that an underlying material can simultaneously cool itself via thermal emission without absorbing solar irradiance [74–76]. As the fabrication technique of nanomaterials advances, radiative coolers enabled by nanostructures and nanoparticles are proved to be good alternatives to bulk coolers [113, 114]. In recent years, nanophotonic structures have become powerful in tailoring the thermal emission properties of bulk materials [20, 21] and have a significant impact on different applications, including radiative cooling. It is demonstrated by simulation that properly designed photonic crystals (PhCs) can provide emittance spectra close to the ideal cases for radiative cooling (both above-ambient and below-ambient) under direct solar irradiance [81, 83, 115, 116]. Later, experiments successfully demonstrated the radiative cooling via PhC coolers [82, 84]. In addition to the spectral selectivity, the angular dependence of emittance is another important factor for radiative coolers, as implied in Eq. 1.14. Complete characterization of a radiative cooler should include its emittance spectra at multiple zenith angles. For cooling systems that are not angularly restricted, the emittance variation over zenith angles from 0° to 90° is preferred to be as small as possible [69]. It has recently been demonstrated that the weak angular dependence of emittance can be achieved by nanophotonic structures such as polymer stacks [117] and 2D PhC structures [84].

Bulk and Gaseous Material Radiative Coolers

In the early stage, plastic has been investigated as a prospective candidate for radiative coolers. Polyvinyl chloride (PVC) [72], polyvinyl fluoride (PVF) [68, 73, 97, 106, 107], and polymethylpentene (TPX) [105] were shown to have high emittance in the atmospheric window. Most plastic coolers reported in the literature were aluminized at the back to block transmission without adding significant absorption outside the atmospheric window. Although the TPX and PVF emittance spectra match the atmospheric window, as shown in Fig. 1.12(a) [69, 105], TPX is slightly

better, due to its higher emittance near 8 μm.

Alternative bulk materials, such as oxide and nitride, have been investigated

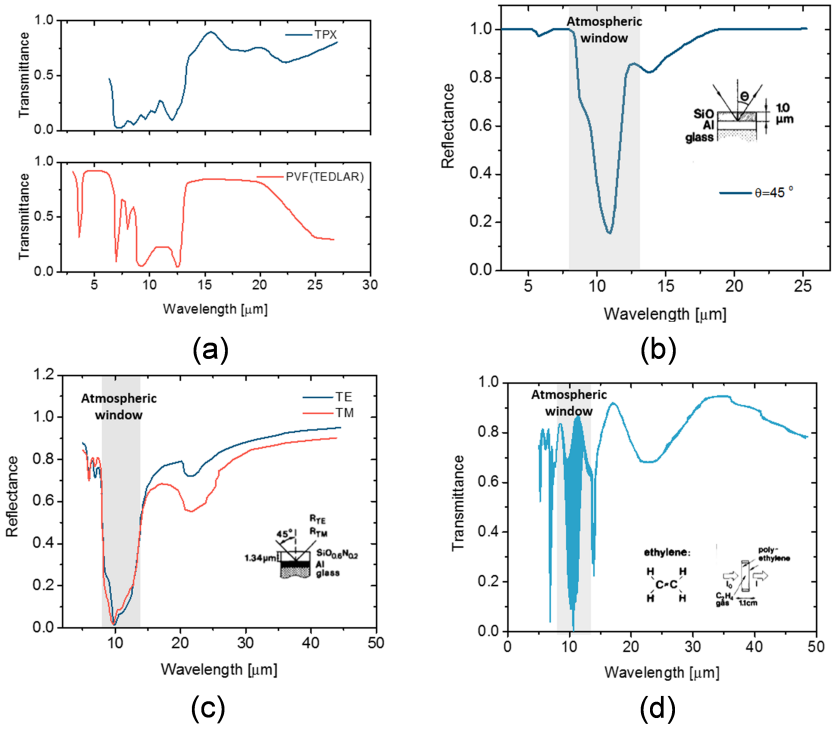

Fig. 1.12. (a) Transmittance spectrum of aluminized polyvinyl fluoride (TEDLAR) cooler (red) and polymethylpentene (TPX) cooler (blue); adapted from [69, 105]. Strong emittance can be observed within the atmospheric window. (b) the measured reflectance spectrum of 10 μm SiO film on aluminum (Al). The spectrum is adapted from [69]. (c) The measured reflectance for TM (red) and TE (blue) polarizations incident on a 1.34 μm $SiO_{0.6}N_{0.2}$ film on Al. Compared to SiO, a broader peak is found within the atmospheric window. The spectrum is adapted from [109]. (d) The measured transmittance spectrum of ethylene gas in a 1.1-cm-thick gas slab. The spectrum is adapted from [111].

extensively in the pioneering works of Granqvist et al. It was found that SiO, with its strong lattice absorption near 10 μm, can serve as a selective radiative cooler. The optimal thickness of 1 μm was found to be most effective in reducing reflection [69,78]. Like the previous structure made from plastic coolers, an Al back reflecting layer was

coated by evaporation [69, 78]. The structure and the reflectance of the SiO cooler are shown in Fig. 1.12(b) [69]. However, the emittance of SiO within the atmospheric window is not strong enough to yield a significant improvement in the cooling effect compared with a blackbody cooler during a nocturnal test. The SiO cooler cooled to 13.8 °C below ambient, while the blackbody cooler cooled to 13.4 °C below ambient [69]. Therefore, a stronger cooler consists of silicon nitride (Si_3N_4), and the Al back reflector was fabricated in the following work [77]. (Si_3N_4) has been explored again in a more recent work, showing a capability of sub-freezing temperature cooling (−22.2 °C) [102]. The optical properties of silicon oxynitride (SiO_xN_y) have also been studied [108, 110], with its application as a selective cooler examined in [109]. As shown in Fig. 1.12(c) [109], a 1.34-μm-thick ($SiO_{0.6}N_{0.2}$ ($x = 0.6$ and $y = 0.2$) on the Al back reflector exhibits a strong emittance peak that matches the atmospheric window. The peak is related to the SiO and SiN bonds [118, 119] and the shoulder near 8.5 μm is related to the SiH bond [118]. The net result was an equilibrium temperature of (16 °C) below ambient during nighttime, (2 °C) lower than what was achieved by a blackbody cooler [109]. For above-ambient cooling, it was found that fused silica is a suitable cooler with its high emittance across a broad wavelength range except for a dip within the atmospheric window. It is demonstrated to be able to cool an underlying Si wafer by (12 °C) [84]. Soda-lime glass or low-iron glass, commercially used as cover glass for PV, was found to be slightly better than fused silica for above-ambient cooling [120]. More recently, a structural material prepared by delignificated and densificated wood is shown to exhibit emittance properties that are suitable for daytime above-ambient cooling [121].

Radiative coolers in gaseous state have also been considered for radiative cooling applications. It is shown that for ammonia gas (NH_3), the IR absorption corresponding to the N atom moving perpendicularly to the H_3 plane is broadened by the rotational absorption so that it covers the atmospheric window [112]. Theoretical modeling showed that a slab of (NH_3) gas can potentially cool down to (20 °C) below ambient during nighttime [112]. Similarly, with out-of-plane bending vibrations,

ethylene (C_2H_4) also exhibits strong emittance in the atmospheric window, as shown in Fig. 1.12(d) [111]. When encapsulated in an IR transparent container, C_2H_4 is a good candidate for radiative coolers that reached (10 °C) below-ambient cooling during daytime without direct sunlight [111]. Eriksson et al. showed that a mixture of C_2H_4 and C_2H_4O has higher cooling power, compared with either C_2H_4 or C_2H_4O [109].

Composite Radiative Coolers

As an alternative to bulk and gaseous material radiative coolers, composite material coolers consisting of two or more different materials were investigated, and were shown by several groups to have emittance properties suitable for radiative cooling. Commercially available white paints containing 35% TiO_2 provide a maximum (15 °C) drop in temperature with indirect sunlight, clear sky, and low absolute humidity; however, concerns regarding the true spectral selectivity of these TiO_2 paints were raised by Granqvist and Hjortsberg in their letter to the editor [122]. Additional experiments that applied white pigmented paints consisting of $TiO_2/BaSO_2$ or TiO_2/ZnS in alkyd resin binder on Al panels showed a $9-12$ °C temperature drop under nocturnal conditions [75]. Furthermore, a recent study showed that a polymer paint may allow for 6 °C sub-ambient cooling even during daytime [123].

The development of nanomaterials offered more choices of cooler design. Suryawanshi and Lin fabricated and tested three types of above-ambient radiative coolers consisting of carbon-based nanomaterials [nanodiamond powder (NDP), multi-wall carbon nanotubes (CNTs), or carbon black (CB)] dispersed in acrylate (AC) emulsion with the Al back panel [113]. It was found that the composite cooler with a CNT gives the best performance among the three, as shown in Fig. 1.13(a). Furthermore, 1 wt% of CNT in AC can lower the temperature by 17 °C from 87 °C [113]. Similarly, nanoparticles that have absorption bands that match the atmospheric window were added to polymeric binders to form radiative coolers for below-ambient cooling. It

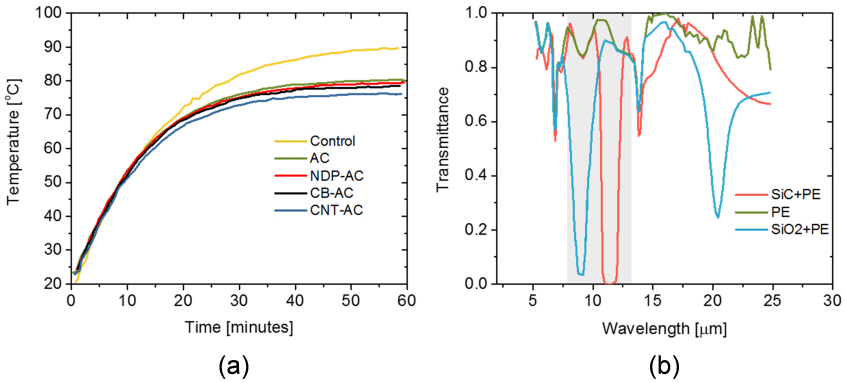

Fig. 1.13. (a) Operating temperature vs. time for carbon-based nanomaterial-composite coolers. The cooler with multiwall carbon nanotubes (CNT-AC) gives the best performance. Adapted from [113]. Copyright (2009) American Chemical Society. (b) The transmittance spectrum of SiO_2 nanoparticles in polyethylene binder (blue) and SiC nanoparticles in polyethylene binder (red). The transmittance spectrum of the polyethylene film itself [114] is shown in green. The two nanoparticle emission peaks are complementary to each other, and both fit within the atmospheric transparency window.

was found that the two IR absorption bands of SiO_2 and SiC nanoparticles, as shown in Fig. 1.13(b), are complementary to each other. Therefore, when the two nanoparticles are mixed together in the polyethylene film, the emittance spectrum matches well with the atmospheric window [114]. The estimated result from the model proposed in [114] showed that a 25 °C temperature drop below ambient can be achieved when there are limited non-radiative heat transfer and no sunlight. Other than polyethylene, PVF and polyvinylidene fluoride are also good polymeric binders for SiO_2 and SiC nanoparticle composite radiative coolers [124].

Nanophotonic Radiative Coolers

Nanophotonics opens up new possibilities to tailor the emittance spectrum via properly designing periodic nano/micro-structures, in analogy with prior efforts in

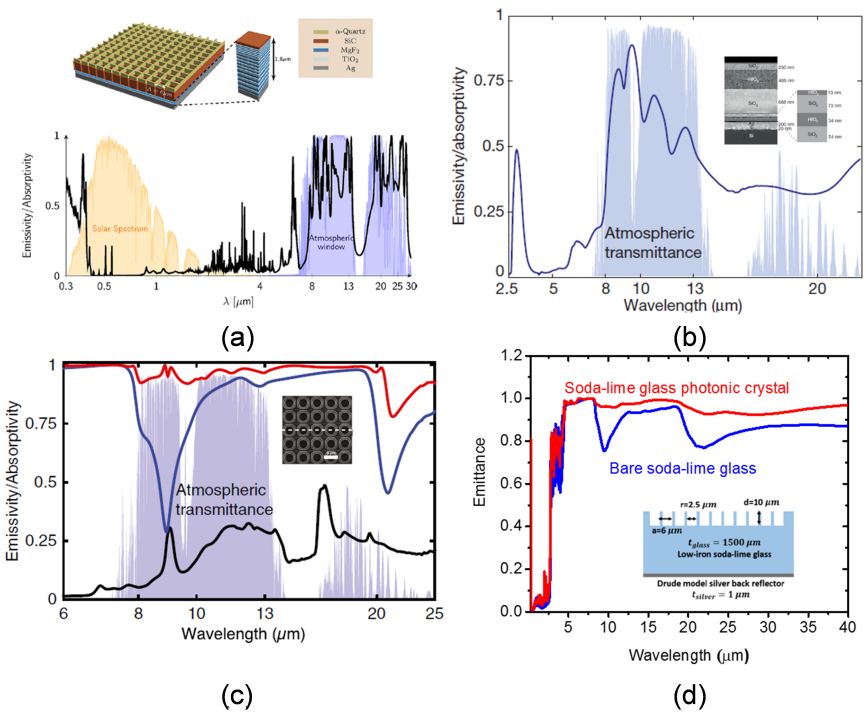

Fig. 1.14. (a) The numerically optimized photonic crystal cooler for a below-ambient cooler under direct solar exposure. Reproduced from [81]. Copyright (2013) American Chemical Society. (b) The measured emittance spectrum of the fabricated 1D photonic crystal cooler with feasible structures and excellent emittance within the atmospheric window. Adapted from Macmillan Publishers Ltd (Nature) [82], copyright (2014). (c) The measured emittance spectrum of a bare silicon wafer (black), a bare silica slab (blue) and a 2D photonic crystal of silica (red). It can be seen that the emission of silica in the atmospheric transparency window can be enhanced by the 2D square lattice structure. The figure is adapted from [84]. (d) Simulated emittance spectrum of bare low-iron soda-lime glass (blue) and 2D photonic crystal-enhanced bare low-iron soda-lime glass (red). A similar effect of enhanced emission within the atmospheric window is observed. The broad emission spectrum and low solar absorption is ideal for above-ambient daytime cooling. The figure is adapted from [116].

photovoltaics [125] and TPV [6, 23]. Similarly, for radiative cooling, the large degree of freedom in engineering nanophotonic structures potentially allows for better cooling performance than bulk material or composite coolers. It is proposed that a bar

array consisting of α-quartz gives strong selective thermal emission within the atmospheric window while preserving the solar absorption of the underlying structure (Si nanowire array on Al) [115]. The simulation showed that the temperature drop during daytime can be as large as 31.4 °C with a nonradiative heat exchange coefficient equal to 6 W/(Km^2) [115]. Stronger selectivity in thermal emittance can be achieved by more complex PhC structures. Rephaeli et al. proposed a structure consisting of two layers of quartz and SiC 2D PhC on top of a 1D chirped dielectric stack and silver (Ag) substrate [81]. As shown in Fig. 1.14(a), the structure proposed has a strong emittance spectrum that matches well with the atmospheric window due to the phonon-polariton resonances of quartz and SiC. Meanwhile, the introduction of a chirped dielectric reflector and the intrinsically low solar absorption of both quartz and SiC strongly suppressed solar absorption so that below-ambient cooling can be achieved during daytime [81]. The simulation showed that with the optimized PhC structure, a temperature of 7 °C below ambient can be reached with a non-radiative heat exchange coefficient of 12 W/Km^2) [81]. In experimental demonstrations, it was shown that a much simpler nanophotonic cooler structure also cools to 4.9 °C below ambient under direct sunlight [82]. Fig. 1.14(b) shows the emittance spectrum of the fabricated radiative cooler. The SEM cross-section of the cooler which consists of seven alternating layers of SiO_2 and HfO_2 on top of Ag is shown in the inset [82]. The significance of the result is that a properly designed one-dimensional photonic film that is feasible for large-scale fabrication could achieve below-ambient cooling in daytime. However, a low-density polyethylene film, serving as a convection barrier, is used in the experiment. The non-radiative heat transfer was therefore strongly suppressed, giving more significant below-ambient cooling effect. Fortunately, such below-ambient cooling in daytime can be achieved even without convection barriers [117]. Using multilayer polyester stacks, Gentle and Smith demonstrated 2 °C below-ambient cooling under mid-summer sunlight without using convective barriers [117].

For above-ambient cooling during daytime, nanophotonic coolers also showed

promising performance. It was proposed by Zhu et al. [83] that a 2D square lattice of SiO_2 pyramids can reduce the temperature of the underlying Si solar cell by 17.6 °C. Later, their experiments demonstrated that a 2D PhC consisting of a square lattice of air holes on SiO_2 cools the underlying Si wafer by 13 °C [84]. Fig. 1.14(c) shows the emittance spectrum of the SiO_2 PhC and its top-view SEM cross-section in the inset. Apparently, the PhC structure enhances the thermal emittance of bare SiO_2 within the atmospheric window, yielding an equilibrium temperature that is 1 °C lower than the case with bare SiO_2 [84]. A similar 2D PhC structure can enhance the thermal emittance of low-iron soda-lime glass as well. It is shown in Fig. 1.14(d) that a square lattice of air holes on low-iron soda-lime glass (structure cross-section in the inset) provides an almost uniform emittance that is close to unity in mid-IR and is highly reflective in the solar spectrum, which is close to the ideal case for above-ambient radiative cooling during daytime [116]. Simulations showed that such radiative cooler design cools the photovoltaic diode of a specific energy conversion device with high heat load, known as TPV, by 91 °C from 161 °C. The amount of cooling can significantly increase the efficiency of the TPV system and improve the reliability thereof.

Summary and Analysis of Radiative Cooling Materials

Various radiative coolers can be quantitatively compared by the cooling parameters defined in a way similar to [69]. From the discussion in Section 1.2.1, radiative coolers for below-ambient or above-ambient cooling have different ideal emittance spectra. Therefore, a pair of cooling parameters should be defined to capture the different requirements. Following the work by Granqvist et al. [69], the spectrally averaged hemispherical emittance inside the atmospheric window ϵ_{avein} is defined as:

$$\epsilon_{ave-in} = \frac{\int_{8\mu m}^{13\mu m} d\lambda I_{BB}(T_{atm}, \lambda)\epsilon(\lambda)}{\int_{8\mu m}^{13\mu m} d\lambda I_{BB}(T_{atm}, \lambda)}, \tag{1.16}$$

where $\epsilon(\lambda) = \int_0^{\pi/2} d(\sin^2\theta)\epsilon(\lambda,\theta)$ and $I_{BB}(\lambda,T)$ is Plancks blackbody radiation function. The spectrally averaged hemispherical emittance outside the atmospheric window ϵ_{aveout} is defined as:

$$\epsilon_{ave-in} = \frac{\int_0^{\infty} d\lambda I_{BB}(T_{atm},\lambda)\epsilon(\lambda) - \int_{8\mu m}^{13\mu m} d\lambda I_{BB}(T_{atm},\lambda)\epsilon(\lambda)}{\int_0^{\infty} d\lambda I_{BB}(T_{atm},\lambda) - \int_{8\mu m}^{13\mu m} d\lambda I_{BB}(T_{atm},\lambda)}. \tag{1.17}$$

It should be noted that this term is different from the spectrally averaged hemi-

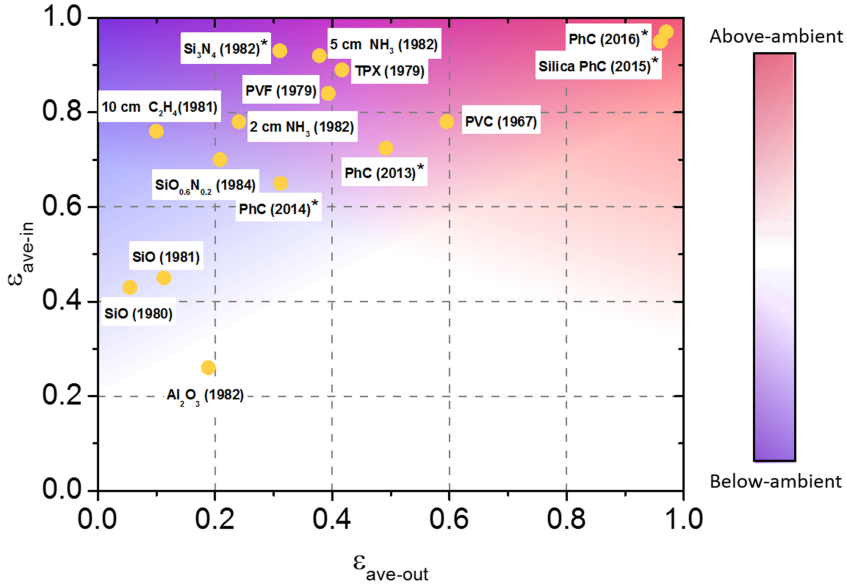

Fig. 1.15. Cooling parameters of selective radiative coolers. The top-left corner (blue shaded region) implies the best below-ambient cooling performance. The top-right corner (red shaded region) implies the best above-ambient cooling performance. Data points with * were calculated by the author, using detailed spectra previously presented in the references. Reference list: PVC (1967) [72], TPX (1979) [69], PVF (1979) [69], SiO (1980) [78], SiO (1981) [69], 10 cm C_2H_4 (1981) [111], Al_2O_3 (1982) [126], Si_3N_4 (1982)* [77], 2 cm NH_3 (1982) [112], 5 cm NH_3 (1982) [112], $SiO_{0.6}N_{0.2}$ (1984) [109], PhC (2013)* [81], PhC (2014)* [82], Silica PhC (2015)* [84], PhC (2016)* [116].

spherical emittance over the entire spectrum ϵ_{ave} defined by Granqvist et al. But it can be derived from ϵ_{ave} by substituting the first term in the numerator of Eq. 1.17) with $\epsilon_{ave} \int_0^\infty d\lambda I_{BB}(T_{atm}, \lambda)$. One important reason of picking these two parameters, as pointed out by Granqvist et al. [69], is that they do not depend strongly on the operating temperature of the cooler and can be easily used to estimate the cooling power at certain temperatures. For some of the radiative coolers discussed above, their cooling parameters are mapped in Fig. 1.15. For the coolers labeled with *, the cooling parameters are calculated based on published spectra and are limited by the spectral range presented. The top-left corner of the plot (blue shaded region) corresponds to the ideal emittance profile of a cooler for below-ambient cooling, while the top-right corner (red shaded region) corresponds to the ideal emittance profile of an above-ambient cooler. It is apparent that most demonstrated and proposed coolers lie in the top-left corner, and are therefore more suitable for below-ambient cooling. However, two designs (silica PhC (2015) [84] and PhC (2016) [116]) lie in the top-right corner, and are both strong candidates for above-ambient cooling. The map shows that bulk material coolers such as $SiO_{0.6}N_{0.2}$ and Si_3N_4 and gaseous coolers such as C_2H_4 and NH_3 already have good emittance spectra that are suitable for below-ambient cooling. Besides, although the absolute cooling of PhC designs is not always as good as bulk material coolers developed much earlier, their solar absorption can be suppressed much more significantly. This is an unprecedented advantage that enables below-ambient cooling even under direct sunlight. Remarkably, the map shown in Fig. 1.15 clearly differentiates the performance of different coolers for both above-ambient and below-ambient cooling. It also allows a quantitative comparison between different cooler designs, as well as estimating their cooling power. In the next section, we consider how various materials and designs can be applied to specific applications.

1.2.3 Radiative Cooling on Outdoor Optoelectronic Devices

In the preceding section, various radiative coolers for either above-ambient cooling or below-ambient cooling are reviewed comprehensively. Here, we review the application of radiative cooling on outdoor optoelectronic devices. For many optoelectronic devices, such as solar cells, photo detectors or TPVs, heating by the incident power can significantly impair the performance and reliability. Therefore, cooling becomes a critical part of a high-performance optoelectronic system. As radiative cooling emerges as a unique, passive cooling strategy, many researches have been focusing on applying radiative cooling to enhance optoelectronic device performance and reliability, especially for those operate in outdoor environment. In this section, benefits of cooling such as PV performance improvement and reliability enhancement will be discussed first. Theoretical and experimental studies of enabling radiative cooling on flat-plate photovoltaics (one-sun PV) will then be discussed. For systems with higher heat load, such as concentrating photovoltaics (CPV) and thermophotovoltaics (TPV), heating on the PV diode is much more severe. Research efforts on applying radiative cooling to CPV and TPV systems will be discussed as well.

PV Cooling

Based on the mechanism of photovoltaic effect, not all the incident radiation power can be converted into electricity. Thermalization loss and sub-bandgap absorption due to non-ideal back reflectors, highly doped layers and window layers [127, 128] can both increase the temperature of an operating PV device. For instantaneous performance degradation, higher temperature mainly affects the open circuit voltage (V_{OC}) of a PV diode. This is mainly because the intrinsic carrier concentration n_i increases exponentially with temperature:

$$n_i^2 = 4\left(\frac{2\pi kT}{h^2}\right)^3 (m_e^* m_h^*)^{3/2} \exp\left(-\frac{E_{g0}}{kT}\right), \tag{1.18}$$

where T is the temperature; m_e and m_h are the effective masses of electrons and holes, respectively; E_{g0} is the bandgap of the PV material (linearly extrapolated to 0 K); k and h are Boltzmann constant and Planck constant, respectively.

Higher intrinsic carrier concentration leads to higher dark current I_0, which increases quadratically with n_i:

$$I_0 = qA\frac{Dn_i^2}{LN_D}, \tag{1.19}$$

where A is the surface area of the PV diode; D is the diffusivity of minority carrier; L is the minority carrier diffusion length; N_D is the doping density; q is the elementary charge.

Following the diode equation (Eq. 1.11), V_{OC} drops as dark current I_0 increases. For Si PV, the rate of V_{OC} reduction is roughly 2.2 mV/°C. Considering that in real applications, flat plate PV can operate at a temperature about 20 - 40 °C higher than the ambient. Such reduction in generated power is non-trivial.

For long term applications, the increase in operation temperature hampers reliability. It is found that many degradation modes within PV, such as corrosion and potential-induced degradation [129, 130], are thermally activated. Therefore, cooling PV devices can also increase their lifetime. This benefit is particularly important, as the levelized cost of energy, a critical figure of merit when evaluating the viability of an energy conversion technology, can be significantly reduced when device lifetime is longer.

Radiative Cooling on One-sun PV

Implementing radiative cooling to one-sun PV attracts lots of attention, as it only requires adding an extra cooling layer on top of the existing PV system. Despite the simplicity, the theoretical cooling effect can be significant. Theoretical studies

show that an ideal above-ambient radiative cooler can lower the temperature of a bare Si solar cell by 18.3 °C [83]. Experimental demonstrations using SiO_2 2D PhC cooler achieved 13 °C cooling to a bare Si wafer [84]. Though the demonstration is not directly on PV devices, similar cooling effect can be expected for a bare Si solar cell. For encapsulated solar cells, which is more common in real applications, cover glass is already an existing radiative cooler. In this case, the aforementioned PhC radiative cooler can further lower the temperature by 1 - 2 °C [84, 120]. Therefore, a more comprehensive cooling strategy has been proposed for better cooling effect. It involves both radiative cooling and sub-bandgap photon screening [87, 131]. While radiative cooling alone reduces the temperature of one-sun PV by only 1 - 2 °C, its benefit on PV reliability is non-trivial. For failure modes with activation energy of 0.89 eV, PV lifetime can be extended by 20%. For this reason, radiative cooling on one-sun PV still has great long-term benefits.

Radiative Cooling on CPV and TPV

Different form one-sun PV, CPV and TPV systems have much higher heat load. There is more demand for excessive heat dissipation strategies that are reliable and less energy consuming. Radiative cooling is therefore a particularly appealing cooling method for such systems.

CPV operates under concentrated sunlight. The incident photon flux can be more than 100 times higher than one-sun PV, depending on the concentration factor. As a result, the temperature at the PV diode can be too high for optimal performance. For example, the temperature of a PV diode in a CPV system with 24 sun concentration can reach 140 °C even with conventional passive cooling [132]. Such high temperature greatly impairs conversion efficiency and device lifetime. To achieve better cooling effect, active cooling methods including forced air cooling or liquid cooling are implemented. However, those active cooling methods consume power and involve many moving parts, reducing its reliability for long-term operations. In this

context, radiative cooling has been proposed as a complementary cooling strategy. It has been shown through theoretical calculation that radiative cooling, in conjunction with passive air convection, may lower the operating temperature of a high concentration photovoltaic (HCPV) system to only 15 °C above ambient [133]. Furthermore, the radiative cooler can be much lighter compared with conventional copper coolers for same cooling power, which makes the dual-axis solar tracking of HCPVs more reliable and cost-effective [133].

Similar to CPV, TPV suffers from high heat load due to the high-temperature thermal emitter and the high view factor. The aforementioned active cooling methods have been implemented in most reported TPV demonstrations. In addition to power consumption and reliability issues, active cooling may also lower the value of TPV in the application of military power supply, where quietness is a key factor to be considered. Zhou et al. [116] proposed a setup for radiatively cooled outdoor TPV applications. Using an opto-electro-thermal coupled simulation framework, a temperature drop of 90 °C of TPV cells by radiative cooling has been predicted in [116]. With sufficient cooling concentration factor (area ratio between the radiative cooling emitter and the PV cell), below-ambient cooling of TPV during daytime can be realized by employing low-iron soda-lime glass as the radiative cooler, allowing TPV exceeding the optimal efficiency at room temperature. Details of this study will be discussed in Chapter 6.

1.3 Outline of The Thesis

High-performance TPV/STPV systems require design and optimization of selective thermal emitters and selective solar absorbers. Towards the deployment of TPV in real applications, experimentally demonstrating selective emitters and absorbers that have high scalability, versatility and good high-temperature performance is equally important. On the system level, thermal management can strongly affect conversion efficiencies. Cooling strategies that are passive and effective warrant care-

ful explorations. This thesis will first focus on improving selective thermal emitters and solar absorbers via both numerical simulations and experimental demonstrations (in Chapter 2 to 5). It will then discuss the potential effect of radiative cooling on the thermal management of TPVs (in Chapter 6 to 7). The following outlines the content and significance of each chapter.

- Chapter 2 addresses the challenge of reducing sub-bandgap emissions from a realistic thermal emitter. An integrated photonic crystal selective emitter is proposed to achieve ultra-high spectral selectivity, eliminating the conventional cold-side filter photon recycling.

- Chapter 3 introduces the design of an integrated photonic crystal selective solar absorber. Its ultra-high spectral selectivity allows near-ideal thermal conversion efficiency. It can be further integrated with the thermal emitter designed in Chapter 2 to form a monolithic emitter/absorber assembly for high-performance STPV.

- Chapter 4 introduces a high-temperature emittance measurement setup, including its design considerations and calibrations. The apparatus is a critical tool for high-temperature characterization of selective thermal emitters and solar absorbers.

- Chapter 5 addresses the challenge of making solar absorbers and emitters that are highly scalable, mechanically flexible and spectrally selective under high temperatures. A thin-film Si-based absorber/emitter is fabricated and characterized at high temperature using the setup introduced in Chapter 4. Its simplicity, exceptional mechanical flexibility and good high-temperature performance are experimentally demonstrated.

- Chapter 6 proposes a potential framework of using radiative cooling as a complementary passive cooling strategy in a TPV system. The effect of radiative cooling under different TPV operating conditions are studied.

- Chapter 7 experimentally demonstrates enhanced radiative cooling on a concentrating photovoltaic (CPV) system. Both instantaneous performance improvements and potential increase in PV lifetime are studied. The similarities between CPV systems and TPV systems allow extending radiative cooling to TPV applications in future works.

SELECTIVE THERMAL EMITTERS AND SOLAR ABSORBERS

Chapter 2 to Chapter 5 focus on design, fabrication and characterizations of spectrally selective thermal emitters and solar absorbers for high-performance TPV/STPV applications.

Specifically, Chapter 2 and Chapter 3 present designs and optimizations of selective thermal emitters and solar absorbers, respectively.

Chapter 4 presents the experimental system built for high-temperature emittance characterization of selective thermal emitters and solar absorbers. Chapter 5 presents the fabrication and characterizations of a thin-film Si spectrally-selective absorber/emitter.

2. INTEGRATED PHOTONIC CRYSTAL SELECTIVE EMITTER FOR THERMOPHOTOVOLTAICS[1]

Converting blackbody thermal radiation to electricity via thermophotovoltaics (TPV) is inherently inefficient. Photon recycling using cold-side filters offers potentially improved performance but requires extremely close spacing between the thermal emitter and the receiver, namely a high view factor. Here, we propose an alternative approach for thermal energy conversion, the use of an integrated photonic crystal selective emitter (IPSE), which combines two dimensional photonic crystal selective emitters and filters into a single device. Finite difference time domain and current transport simulations show that IPSEs can significantly suppress sub-bandgap photons. This increases heat-to-electricity conversion for photonic crystal based emitters from 35.2% up to 41.8% at 1573 K for a GaSb photovoltaic (PV) diode with matched bandgaps of 0.7 eV. The physical basis of this enhancement is a shift from a perturbative to a nonperturbative regime, which maximized photon recycling. Furthermore, combining IPSEs with nonconductive optical waveguides eliminates a key difficulty associated with TPV: the need for precise alignment between the hot selective emitter and cool PV diode. The physical effects of both the IPSE and waveguide can be quantified in terms of an extension of the concept of an effective view factor.

2.1 Introduction

Thermophotovoltaics (TPV) convert heat to electricity via thermal radiation. Photons with energies below the bandgap of the photovoltaic (PV) diode, resulting from the broad spectrum of the Planck blackbody distribution, are generally the

[1]Adapted from: Z. Zhou, O. Yehia, and P. Bermel, "Integrated photonic crystal selective emitter for thermophotovoltaics," *Journal of Nanophotonics*, vol. 10, no. 1, 2016.

dominant source of loss in TPV systems. Fortunately, these energy losses can be eliminated by selective emitters that have near-blackbody emission above the PV bandgap and low emission below the PV bandgap [4]. Several materials have been proposed for selective emission, including plasmonic metamaterials [27, 134, 135], refractory plasmonic structures [136], rare earth materials [13, 16, 17], and photonic crystals (PhCs) [20, 22–24, 36, 66, 79, 80, 137–144]. However, realistic selective emitters still have residual low energy emission near the bandgap that can considerably limit the conversion efficiency. Significant improvement can be achieved by the use of cold-side PhC filters, including plasma filters, quarter-wave stacks [145], and rugate filters [146]. These filters essentially reflect the low-energy photons back to the selective emitter, in a process known as photon recycling [147–152]. In order to achieve sufficient photon recycling, proximity between the emitter and filter is required [153]. In the typical cold-side filter configurations, where the filter is attached to the PV diode as an entire receiver, this requirement can be quantified by the view factor from the emitter to the receiver, which is the probability that emitted photons reach the receiver. Certain strategies, such as micro-gap or nanoscale-gap TPV, in fact require extremely high view factors to achieve evanescent coupling [154–156]. However, it is extremely difficult to achieve high view factors in experiments, since a constant gap d must be maintained between two surfaces when the distance is orders of magnitude smaller than the lateral width w of each surface. The angular tolerance $\theta_{tot} = \tan^{-1}(d/w)$ is impractically low. Although ultra-narrow (scanning electron microscope-like) tips can achieve such small gaps, the associated power produced is extremely small.

Despite the great potential for the improvement of TPV associated with these various approaches, certain common challenges remain in translating these ideas into experiment. One major difficulty is in achieving and maintaining sufficiently selective thermal emission. While simpler structures can be fabricated with high fidelity, their selectivity is often lacking, while more complex monolithic structures with higher potential selectivity are more vulnerable to fabrication error and degradation, which

becomes even more severe with finer features [38]. Composite structures consisting of simple emitters and cold-side PhC reflectors also have potential for highly selective effective emissivity, but these give rise to a second common problem: achieving precise alignment between a hot emitter and cold receiver. Unfortunately, configurations requiring the greatest precision are the same as those with the highest power generation potential. In order to overcome this challenge, it is important to fundamentally reexamine the geometric configuration of the three key objects: emitter, filter, and PV diode. While it is exceedingly difficult to bring the PV diode in contact with the emitter, it is certainly conceivable to bring the emitter and filter together. However, it is quite likely that a filter made exclusively of insulating materials would be a poor conductor of heat and thus would experience a significant thermal gradient. Therefore, a different treatment is needed, which correctly accounts for both the thermal gradient and potential for incoherent radiative exchange between the emitter and filter in proximity.

Thus, in this work, we propose an alternative approach for high-performance TPV systems capable of simultaneously addressing problems with long-lasting selectivity and alignment, known as an integrated photonic crystal selective emitter (IPSE), and develop a corresponding framework to analyze its performance. The IPSE combines the PhC selective emitter and the filter as an integrated whole, such that the view factor from the emitter to the filter approaches unity and is independent of the view factor from the emitter to the receiver (PV diode). This approach also sidesteps the difficulties of the nanoscale-gap regime, since no gap is required. Photon recycling and reabsorbed power can therefore no longer be considered as a perturbation [153]; instead, new physical effects should arise in this nonperturbative regime. Finite difference time-domain (FDTD) [157] and current transport simulations have shown that an IPSE enables system conversion efficiencies to reach up to 41.8%, using the realistic model for GaSb PV diodes, by nearly eliminating sub-bandgap emission. This corresponds to showing that the 10.9% gap from the ideal efficiency value observed in previous work [6] can now be reduced to 4.3% using IPSEs. Arguably, the IPSE

creates a nonzero chemical potential for photon emission using a purely thermal input source, which is a fundamentally distinctive physical behavior akin to light-emitting diodes [158]. Further, the IPSE is relatively amenable to fabrication in the near term, with key features already achieved in previous experimental work [20, 143–146].

2.2 Design of the Integrated Photonic Crystal Selective Emitter

As shown in Fig. 2.1(a), the IPSE consists of a metal two-dimensional (2-D) PhC and a chirped quarter-wave stack (QWS), which are brought to an extremely small separation. The metal 2-D PhC consists of an array of holes filled entirely with low refractive index material, so that the bilayer structure can be fabricated and firmly attached to the emitter without greatly increasing sub-bandgap emission [159, 160]. The chirped QWS structure placed directly atop the PhC consists of two alternating dielectric materials with different refractive indices. In such an integrated design, where the view factor approaches unity, all thermal photons emitted from the front surface of the 2-D PhC would be filtered.

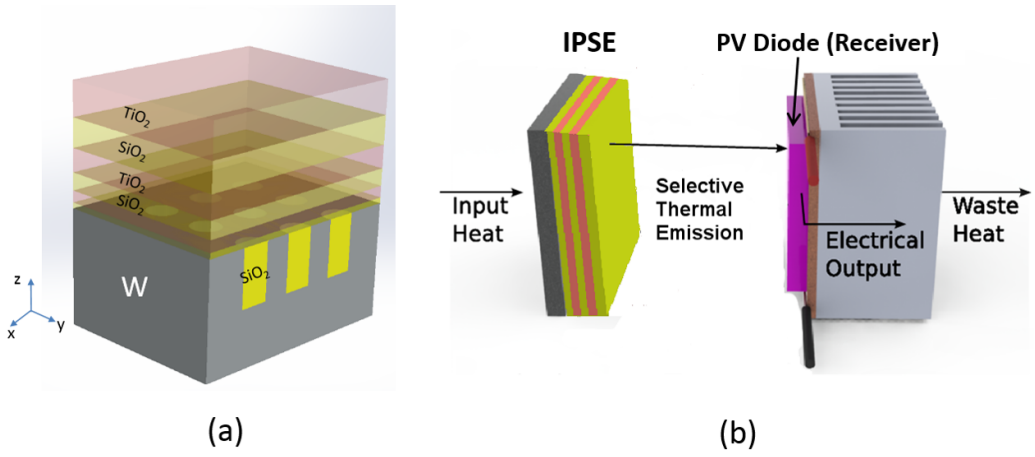

Fig. 2.1. Design of the IPSE. (a) Cutaway view of the IPSE, made of a chirped one-dimensional PhC filter, consisting of low-index SiO_2 and high-index TiO_2, integrated with a 2-D tungsten PhC structure filled with SiO_2. (b) Schematic depicting a high-performance TPV system utilizing an IPSE.

In this work, the IPSE is examined directly as a whole using a TPV simulation tool developed by the present authors [161, 162]. The emittance spectrum associated with the design is first calculated using an FDTD simulation method known as MIT electromagnetic equation propagation [163]. Then the currentvoltage (J-V) relation for TPV cells is calculated from the emittance spectrum assuming zero series resistance, as in previous work [153]. The effect of finite series resistance is considered later in this work. The power output is then calculated by solving for the maximum power point via $d(JV)/dV = 0$ (equivalently $I_{sc}V_{oc}FF$, where I_{sc} is the short-circuit current, V_{oc} is the open-circuit voltage and FF is the fill factor). Based on the experimental performance of metalorganic vapor phase epitaxial grown low-bandgap III-V PV diodes from Lincoln Laboratories, an average external quantum efficiency of 82% is assumed [153]. The thermal power input is calculated as the total thermal emission P_{em} less the power reabsorbed P_{re} by the emitter. The system conversion efficiency η is then finally given as

$$\eta = \frac{I_{sc}V_{oc}FF}{P_{em} - P_{re}} \tag{2.1}$$

The geometry of the 2-D PhC emitter follows from our recent work on the performance of tungsten (W) PhC selective emitters [6]. Previously, we found that for a W PhC emitter paired with a cold-side rugate filter [164], the highest estimated $\eta = 35.2\%$ occurs at $E_g = 0.7$ eV and $T = 1573$ K, where E_g is the bandgap energy of the PV diode and T is the operating temperature of the emitter. A suitable geometry for selective emission is determined using the technique of quality factor-matching, in which the radiative coupling rate is matched with the material absorption rate to achieve full absorption. In this proposed structure, the array of holes is filled with SiO_2; therefore, the optimal 2-D hole array geometry needs to be rescaled by the refractive index $n_{SiO_2} = 1.46$, giving $r = 0.260$ μm, $d = 2.117$ μm, and $a_x = a_y = 0.636$ μm. Here, r is the hole radius, d is the hole depth, and a_x and a_y are the periods of the array along the x and y directions. Maxwells equations make

these photonic structures completely scalable in principle [80]. The key constraint is to find a pair of materials with sufficient refractive index values and very low losses; this criterion generally excludes frequencies in ultraviolet or above.

It will now be shown that IPSEs can lead to performance improvements over bare W PhCs, which help approach the limits of an ideal selective emitter. For specificity, we consider the case of a bandgap $E_g = 0.7$ eV. The ideal selective emitter for such a bandgap has a top hat emittance spectrum depicted by the red curves in Fig. 2.2, corresponding to 100% emittance between 1300 and 1771 nm, and zero emittance elsewhere. This property fully suppresses sub-bandgap losses and greatly reduces carrier thermalization [11], yielding an ideal emission conversion efficiency $\eta_{ideal} = 46.1\%$.

2.2.1 Integrated Photonic Crystal Selective Emitter with Chirped Quarter-Wave Stack

Now we consider the efficiency of an appropriate IPSE structure for comparison. The integrated SiO_2/TiO_2 ($n_{TiO_2} = 2.50$) QWS has a cutoff wavelength at 1771 nm, matching the PV bandgap energy of 0.7 eV. The bilayer structure has an initial bilayer thickness of 497 nm, which is chirped exponentially upward at a rate of 5.1% per bilayer to make a broadband filter. It is important to limit the chirping rate and material choices here to suppress the emergence of anomalies in the photonic density of states (analogous to a Wannier-Stark ladder in electronic structures). At the selected chirping rate, the emittance spectrum of a 15-period QWS IPSE is simulated and displayed as a black curve in Fig. 2.2(a). At $T = 1573$ K, the spectrally averaged effective emittance from 1771 to 9000 nm is $\epsilon_{eff} = 0.02$; for useful emission, it is $\epsilon_{eff} = 0.71$. These calculations assume that the material parameters are unchanged from literature values at the targeted temperature [165]. Compared to the bare W PhC (without an integrated filter) results, shown as the blue curve in Fig. 2.2(a), it is immediately obvious that the IPSE strongly suppresses parasitic emittance from the cutoff wavelength of 1771 up to 4000 nm, but strong parasitic emission occurs

between 4000 and 9000 nm, as shown in Fig. 2.2(a). The conversion efficiency η calculated using the emittance spectrum up to 9000 nm is 38.2%. Thus, an increase in η of 3% is achieved at 1573 K, since the major parasitic emission is beyond the blackbody peak.

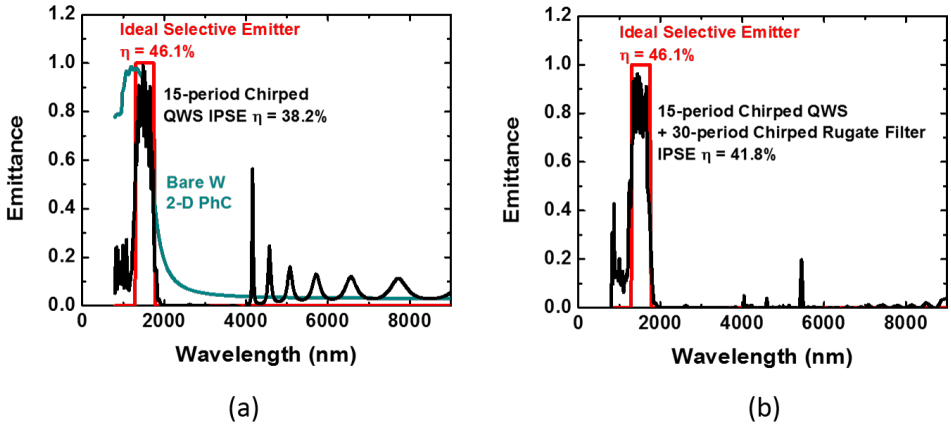

Fig. 2.2. Emittance spectrum comparisons. (a) Emittance spectrum of 15-period QWS IPSE (black) in comparison to the emittance spectrum of an ideal emitter (red) and a bare W photonic crystal emitter (blue). Parasitic emission from 1771 to 4000 nm is effectively suppressed, but strong parasitic emission occurs beyond 4000 nm. (b) Emittance spectrum of 15-period QWS + 30-period rugate filter IPSE (black) in comparison to the emittance spectrum of an ideal emitter (red).

The performance of the 15-period QWS IPSE here is still 7.89% below the ideal case. The reason for this difference can be analyzed by comparing with the ideal emitter and quantifying the loss mechanism. Three sources of efficiency losses are considered in Table 2.1: (1) emission at wavelengths shorter than 1300 nm, (2) imperfect emission between 1300 and 1771 nm, and (3) parasitic emission at wavelengths from 1771 to 9000 nm. Wavelengths beyond 9000 nm are emitted even at room temperature; the power is small enough in this region to be neglected. Even if we assume a constant emittance of 0.1 from 9000 up to 15,000 nm, the efficiency loss at 1573

K is <0.1%. The primary nonideality comes from parasitic emission, particularly between 4000 and 9000 nm, which contributes a 4% efficiency loss. Therefore, further suppression of the parasitic emission is required. However, increasing the number of bilayers or the chirping rate will shift the high-order reflections to longer wavelengths, suppressing useful emission between 1300 and 1771 nm, and thus is not a viable option.

Table 2.1.
Classification of physical loss mechanisms affecting TPV efficiency η. By modifying the structure of the IPSE, parasitic emission is reduced while useful emission is enhanced, allowing efficiencies to more closely approach the ideal value of 46.1%.

IPSE structure	η (%)	**Total losses in efficiency (%)**	**Short-wavelength emission (%)**	**Insufficient emission (%)**	**Parasitic emission (%)**
QWS IPSE	38.2	7.89	0.80	1.71	5.38
QWS + rugate filter IPSE	41.8	4.29	0.89	1.66	1.74

2.2.2 Integrated Photonic Crystal Selective Emitter with Chirped Quarter-Wave Stack and Chirped Rugate Filter

In order to suppress parasitic emission while preserving useful emission, we instead introduce a chirped 30-period rugate filter on top of the 15-bilayer IPSE structure. Rugate filters use a different refractive index profile, more akin to a sinusoid, which eliminates higher-order reflections [146]. In this case, our rugate filter is composed of six different materials, with varying indices of refraction from $n_{SiO_2} = 1.46$ to $n_{TiO_2} = 2.50$. Each layer thickness is determined by following the type C design from Carniglia [164], with the cutoff wavelength designed at 3500 nm and an exponential

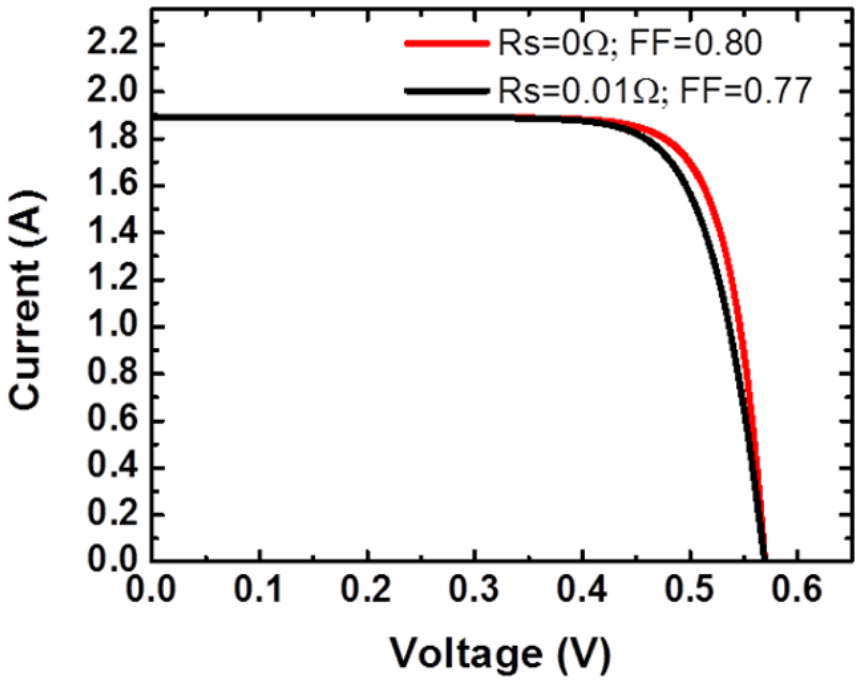

Fig. 2.3. Calculated light I-V curve for the experimentally based GaSb PV diode, when illuminated by the 15-period QWS + 30-period rugate filter IPSE at 1573 K. Two cases are shown: series resistance $R_s = 0\ \Omega$ (red) and $R_s = 0.01\ \Omega$ (black).

chirping rate of 3.5%. The simulated emittance spectrum in Fig. 2.2(b) shows that the rugate filter provides effective suppression of parasitic emission from 4000 to 9000 nm. The effective emittance of parasitic emission from 1771 to 9000 nm is greatly reduced to $\epsilon_{eff} = 0.004$, while that of useful emission actually increases to $\epsilon_{eff} = 0.74$, using the same assumptions as before. Overall conversion efficiency η is thus increased to 41.8%. Similar analysis of loss mechanism for the IPSE with 30-period rugate filter on top is summarized in Table 2.1. The efficiency loss due to the first two categories is close to the 15-bilayer IPSE structure, showing that the emission at wavelengths shorter than 1771 nm is preserved by the pass-band of the rugate filter. The parasitic loss is significantly reduced by the broader stop-band of the rugate filter. Overall, the efficiency gap from the ideal case is substantially reduced to 4.3%, which is less

than two-fifths of the original gap previously seen in the literature [6].

Assuming the presence of a large-area passive heat sink with convective and radiative cooling available on its outer surface, the best IPSE design leaves the temperature of the PV diode at 1.5 K above ambient when illuminated. It was also assumed that the PV diode has zero series resistance. Here, we consider the impact of a finite series resistance on the system conversion efficiency. A typical GaSb PV diode produced by JX Crystals has a series resistance $R_s = 0.01\ \Omega$ (the value is fitted from the experimental I-V curve under illumination of a 1200 °C emitter provided by JX Crystals). The light I-V curve of GaSb PV diode illuminated by the 15-period QWS + 30-period rugate filter IPSE at 1573 K is calculated with $R_s = 0.01\ \Omega$, as seen by the black curve in Fig. 2.3. Compared to the case where zero R_s is assumed, the fill factor decreases from 80 to 77% when $R_s = 0.01\ \Omega$, reducing the conversion efficiency to $\eta = 40.3\%$.

2.3 Perturbative and Nonperturbative Photon Recycling

Next, the new physical effects that arise in TPV systems that use IPSEs are examined from the aspect of radiative heat transfer. Generally, the differential view factor for the n'th reflection between the emitter and the receiver can be defined as follows:

$$dF_n = \frac{\cos^2\theta_n}{\pi d_n^2} dA_{n+2}, \tag{2.2}$$

where dF_n is the differential view factor for the n'th reflection; dn is the distance from the original emitter A1 to the n'th reflection image surface A_{n+2} [166]; θ_n is the angle between the surface normal of the differential area dA_1 and the line connecting two differential areas dA_1 and dA_{n+2}. The integrated view factor F_n can be calculated as shown in Ref. [67].

The n'th contribution to the short-circuit current $I_{sc}(\lambda)$ for a given wavelength λ is then calculated by

$$I_{sc}(\lambda) = \sum_{n=0,2...}^{\infty} A_1 \frac{2qcEQE(\lambda)(R_1R_2)^{n/2}\epsilon(\lambda)}{\lambda^4[\exp(\frac{hc}{\lambda kT}) - 1]} F_n = \sum_{n=0,2...}^{\infty} B_n(\lambda)F_n, \tag{2.3}$$

where F_n is the n'th-order view factor and B_n is the coefficient corresponding to the n'th reflection; $EQE(\lambda)$ is the external quantum efficiency of the PV diode; R_1 and R_2 are the reflectivities of the emitter and receiver, respectively; h is the Plancks constant; k is the Boltzmanns constant; c is the speed of light. Since R_2 is very small for photons above the bandgap, $I_{sc}(\lambda)$ can be approximated as $I_{sc}(\lambda) \approx B_0F_0$.

When a cold-side filter is applied, photon recycling in the TPV system is expressed using a power series (in the perturbative regime). The recycled power $P_{re}(\lambda)$ at a given wavelength λ can be calculated as

$$P_{re}(\lambda) = \sum_{n=1,3...}^{\infty} A_1 I_{BB}(\lambda) R_2^{(n+1)/2} R_1^{(n-1)/2} (1 - R_1)\epsilon(\lambda)F_n = \sum_{n=1,3...}^{\infty} C_n(\lambda)F_n, \tag{2.4}$$

where $I_{BB}(\lambda)$ is the blackbody radiation power density at wavelength λ and C_n is the coefficient corresponding to the n'th reflection. Specifically, for TPV systems using selective emitters and nonideal filters, $P_{re}(\lambda)$ can be approximated as $P_{re}(\lambda) \approx C_1F_1$. Substituting I_{sc} and P_{re} in Eq. 2.1 with Eq. 2.3 and 2.4, the TPV conversion efficiency, including photon recycling, can be calculated as

$$\eta = \frac{BV_{oc}FF}{P_{em}(1 - \kappa)} F_{eff}, \tag{2.5}$$

$$F_{eff} \equiv \frac{F_0(1 - \kappa)}{1 - \kappa F_1}, \tag{2.6}$$

where $B = \int B_0(\lambda)d\lambda$; $C = \int C_1(\lambda)d\lambda$; F_{eff} is defined as the effective view factor,

whose physical meaning is the ratio between the useful photons received by the receiver and the total emitted photons excluding the reabsorbed ones; $\kappa \equiv C/P_{em}$ is the ratio between the maximum recycled power and the initial emitted power P_{em}; V_{oc} is the open-circuit voltage. Since the effective view factor is not linearly dependent on the actual view factor F_0, a nonlinear dependence of η on the view factor is expected in the perturbative regime.

However, in the nonperturbative regime, the view factor from the emitter to the filter approaches unity, while the view factor from the IPSE to the PV diode is still F_0. The reabsorbed power P_{re} is now a constant instead of a function of F_1 (or F_0). Thus, $F_{eff} = F_0$, so Eq. 2.5 should be modified as

$$\eta = \frac{B' V_{oc} FF}{P_{em}(1-\kappa)} F_0, \tag{2.7}$$

where $B' = \int B'_0(\lambda) d\lambda$; $B'_0(\lambda)$ is similarly defined by Eq. 2.3 but using different parameters. Since the photon recycling perturbation is eliminated, linear view factor dependence is thus expected in the nonperturbative regime.

The system conversion efficiency of a TPV system using IPSE is now simulated at different view factors (with respect to the receiver), using a TPV simulation tool developed by the authors. For comparison, the same approach is also employed to simulate a TPV system with a cold-side rugate filter attached to the PV diode (in the perturbative regime). Eq. 2.5 and 2.7 are then used to fit the results of the perturbative and the nonperturbative cases respectively, as shown in Fig. 2.4. The fits are in perfect agreement with the simulation results in each case. The linear view factor dependence of a TPV system where IPSE is applied shows that the photon recycling is no longer influenced by the spacing between the emitter and the receiver. Thus, an extremely high view factor for sufficient photon recycling is no longer necessary. The distinction between the behavior in the perturbative and nonperturbative regimes is very accurately described by Eq. 2.5 and 2.7. Therefore, F_{eff} correctly captures the physics of photon recycling in TPV systems and can

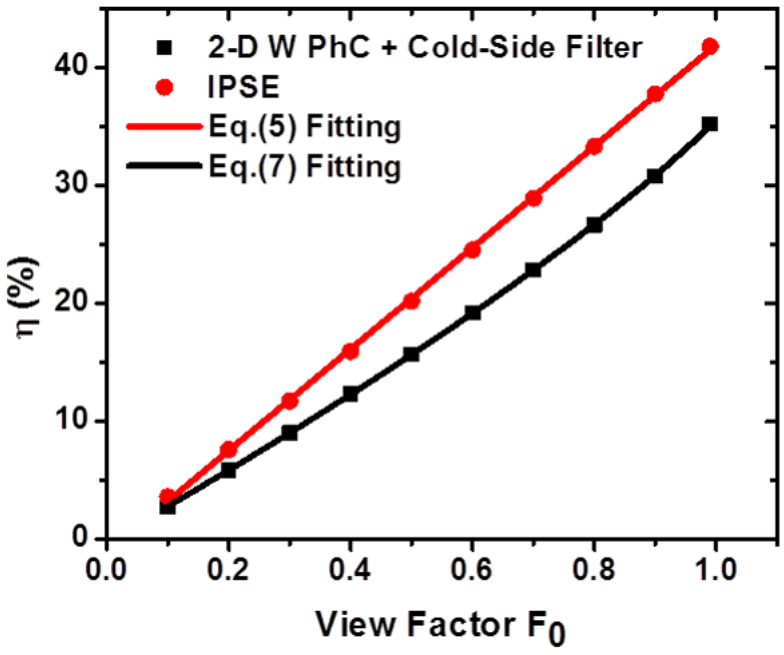

Fig. 2.4. Conversion efficiency η as a function of view factor F_0 for a TPV system using a 15-period QWS + 30-period rugate filter IPSE and a TPV system using a cold-side rugate filter. The distinctive behaviors of the perturbative and nonperturbative regimes are successfully described by Eq. 2.5 and 2.7, which incorporate the analytically calculated effective view factor.

be used as a metric to describe most TPV systems (both in the perturbative and nonperturbative regimes).

2.4 Thermophotovoltaics System with Photonic Crystal Waveguide

Furthermore, F_{eff} can be increased much further by surrounding the gap between the emitter and the receiver with a waveguide as shown in Fig. 2.5(a). The requirements for high reflectivity at specific wavelengths and low thermal conductivity could be satisfied by the use of dielectric PhC waveguides. To include the impact of the waveguide on the TPV systems, the expressions for F_0 and F_1 can be generalized as

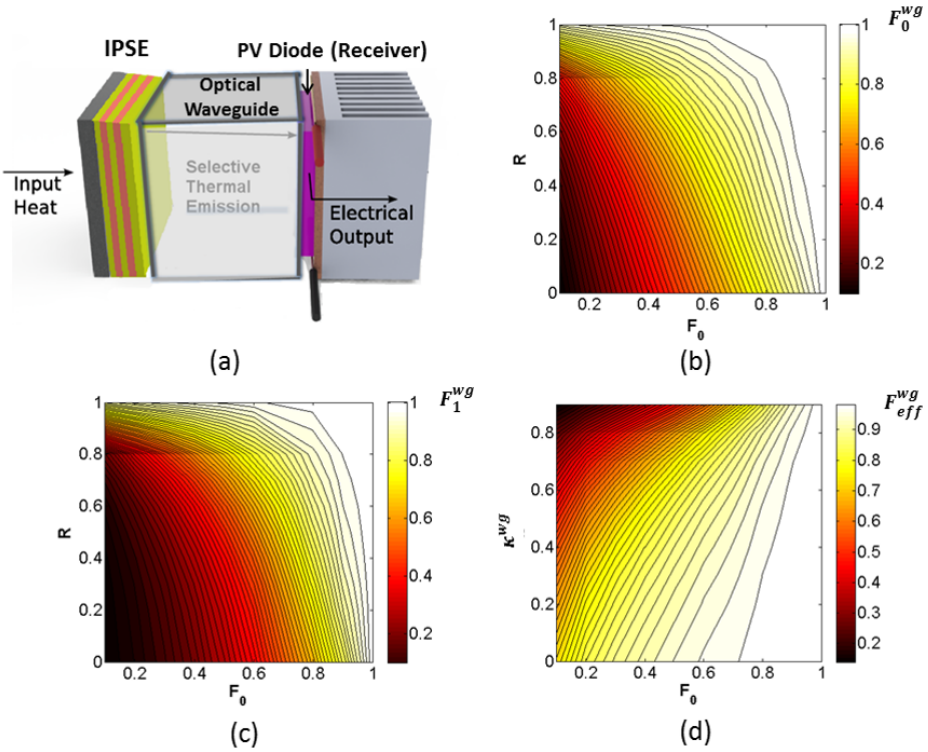

Fig. 2.5. Waveguide and contour plots. (a) A TPV IPSE surrounded by a dielectric waveguide reduces the need for close alignment between emitter and receiver for improved efficiency. (b) Contour plot of F_0^{wg}as a function of original view factor F_0 and reflectivity R of the waveguide. (c) Contour plot of F_1^{wg} as a function of original view factor F_0 and reflectivity R of the waveguide. (d) Contour plot of F_{eff}^{wg} as a function of original view factor F_0 and maximum recycled power ratio κ^{wg} contributed only by the waveguide.

$$F_0^{wg} \approx F_0 + (1 - F_0)\frac{f^2 R\gamma}{1 - Rf(1-\gamma)}, \tag{2.8}$$

$$F_1^{wg} \approx F_1 + (F_0^{wg} - F_1)\frac{f^2 R\gamma}{1 - Rf(1-\gamma)}, \tag{2.9}$$

where f represents both the view factor from the emitter to the waveguide and from the waveguide to the receiver, respectively; R is the reflectivity of the sidewalls of the

waveguide; γ is the area ratio between the emitter and the waveguide; all the view factors with the superscript wg capture the effect of waveguiding. Fig. 2.5(b) and (c) show the contour plots of both F_0^{wg} and F_1^{wg} as functions of the original view factor F_0 and the reflectivity R of waveguide, assuming that the waveguide is in proximity to both the emitter and the receiver ($f = 0.99$) and the cross-section of the waveguide is the same as the surface area of the emitter. Significant improvement in F_0^{wg} and F_1^{wg} can be achieved when a highly reflective waveguide is applied. Especially when waveguides with $R \approx 0.99$ is added, both F_0^{wg} and F_1^{wg} will be close to unity even with an original view factor as low as 0.28, a view factor corresponding to a length of waveguide enough to make the thermal power conduction less than 0.1% of the overall heat transfer. From Eq. 2.3 and 2.4, it can be predicted that both the short-circuit current and the reabsorbed power will be considerably improved if a highly reflective waveguide is used. The effective view factor F_{eff}^{wg} including the waveguide can be calculated as

$$F_{eff}^{wg} \equiv \frac{F_0^{wg}(1-\kappa^{wg})}{1-\kappa^{wg}F_1^{wg}}, \tag{2.10}$$

where κ^{wg} is the ratio between the maximum recycled power contributed by the waveguide only to the initial emitted power P_{em}. Fig. 2.5(d) shows the contour plot of F_{eff}^{wg} as a function of κ^{wg} and the original view factor F_0, assuming a realistic waveguide with $R = 0.95$ is added. The IPSE almost eliminates the need for photon recycling between the emitter and the PV diode. Therefore, κ^{wg} in this case is close to zero, giving an F_{eff}^{wg} close to 0.9, even with $F_0 = 0.28$. It is obvious that using a waveguide can greatly improve F_{eff} , which could be extremely useful for maintaining physical separation between a hot emitter and cold PV diode.

2.5 Conclusion

In conclusion, the IPSE and waveguide eliminate losses, due to the nonideal photon recycling between the emitter and the receiver, as well as the difficulty of close alignment between a hot emitter and cold receiver. This approach can increase the theoretical conversion efficiency of a TPV system from the prior value of 35.2% up to 41.8% at 1573 K. Such behavior is described by analytical expressions based on our extended definition of the effective view factor F_{eff}. Our approach captures the physics of TPV systems where Kirchhoff's law cannot be applied directly, particularly in the presence of photon recycling and waveguides. It is also consistent with previous results in the field [20, 159, 160]. This extended definition of effective view factor can be broadly applied to any TPV system, and could even lead to further improvements in system conversion efficiencies and experimental fabrication, through the use of dielectric PhC waveguides.

3. PHOTONIC CRYSTAL SELECTIVE STRUCTURES FOR SOLAR THERMOPHOTOVOLTAICS[1]

Solar thermophotovoltaic (STPV) systems convert sunlight into electricity by first converting incoming sunlight into heat and then generate electricity from heat via thermophotovoltaic process. The efficiency of this overall conversion strongly depends on the spectral selectivity of both the solar absorber and the thermal emitter, both can be engineered by materials and the photonic design. Though existing nanophotonic designs based on refractory materials have shown promising results for high concentration STPV applications, high performance under moderate solar concentration still remains a challenge. In this work, we propose an integrated photonic crystal selective structure (IPSS), which combines 2D photonic crystals and filters into a single device. The IPSS is a monolithic structure that can collect solar heat on one side and emit above-bandgap photons on the other. Finite difference time domain (FDTD) simulations show that the IPSS can be engineered to achieve near-optimal performance as solar absorbers and thermal emitters. The net result is an increase in sunlight-to-electricity conversion efficiency above 24.3% at 100 suns concentration using a $Ga_{0.42}In_{0.58}As$ PV diode with a bandgap of 0.7 eV.

3.1 Introduction

Solar thermophotovoltaic (STPV) systems convert sunlight into electricity via two steps. The incident solar power is first converted into heat, elevating the temperature of a thermal emitter. Then, thermal emission from the emitter is converted into electricity through photovoltaic effect. The efficiency of STPV is therefore depen-

[1]Adapted from: Z. Zhou, E. Sakr, O. Yehia, A. Mathur, and P. Bermel, "Photonic crystal selective structures for solar thermophotovoltaics," *MRS Advances*, vol. 1, no. 59, 2016.

dent on both the thermal transfer efficiency of the selective absorber [44] and the system conversion efficiency of TPV [153]. Both components can be engineered by materials and the photonic design. Metal-dielectric composites like cermets [47] and semiconductor-metal tandem [23] are demonstrated as strong candidates for operations under conditions such as 100 suns concentration and 1000 K. It is also demonstrated that with proper design and fabrication, single wall carbon nanotubes exhibit selective absorption as well [167]. For artificial photonic structures, plasmonic selective absorbers [28] were proposed due to its surface plasmon enhanced absorption. Photonic crystals made of refractory metals [6] were proposed to be highly efficient selective solar absorbers under high temperature ($\geq$ 1000 K) and high solar concentrations ($\sim$ 1000 suns) [33, 55, 57]. However, it is still a challenge to design a selective solar absorber that has high thermal transfer efficiency at high operating temperatures ($\sim$ 1500 K) and moderate solar concentrations ($\leq$ 100 suns), a preferred condition that allows integration with highly efficient TPV systems and better system reliability by alleviating complexities of dual-axis solar tracking systems.

The main challenge is that under low solar concentration, thermal re-radiation loss should be strongly suppressed. However, high operating temperatures make the blackbody radiation spectrum overlapping with the solar spectrum, making it very hard to balance between low thermal re-radiation and high solar absorption. Furthermore, system integration may benefit from the use of selective solar absorbers and selective emitters that use similar materials and structures. But in most cases, selective emitters and selective solar absorbers have different requirements in their emittance spectra [23]. Therefore, achieving this together with the aforementioned constraints can be even harder. In order to address this challenge, an integrated photonic crystal selective absorber (IPSA) design is proposed based on the selective emitter design in [168].

Similar to the integrated photonic crystal selective emitter (IPSE) proposed in Chapter 2, the IPSA combines a 2D photonic crystal with a chirped rugate filter into a single device. By directly stacking the rugate filter on top of the 2D PhC,

the sub-bandgap photon recycling [153] shifts to a non-perturbative regime instead of a perturbative one. The net effect is a strong selectivity in the absorptance spectrum. We show that when the proposed IPSA is combined with an IPSE, the STPV conversion efficiency can be as high as 24.3% at 1450 K and 100 suns.

3.2 Integrated Photonic Crystal Selective Structure

Photonic crystal structures are proved to be versatile in terms of tailoring emittance spectrum, making it possible to cover the spectral requirements of both selective emitter and selective absorber. It has been shown that an integrated photonic crystal is strongly selective in its emittance spectrum [168, 169]. In order to achieve high STPV conversion efficiencies under the constraints of high temperature and moderate solar concentration, we investigate an integrated photonic crystal structure (IPSS) that combines a selective absorber with a selective emitter as a monolithic device.

The IPSS consists of an IPSA and IPSE. For the IPSA structure, the integrated filter should exhibit a sharp cut-off in its transmittance spectrum that resembles Fig. 1.6. At an operating temperature of 1500 K and a solar concentration of 100 suns, the optimal cut-off wavelength is ~ 1 μm [170]. To achieve that, a 60-period chirped rugate filter is designed. It consists of twenty materials with refractive indices ranging from $n_{SiO_2} = 1.46$ to $n_{TiO_2} = 2.50$. The permittivity of each layer, as shown in the inset of Fig. 3.1, is calculated following the design principle discussed in [164]. The transmittance spectrum of the rugate filter is simulated using S4 [171], as shown in Fig. 3.1. With the initial period thickness of 0.349 μm and a chirping rate of 3.5%, the rugate filter exhibits a broad stopband, extending from 1.3 μm to 10 μm. Later, we will see that such broadband filtering allows the IPSA to have low ($< 10\%$) spectrally averaged absorptance $\overline{\alpha}$ [153] even at a temperature of 1500 K.

The 2D PhC is made of tungsten (W) and has a square lattice with period $a = 0.470$ μm, hole radius $r = 0.293$ μm and hole depth $d = 2.386$ μm. Since the diameter of the holes are larger than the period, the PhC appears to be an array of W pillars,

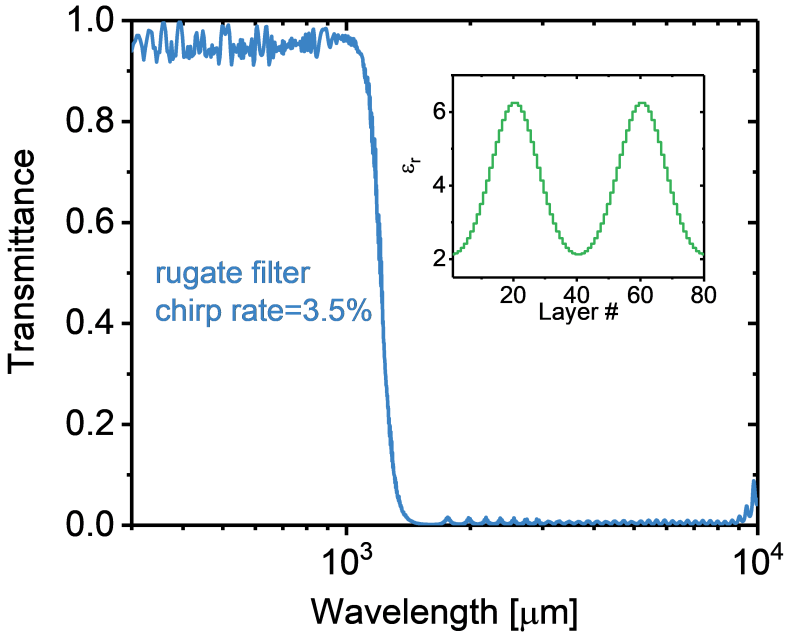

Fig. 3.1. Transmittance spectrum of the designed rugate filter to be integrated on IPSA. It has a sharp cut-off near 1 μm that matches with the theoretical optimal value. The inset shows the relative permittivity (ϵ_r) of each layer in the first two periods of the filter.

as schematically shown in Fig. 3.2(a). In order to integrate the filter with the 2D W PhC, spacing between the pillars are filled with the low index material SiO_2. For the IPSE, we choose the 15 bilayer integrated structure proposed in reference [169]. Both IPSA and IPSE have similar structural design and the 2D PhCs are both made of W. Therefore, when applied to an STPV system, the IPSA can be directly combined with the IPSE back to back as a single piece of IPSS absorber/emitter pair.

The absorptance spectrum of the designed IPSA is calculated using a finite difference time domain (FDTD) [157] method known as MEEP [163]. There is a numerical error no greater than 2.9% in the absorptance calculation beyond 4 μm due to the finite resolution and time. As shown in Fig. 3.2(b), the absorptance of IPSA has strong spectral selectivity near 1.3 μm. The enhanced absorptance below this cut-off

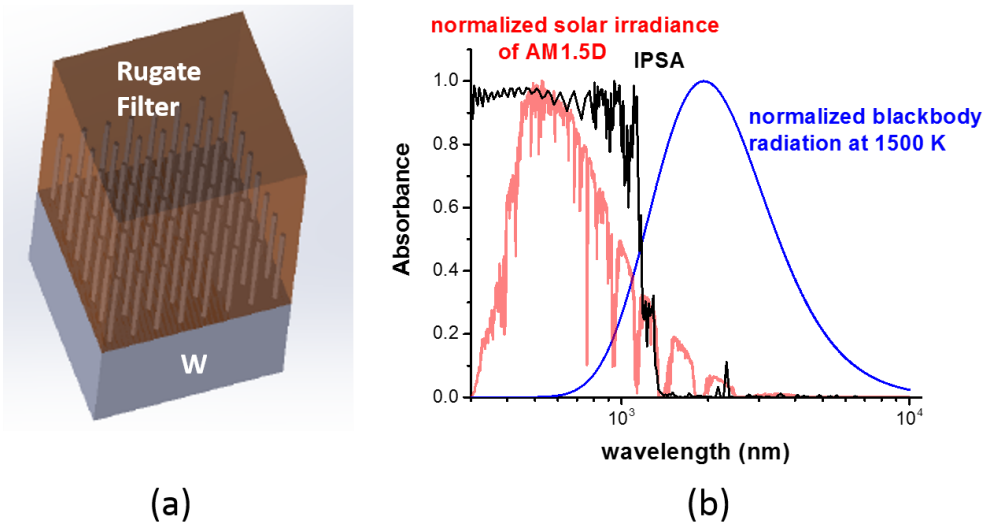

Fig. 3.2. (a) Schematics of the IPSA structure; (b) Absorptance spectrum of the IPSA (black) plotted together with the normalized AM1.5D solar irradiance (red) and the normalized blackbody radiation at 1500 K (blue). The steep cut-off at 1.3 μm allows strong absorption of most solar irradiance while keeping the thermal emission low.

covers the majority of the solar irradiance, yielding a spectrally averaged absorptance $\overline{\alpha} = 0.7686$. Beyond this cut-off, most of the thermal emission is suppressed, as can be seen in Fig. 3.2(b). The absorptance spectrum of the IPSA is calculated up to 7 μm and the broad stopband of the rugate filter (shown in Fig. 3.1) should make the absorptance negligible from this point to 10 μm . At a temperature of 1500 K for example, a typical value for STPV application, the IPSA has a spectrally averaged emittance [153] $\bar{\epsilon} = 0.0415$. The thermal transfer efficiency η_t at 100 suns solar concentration is then 65.0%, 6.9% below the maximum thermal transfer efficiency of 71.9% under the same condition (100 suns, 1500 K). In order to understand the performance of the proposed IPSA structure at various temperatures and solar concentrations, a contour plot of thermal transfer efficiency η_t as a function of temperature and solar concentration, as shown in Fig. 3.3, is calculated. It is obvious that η_t of the IPSA follows the same trend as theoretically expected: at a given con-

centration, η_t decreases as temperature increases; at a given temperature, η_t increases with concentration. It should be noted that even at low solar concentrations ($\leq$ 100 suns) and high temperatures ($>$ 1000 K), IPSA still gives high η_t, thanks to its strong selectivity. This offers the opportunity to achieve good STPV performance at low solar concentrations, where only single axis precision tracking [172] is needed for highly efficient solar concentration, greatly reducing the system complexity.

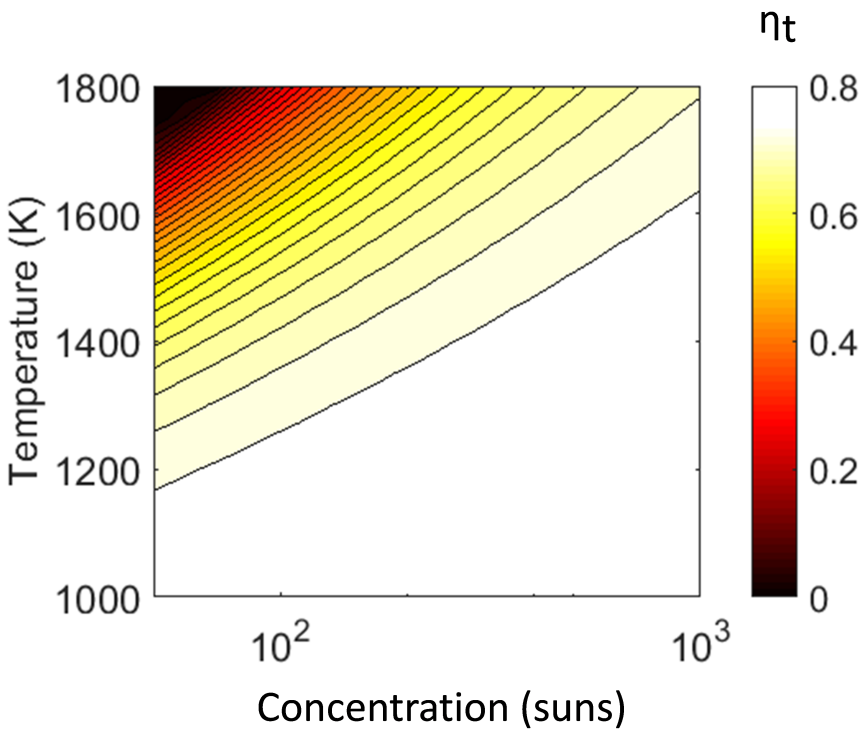

Fig. 3.3. Thermal transfer efficiency η_t as a function of temperature and solar concentration. For IPSA, the slight variation of η_t with concentrations at a given temperature makes it possible for low concentration STPV applications.

For a given solar concentration, higher temperature increases η_t while decreasing TPV conversion efficiency η_{tpv}. Such intrinsic trade-off between η_t and η_{tpv} requires the investigation of the IPSS as an entire whole. Therefore, we calculate a contour plot of STPV conversion efficiency η_{stpv} for the IPSS as a function of temperature

and solar concentration, neglecting concentration losses. The value of η_{tpv} at various temperatures for a PV diode with a bandgap of 0.7 eV ($Ga_{0.42}In_{0.58}As$) is calculated using current transport simulations available on nanoHUB.org [173]. As shown in Fig. 3.4, for each given solar concentration, an optimal temperature can be found. For the proposed IPSS structure under 100 suns concentration, the optimal temperature is 1450 K, where the IPSA has $\bar{\epsilon} = 0.0354$ and $\eta_t = 68.0\%$. Assuming that the IPSE is at the same temperature as the IPSA in equilibrium, then $\eta_{tpv} = 35.7\%$, yielding $\eta_{stpv} = 24.3\%$.

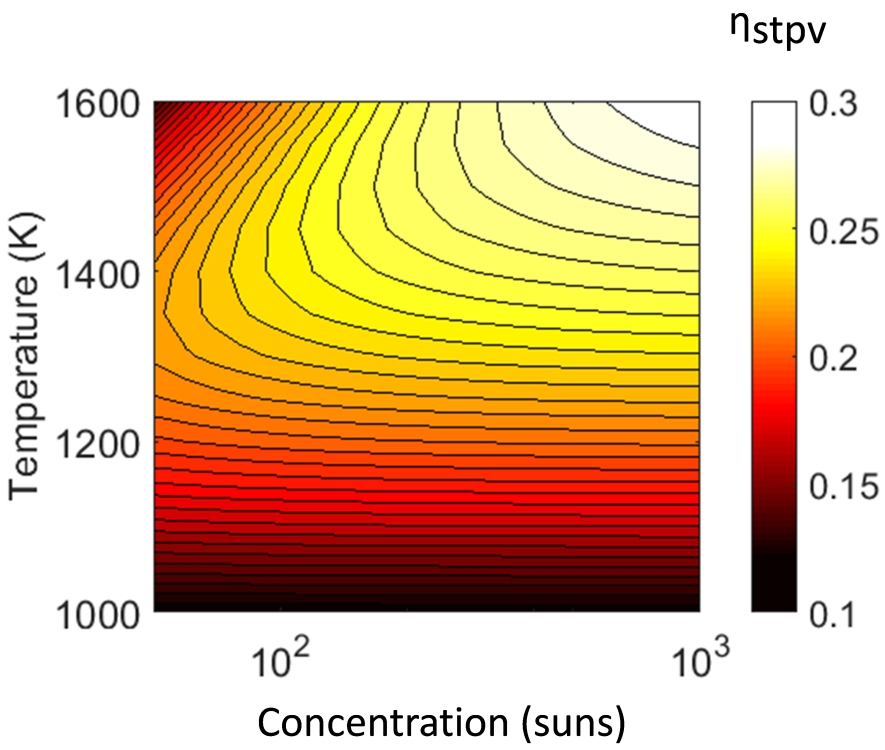

Fig. 3.4. STPV conversion efficiency as a function of temperature and solar concentration. For a given concentration of 100 suns, the optimal temperature is 1450 K, yielding $\eta_{stpv} = 24.3\%$

3.3 Conclusions

A high-performance selective solar absorber is proposed for STPV applications with moderate solar concentrations ($\sim$ 100 suns) and high operating temperatures ($\sim$ 1500 K). We showed that through a properly designed integrated photonic crystal structure, near-optimal thermal transfer efficiency is estimated. When the proposed IPSA is combined with an IPSE and forms a monolithic IPSS (absorber/emitter assembly), high STPV efficiencies can be achieved. We report a theoretical STPV conversion efficiency of 24.3% under 100 suns and 1450 K using IPSS. This result approaches the highest reported efficiency of a single-junction solar cell under similar concentrations is 27.6% (Si back -contact solar cell) [174]. Though further investigations on the IPSS are needed for performance optimizations and structural simplification, the proposed design certainly shows a path towards high performance STPV systems under much less stringent requirement of solar concentration, potentially enhancing the cost effectiveness and system reliability of STPVs.

4. HIGH-TEMPERATURE DIRECT THERMAL EMITTANCE MEASUREMENT

4.1 Introduction

In real TPV and STPV applications, spectrally-selective thermal emitters and solar absorbers operate at high temperatures. This imposes a challenge that a proper optical characterization of thermal emitters and solar absorbers should be performed at their operating temperatures [20, 175, 176], since optical properties of most materials are temperature-dependent. Such high-temperature characterization can be challenging due to the requirements of:

(1) a high-vacuum system to prevent oxidation at high-temperature;

(2) a broad spectral range of detection that covers at least near-IR to mid-IR.

To address the challenges listed above, a high-temperature direct thermal emittance measurement setup is designed and constructed. The setup optically couples an ultra-high vacuum chamber with a Fourier-transform Infrared Spectroscopy (FTIR). A complete and consistent measurement procedure, including calibration and background correction, has been developed. As a critical apparatus of the experimental study of spectrally-selective thermal emitters and solar absorbers, the high-temperature direct thermal emittance measurement setup can be used to validate their designs and provide reliable predictions of their performance when implemented in a system.

In this chapter, details of the setup are introduced in Section 4.2, followed by a discussion of components in the measured signal. Based on the understanding of the signal being collected, measurement procedures including calibration and background correction are discussed in Section 4.3. An example measurement is performed as well in Section 4.4, proving the versatility of the measurement.

4.2 Experimental Setup

The basic concept of the measurement is to directly measure the high-temperature thermal emission from a sample, and then calculate its emittance spectrum.

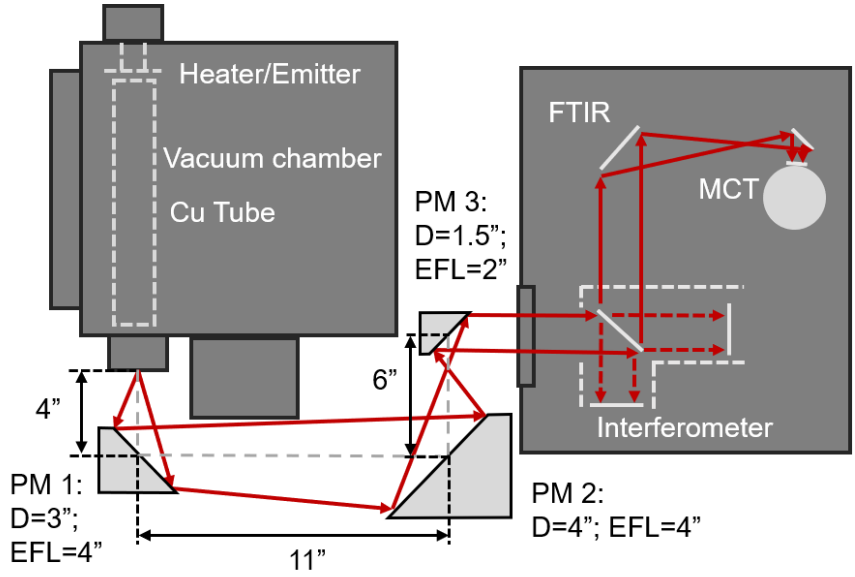

Fig. 4.1. Schematics of a custom-built direct thermal emission measurement system that covers wavelengths from 2 to 10 μm. The sample is heated in a high-vacuum chamber. The thermal emission signal is sent through optical elements, including an interior-polished copper tube and 3 90° off-axis parabolic mirrors (PM) with diameters (D) and effective focal lengths (EFL), to a Nexus 670 FTIR. Relative positions of PMs are labeled. The emission signal is shown by red arrows and the beam center is illustrated by the gray dashed line. Inside the FTIR, the signal passes through a Michelson interferometer and is then detected by a mercury cadmium telluride (MCT) detector.

The first step is to collect the broadband emission signal from the sample. As shown in Fig. 4.1, the setup for direct thermal emittance measurement consists of two major components, an ultra-high vacuum chamber where the sample is heated up to elevated temperature, and an FTIR (Nexus 670, Thermo Fisher Scientific) that measures the broadband emission spectrum. The two components are coupled by an

optical system that consists of a copper tube and 3 off-axis parabolic mirrors (PM 1, PM 2 and PM 3). In the next two sections, the ultra-high vacuum system and the optical system are introduced in detail.

4.2.1 Ultra-high Vacuum System

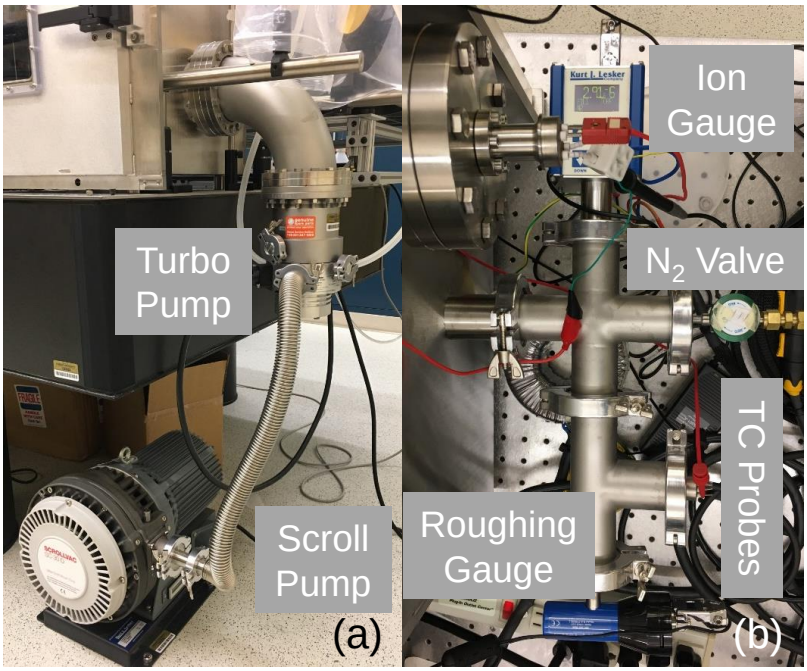

Fig. 4.2. Ultra-high vacuum system. (a) The vacuum chamber is pumped by a turbo pump and a scroll pump connected in series. (b) The vacuum level is monitored by a roughing gauge (3 mTorr and above) and an ion gauge (below 3 mTorr). During sample loading, the vacuum chamber is purged with N_2. The port, TC probe, is for temperature measurements.

To create a vacuum environment that prevents oxidation of samples at high temperatures, a customized ultra-high vacuum chamber (Kurt J. Lesker) is built. Fig. 4.2 (a) shows the pump system that supports the vacuum environment. The chamber is pumped by a turbo pump (Turbovac 151 C, Oerlikon) backed up by a scroll pump (SC 30 D, Oerlikon). As shown in Fig. 4.2 (b), The vacuum level inside the chamber

is monitored by an ion gauge (354, Lesker) for sub-mTorr range and a roughing gauge (275i, Lesker) for above. Occasionally, the chamber has to be opened to switch the tested sample. In such cases, the chamber is purged by N_2 to minimize the adsorption of water vapor and other contamination. In addition to the ports for creating and controlling vacuum environment, there are three ports for high-temperature heating stage, transmission window and electrical/temperature measurement feedthrough, respectively.

4.2.2 Optical System

The optical system is designed to reduce background noises and guide the thermal emission signal over a long distance from inside the vacuum chamber to the FTIR.

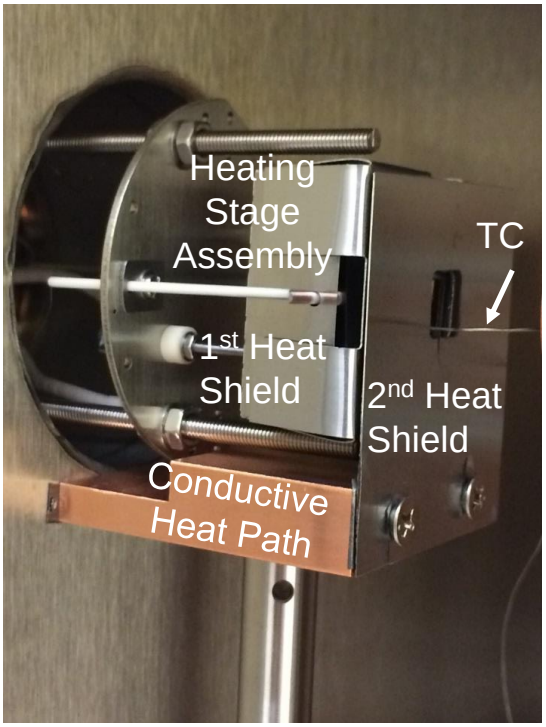

Fig. 4.3. Double heat shield to alleviate background noise from the high-temperature heating stage assembly. The first heat shield is separated from the second heat shield by a vacuum gap. The second heat shield has a conductive heat path to the side wall of the vacuum chamber.

The first component inside the vacuum chamber is a proportional-integral-derivative (PID) controlled resistive heating stage (HTR 1001, Tectra). The heating stage functions as the heat source where emitter samples are placed in direct contact. The temperature is monitored by a type-C thermocouple (TC) that sends voltage signals back to the PID controller. Temperature limit of the heating stage is rated to be 1500 °C, sufficient to cover operating temperatures of high-performance TPVs and STPVs. Fig. 4.3 shows the heating stage from inside the vacuum chamber.

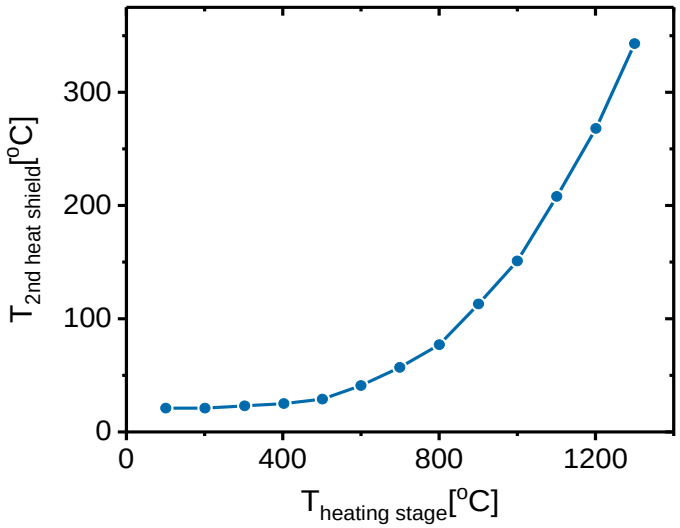

Fig. 4.4. Temperature reduction by the double heat shield structure. The suppressed radiative heat transfer and the enhanced conductive heat dissipation allow significant cooling in the second heat shield, resulting in suppressed background radiation from the heating stage assembly.

The heating stage is a rectangle with a dimension of 35.2 mm × 25.0 mm while most of the emitter samples fabricated are about 11 mm × 11 mm. Therefore, the thermal emission from the uncovered heating stage raises the background noise. To suppress it, a double heatshield structure made of Mo sheet is used, as shown in Fig. 4.3. Both heatshields have a square aperture about 10 mm × 10 mm that is aligned with the emitter sample. The first heat shield reduces thermal radiation due to its

lower temperature and low thermal emissivity. The second heat shield therefore has a lower heat load. Furthermore, it is in direct contact with the sidewall of the chamber via a copper conductive heat path. The net effect is that the temperature of the second heat shield is significantly reduced. As shown in Fig. 4.4, when the heating stage is at 1000 °C the temperature of the second heatshield is measured to be about 150 °C.

Through the apertures of both heat shields, a type-K TC (SCASS-020U-12-SHX, Omega) is inserted to measure the temperature of the sample. As shown in Fig. 4.3, the TC is attached to the front surface of the emitter using conductive paste (Pyro-Duct 597-A, Aremco) that is vacuum compatible at high temperatures.

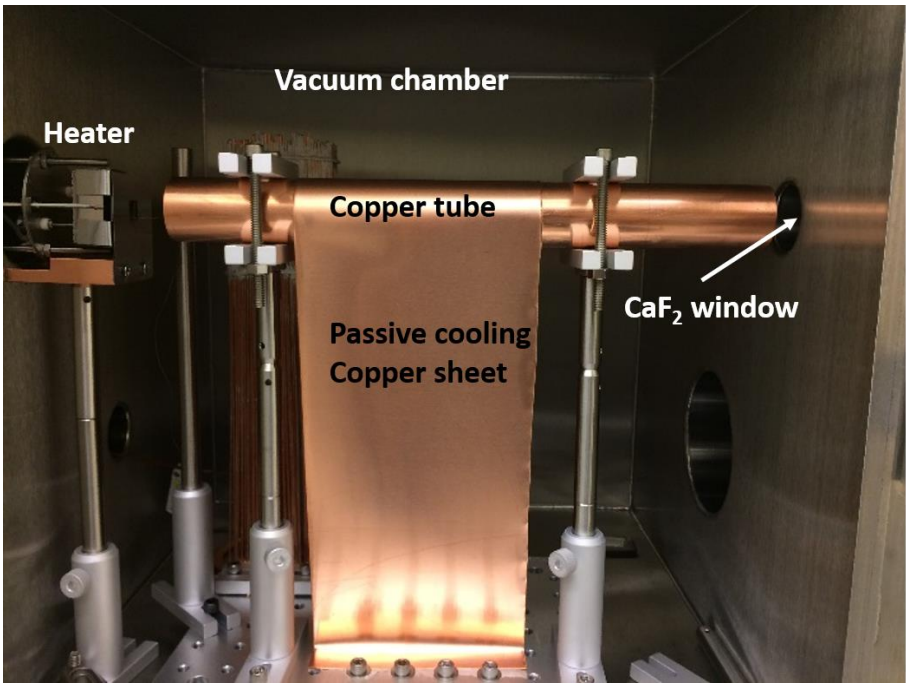

Fig. 4.5. Copper tube that guides the thermal emission signal from the sample mounted on the heating stage to the CaF_2 window on the right-hand side. The copper tube is passively cooled by the copper sheet to alleviate reflectivity variation due to the elevated temperature.

The thermal emission signal, with reduced background noise, is collected by a copper tube, as shown in Fig. 4.5. The tube has an inner diameter of 3.18 cm and a

length of about 31.75 cm, guiding the collected signal across the vacuum chamber to the CaF_2 window (Kurt J. Lesker Company) on the other side. The transmittance spectrum of the window has been measured by the manufacturer and shows high transmission from visible to mid-IR.

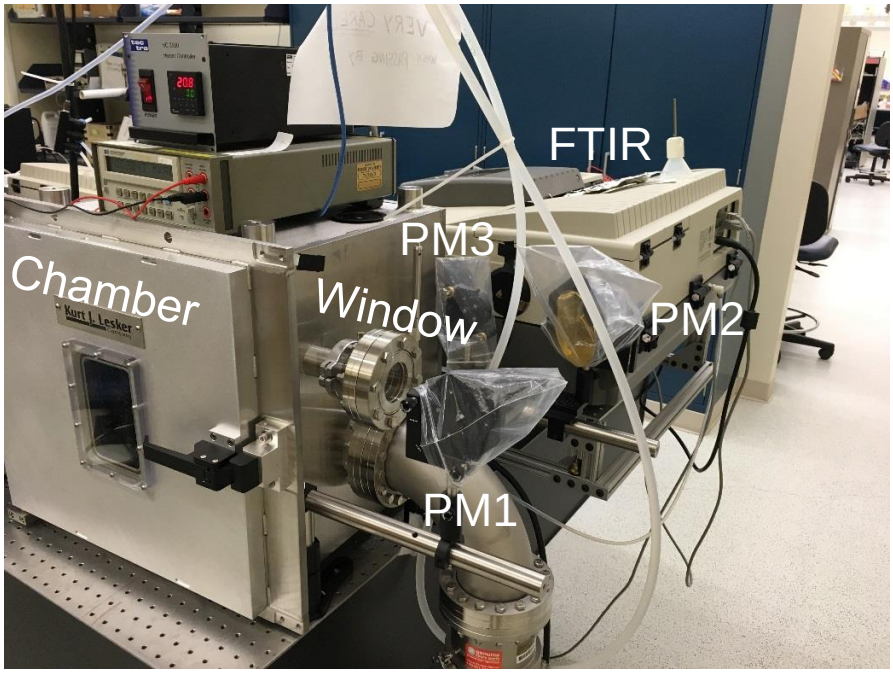

Fig. 4.6. Optical system that couples the vacuum chamber with the FTIR. The beam existing the window is captured and collimated by 3 off-axis parabolic mirrors (PM1, PM2 and PM3). The collimated signal is sent to the FTIR.

After the thermal emission exits the CaF_2 window, it is collected and collimated into the FTIR by three 90° off-axis parabolic mirrors (PM). As shown in Fig. 4.6 and schematically in Fig. 4.1, PM 1 (diameter $D = 3$ inches and an effective focal length $EFL = 4$ inches) collimates the diverging beam from the window. PM 2 ($D = 4$ inches and $EFL = 4$ inches) captures the slightly diverging beam from PM 1 and focuses it so that PM 3 ($D = 1.5$ inches and $EFL = 2$ inches) can collimate the beam to a size that fits the input port (1.5 inches diameter) of the FTIR. All three PMs are in one optical plane. Their relative positions are labeled in Fig. 4.1.

In the FTIR, the signal is converted to an interferogram via a Michelson interferometer. To have a broad spectral range of detection ($1 - 10$ μm), an XT-KBr beamsplitter is used. The detector in The FTIR is a liquid nitrogen cooled mercury cadmium telluride (MCT) detector, ensuring high sensitivity to weak signals. Finally, the frequency-domain signal is generated through Fourier transformation of the time-domain interferogram.

4.2.3 Understanding the Measured Signal

To extract the emittance spectrum of the sample being measured, calibration and background correction have to be performed based on the understanding of the signal composition, which is schematically shown in Fig. 4.7.

To facilitate the discussion, some important parameters (temperature, emittance and surface area are) and their corresponding subjects are listed in Table 4.1.

Table 4.1.
Summary of important parameters and corresponding subjects in the direct thermal emittance measurement. Irrelevant terms are labeled as "-".

	Sample-under-test	**Reference**	**Heater**	**Environment**
Temperature	T_e	T_c	T_h	T_r
Emittance	$\epsilon(\lambda)$	$\epsilon_c(\lambda)$	-	-
Area	A_e	A_c	-	-

At temperature T_e, the sample with surface area of A_e and emittance $\epsilon(\lambda)$ radiates an emission spectrum:

$$P_e(\lambda, T_e) = \epsilon(\lambda) A_e I_{BB}(\lambda, T_e), \tag{4.1}$$

where $I_{BB}(\lambda, T)$ is the blackbody radiation spectrum at temperature T. In addition to the emission signal from the high-temperature sample, room-temperature (T_r) emis-

sion from the surrounding environment can be reflected by the sample and eventually be collected by the detector. Similarly, this component of signal can be calculated as:

$$P_{refl}(\lambda, T_r) = \rho(\lambda) A_e I_{BB}(\lambda, T_r), \tag{4.2}$$

where $\rho(\lambda)$ is the reflectance of the sample. Other background signals from inside the chamber, $B_{in}(\lambda, T_h)$, should be accounted for as well and it varies with the heating stage temperature T_h.

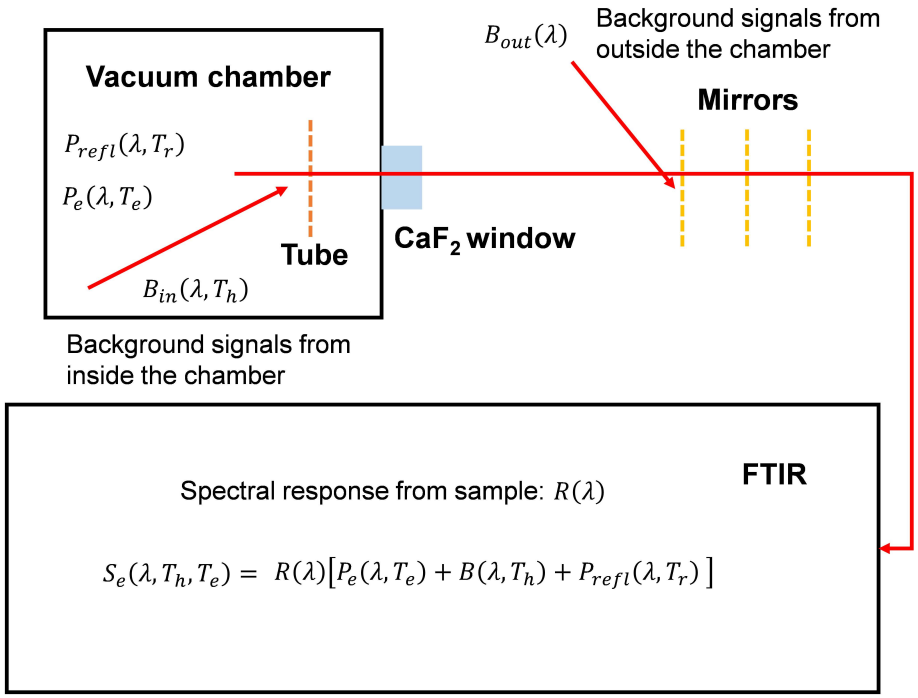

Fig. 4.7. Propagation of signal through the system. Key optical components are shown abstractly. Different sources of background noises are separated as noises from inside the chamber (dependent of the heating stage temperature) and noises from outside the chamber (independent of the heating stage temperature).

In our setup, a copper tube collects the signal with all three components included and sends it through a CaF_2 window. Outside the vacuum chamber, background

noise from other sources $B_{out}(\lambda)$ may enter the beam path and be detected by the FTIR. Therefore, there are in total 4 components included in the signal. As shown in Fig. 4.7, the total signal detected S_e can be expressed as:

$$S_e(\lambda, T_h, T_e) = R(\lambda)[P_e(\lambda, T_e) + B(\lambda, T_h) + P_{refl}(\lambda, T_r)], \tag{4.3}$$

$$B(\lambda, T_h) = B_{in}(\lambda, T_h)\frac{R_{in}(\lambda)}{R(\lambda)} + B_{out}(\lambda)\frac{R_{out}(\lambda)}{R(\lambda)}, \tag{4.4}$$

where $R(\lambda)$ is the spectral response (view factor included) of the optical system (all optical components included) for $P_e(\lambda, T_e)$ and $P_{refl}(\lambda, T_r)$; $R_{in}(\lambda)$ is the spectral response for $B_{in}(\lambda, T_h)$; $R_{out}(\lambda)$ is the spectral response for $B_{out}(\lambda)$.

From the discussion above, in order to extract $\epsilon(\lambda)$, the spectral response $R(\lambda)$ should be calibrated, and the background noise ($P_{refl}(\lambda, T_r)$ and $B(\lambda, T_h)$) should be identified.

4.3 Direct Thermal Emittance Measurement

In this section, a consistent measurement procedure that calibrates the direct thermal emittance measurement, and corrects background noise is developed. Details of the calibration and background correction is explained mathematically, followed by steps of measurements and validation.

4.3.1 Calibration and Background Correction

Assuming the sample being measured is opaque ($\rho(\lambda) = 1 - \epsilon(\lambda)$), Eq. 4.3 can be expressed explicitly (using Eq. 4.1 and Eq. 4.2) as [177]:

$$\begin{aligned} &S_e(\lambda, T_h, T_e) \\ &\quad = R(\lambda)\{\epsilon(\lambda)A_e\left[I_{BB}(\lambda, T_e) - I_{BB}(\lambda, T_r)\right] + B(\lambda, T_h) + A_e I_{BB}(\lambda, T_r)\}, \end{aligned} \tag{4.5}$$

The term $P_{refl}(\lambda, T_r)$, as a part of the background noise, is therefore no longer unknown. If the sample being measured is blocked by a low-temperature cap with near-zero thermal emittance (a silver evaporated cap in our setup), a background signal $S_b(\lambda, T_h)$ with the following expression will be measured:

$$S_b(\lambda, T_h) = R(\lambda)[B(\lambda, T_h) + A_0 I_{BB}(\lambda, T_r)], \tag{4.6}$$

where A_0 is the area of the silver evaporated cap. In our setup, A_0 is made to be very close to A_e to minimize the error.

The background noise $B(\lambda, T_h)$ can be canceled out by subtracting Eq. 4.6 from Eq. 4.5:

$$\begin{aligned} &S_e(\lambda, T_h, T_e) - S_b(\lambda, T_h) \\ &\quad = R(\lambda)\{\epsilon(\lambda) A_e [I_{BB}(\lambda, T_e) - I_{BB}(\lambda, T_r)] - \Delta A_e I_{BB}(\lambda, T_r)\}, \end{aligned} \tag{4.7}$$

$$\Delta A_e = A_0 - A_e, \tag{4.8}$$

The only thing that is undetermined in Eq. 4.7, except for $\epsilon(\lambda)$, is the spectral response $R(\lambda)$. It can be calibrated by a reference sample with high emittance across a broad spectral range. In our setup, a multi-wall carbon nanotube (MWCNT) sample grown on silicon (Si) substrate is used as the reference, due to its near blackbody property [66]. The room-temperature emittance of the MWCNT sample has a nearly uniform emittance of $\epsilon(\lambda) = \epsilon_c = 0.95$, consistent with previously reported performance [66].

Similar to Eq. 4.7, the signal from the reference sample at temperature T_c, after the subtraction of background noise, can be expressed as:

$$\begin{aligned} &S_c(\lambda, T_h', T_c) - S_b(\lambda, T_h') \\ &\quad = R(\lambda)\{\epsilon_c(\lambda) A_c [I_{BB}(\lambda, T_c) - I_{BB}(\lambda, T_r)] - \Delta A_c I_{BB}(\lambda, T_r)\}, \end{aligned} \tag{4.9}$$

$$\Delta A_c = A_0 - A_c, \tag{4.10}$$

where A_c is the area of the MWCNT reference; T_h' is the heating stage temperature, which is in general different from T_h. It should be noted that the temperature of the

reference sample T_c does not have to be the same as T_e. The measurement is thus greatly simplified.

Based on Eq. 4.7 and Eq. 4.9, the emittance spectrum of the sample being measured can be calculated as:

$$\epsilon(\lambda) = \Gamma \cdot \left\{ \frac{\epsilon_c(\lambda) A_c [I_{BB}(\lambda, T_c) - I_{BB}(\lambda, T_r)]}{A_e [I_{BB}(\lambda, T_e) - I_{BB}(\lambda, T_r)]} \right\} - \left\{ \frac{\Gamma \Delta A_c I_{BB}(\lambda, T_r) - \Delta A_e I_{BB}(\lambda, T_r)}{A_e [I_{BB}(\lambda, T_e) - I_{BB}(\lambda, T_r)]} \right\}, \tag{4.11}$$

$$\Gamma = \frac{S_e(\lambda, T_h, T_e) - S_b(\lambda, T_h)}{S_c(\lambda, T_h', T_c) - S_b(\lambda, T_h')}, \tag{4.12}$$

Apparently, the emittance $\epsilon(\lambda)$ can be determined once all four terms in Γ are measured. The four terms can be measured in three steps, which are discussed in Section 4.3.2.

4.3.2 Measurement Procedure

(1) **Reference measurement**: A MWCNT sample is used as a near-blackbody reference. The reference sample is heated up to a temperature T_c. The signal taken is $S_c(\lambda, T_h', T_c)$, where T_h' is the heating stage temperature during the measurement.

(2) **Sample emitter measurement**: The sample to be tested is heated to the target operating temperature (T_e) for emission spectrum measurement. The signal taken is $S_e(\lambda, T_h, T_e)$, where T_h is the heating stage temperature during the measurement.

(3) **Background measurement**: A cap that has a silver pad with dimensions around 10 mm $\times$ 10 mm is mounted to block the sample to be tested. Background spectra $S_b(\lambda, T_h)$ and $S_b(\lambda, T_h')$ are measured at heating stage temperatures that match with the reference and sample emitters measurements, respectively. The temperature of the cap is monitored by the type-K TC.

4.3.3 Validation of the Measurement Procedure

The measurement procedure developed above can be validated via a self-consistency test. For the purpose of validation, the reference sample (MWCNT) is heated up to three different temperatures (412 °C, 472 °C, 527 °C). The signal measured at the highest temperature is used as the reference, while the other two signals are used to extract the emittance spectrum of the MWCNT sample following the developed procedure. The assumption is that the emittance of the MWCNT sample changes little at different temperatures. The room-temperature emittance is $\epsilon_c = 0.95$, as mentioned in the prior section.

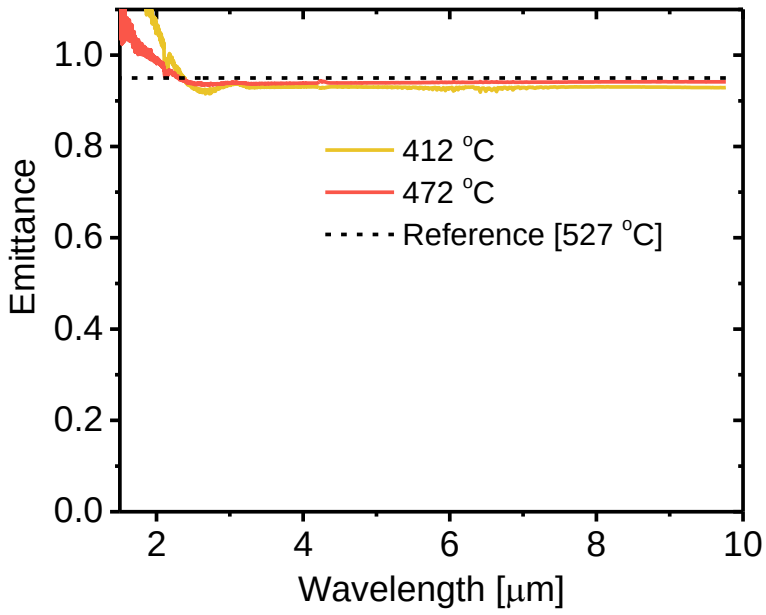

Fig. 4.8. Reliability of the measurement. The emittance of MWCNT is measured at different temperatures (412 °C, 472 °C). The same sample at 527 °C is used as the reference. It should be noted that the emittance greater than 1 is unphysical. For 472 °C, the emittance of the reference can be reproduced in the range of $2 - 10$ μm, proving the self-consistency of the direct thermal emittance measurement.

As shown in Fig. 4.8, both signals collected at 412 °C and 472 °C give consistent results in the spectral range of $3-10$ μm. For the signal collected at 412 °C, deviation starts to occur below 3 μm. The deviation continues to grow at short wavelengths, and the emittance even surpasses 1, which is unphysical. However, when the temperature is higher (472 °C), deviation only occurs below 2 μm. Such behavior indicates that the deviation is mainly caused by the low signal-to-noise ratio at short wavelengths.

The validation test shows that the developed measurement procedure is reliable in a spectral range of $2-10$ μm for sample temperatures higher than 472 °C. Of course, the spectral range can be further extended for higher temperature measurements.

4.4 An Example Measurement

The developed direct thermal emittance measurement setup can be utilized to characterize a broad range of solid-state, non-transparent samples. As an example, a silver(Ag) - TiN hybrid plasmonic metamaterial consisting of tilted Ag nanopillars and TiN binder is measured at elevated temperatures [178]. As shown in the inset of Fig. 4.9, Ag nanopillars in TiN binder are nearly aligned to a fixed tilted angle of about 50° from the normal. TiN, as a refractory material, should strongly suppresses the diffusion and chemical reaction of Ag in principle. Therefore, the hybrid plasmonic metamaterial is expected to be optically stable at high temperatures. In mid-IR spectral range, the best way of proving high-temperature stability is through direct thermal emittance measurements at possible operating temperatures.

Following the measurement procedure developed above, high-temperature emittance spectra are measured at three temperatures (T_e = 432 °C, 471 °C and 519 °C), as shown in Fig. 4.9. The measured emittance spectra are flat across a broad spectral range, which is consistent with its room-temperature characteristics measured by ellipsometry and FTIR [178]. In the temperature range measured, only slight variations ($\sim$ 1% absolute) with temperature are observed, indicating that the optical performance of the Ag-TiN hybrid plasmonic metamaterial holds at high temperatures.

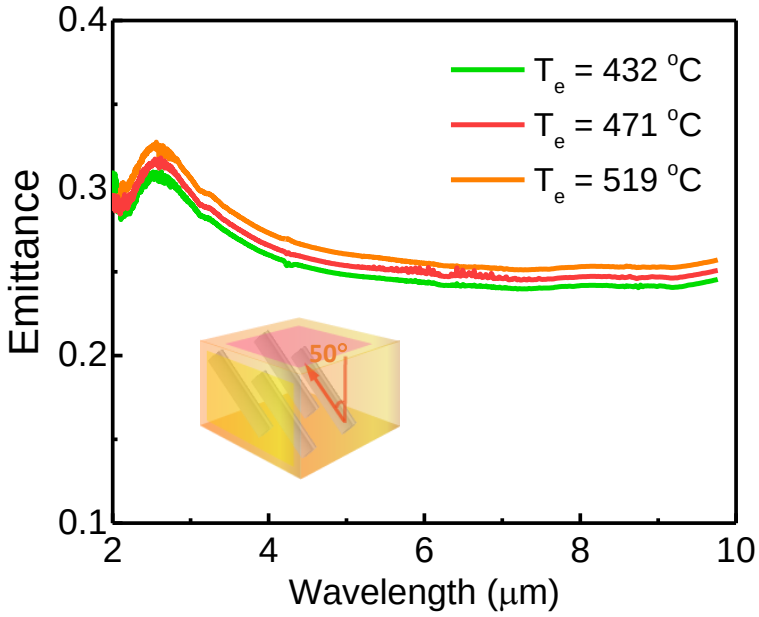

Fig. 4.9. An example measurement. The high-temperature emittance of a Ag-TiN hybrid plasmonic metamaterial (structure shown in the inset, arrays Ag nanopillars tilted at 50° in TiN binder.) is measured by the direct thermal emittance measurement. The measured emittance is consistent with the room-temperature characteristics reported in [178]. Only slight variation in emittance happens at high temperatures, proving the strong thermal stability of the measured sample.

In this example, direct thermal emittance measurement is used to characterize the high-temperature emittance of a non-trivial sample, a Ag-TiN hybrid plasmonic metamaterial. The measured results are consistent with room-temperature characterizations and proves the stability of the sample at high temperatures. Based on this example, the direct thermal emittance measurement is proved to be versatile for various types of opaque emitters.

4.5 Conclusions

In this work, a direct thermal emittance measurement setup is designed and built. Based on the understanding of the measurement, a consistent procedure of measurement is developed. The setup, along with its measurement procedure, is critical to the high-temperature characterization of spectrally-selective thermal emitters and solar absorbers. Its broadband measurement and wide temperature range offer great versatility to measure various types of samples under different conditions. In Chapter 5, the direct thermal emittance measurement setup is used to characterize a thin-film spectrally-selective solar absorber/emitter.

5. HIGH-TEMPERATURE, SPECTRALLY-SELECTIVE, SCALABLE, AND FLEXIBLE THIN-FILM SI ABSORBER AND EMITTER[1]

Solar thermal technologies have great potential to provide low-cost storage for solar energy. However, their efficiencies are limited by a lack of scalable, mechanically flexible, durable, yet highly-efficient spectrally-selective solar absorbers suitable for high temperatures at low solar concentrations. Here, we overcome these challenges by fabricating a scalable free-standing spectrally-selective thin-film Si absorber and emitter (SSTFS) composite. Its high-temperature emittance shows strong spectral selectivity, even at 595 °C. Thermal stability is proven by measuring optical properties before and after thermal cycling equivalent to one day of concentrated sunlight. Despite the use of crystalline Si, the fabricated SSTFS composite exhibits exceptional mechanical flexibility to cover most surface geometries. The SSTFS composite demonstrates the potential of high-temperature, efficient and flexible solar absorbers and thermal emitters to advance renewable solar energy with storage.

5.1 Introduction

Solar thermal technologies provide a promising complement to solar photovoltaics. Since they first capture sunlight as heat, and then convert it to electricity, they can readily incorporate low-cost storage for power generation at night. The efficiency of the first step depends on the specific application, but is limited by the optical properties of the solar absorber at high temperatures. These particularly include the solar absorptance of the absorber and its losses from thermal re-radiation. Both

[1]Adapted from: Z. Zhou, H. Tian, T. M. Hymel, H. Reddy, V. M. Shalaev, Y. Cui, and P. Bermel, "High Temperature, Spectrally-selective, Scalable, and Flexible Thin-film Si Absorber and Emitter," *Optical Materials Express*, (Under Review).

factors relate directly to the absorptance spectrum of the solar absorber over a broad spectral range. The thermal transfer efficiency η_t captures the trade-off between these two factors [170]. For a given solar concentration C and operating temperature T, η_t is given by:

$$\eta_t = \overline{\alpha} - \frac{\overline{\epsilon}\sigma T^4}{CI}, \tag{5.1}$$

where I is the solar irradiance (1 kW/m^2 is the solar constant); and $\overline{\alpha}$ and $\overline{\epsilon}$ are the spectrally-averaged solar absorptance and thermal emittance, respectively. Both can be calculated from the absorptance spectrum of the absorber [23, 170]. To maximize η_t, a spectrally-selective absorber is needed, with absorptance in the wavelength range $0.3 - 2.0$ μm close to unity, and emittance at longer wavelengths close to zero. High spectral selectivity is particularly critical for high operating temperatures and low solar concentrations, conditions that attract much attention due to the combination of higher Carnot efficiency and lower (or zero) cost for solar tracking. Prior work demonstrated that such spectral selectivity can be achieved by composite materials like cermets [48, 179, 180], where metallic nanoparticles are embedded in ceramic binders. Furthermore, multilayer structures [181], photonic crystals [11, 24, 57, 182] and plasmonic structures [18, 183, 184] can tailor the absorptance and emittance spectrum of bulk materials [20, 21], thereby giving rise to strong spectral selectivity. Recent reviews have shown that there are often significant trade-offs between performance, durability, and costs [23, 170].

To convert high-temperature solar heat into electricity, thermophotovoltaic (TPV) systems stand out among various technologies [9, 185]. due to high theoretical maximum efficiencies [186] as well as high power densities [79]. The value of thermophotovoltaics (TPV) also extends well beyond solar energy. It has also been proposed for applications such as recovering waste heat [14, 23] and power generation from fuels [79]. The energy conversion process in TPV consists of two steps. First, a thermal emitter converts heat into thermal radiation. Second, a photovoltaic (PV) diode con-

verts the incident radiation into electricity [23]. A good thermal emitter should have high emittance only over a certain bandwidth above the bandgap energy of the PV diode, and near-zero emittance elsewhere [11].

Complex nanophotonic structures similar to spectrally-selective absorbers may serve as highly selective emitters, since Kirchhoffs law of thermal radiation [67] predicts absorptivity equals emissivity at every wavelength in thermal equilibrium. For example, metamaterials have been demonstrated in prior work to serve as highly selective emitters [27, 187]. It is also crucial that the spectral selectivity holds even at elevated temperatures. In prior work, photonic crystal emitters on refractory metals (similar to photonic crystal absorbers) have been proposed [56] and demonstrated [33]. Plasmonic structures based on refractory materials like titanium nitride have also demonstrated significant spectral selectivity and excellent thermal stability [42].

While prior literature has primarily focused on measures such as thermal transfer efficiency, there are in fact three critical figures of merit for selective solar absorber materials relevant to real applications: scalable manufacturing, mechanical flexibility, and good high-temperature performance. Absorber/emitters that meet all three criteria have yet to be reported in the literature. Those with excellent spectral selectivity, such as nanophotonic structures, are difficult to scale up because of both fabrication methods and raw material costs. Their rigid substrates also limit mechanical flexibility, causing difficulties when applied to non-flat surfaces. Low-cost cermets are commercially available as an alternative, but have limited maximum temperatures and lifetimes. Extensive studies show that new, more expensive manufacturing techniques are required to realize improved performance [179].

To achieve a good balance of all three aforementioned figures of merit, we focus on improving a less-studied category known as the semiconductor-metal-dielectric trio. These composites can be as simple as a three-layer stack of anti-reflection coating (ARC), semiconductor absorber layer and metallic back reflector [170]. Low-cost, high-quality, earth-abundant semiconductor wafers are already commercially avail-

able from the microelectronics and photovoltaics industries. Semiconductor-metal tandems using silicon (Si) and germanium (Ge) have been theoretically proposed to be excellent selective solar absorbers [23, 188]. Furthermore, thick single-crystal Si absorbers with surface texturing [189] and Si_3N_4 ARC [53] have been experimentally demonstrated. However, high-temperature characterization measurements show that thermal emittance due to intrinsic carrier concentration can increase rapidly with temperature [53], limiting the use of thick Si absorbers at higher temperatures.

An effective way to suppress this effect is reducing the thickness of the semiconductor [53]. For instance, absorbers with reduced Si thickness have been fabricated by physical (PVD) or chemical vapor deposition (CVD) [50]; however, free-standing, single-crystal Si thin-films have not been used for such applications. Their theoretical advantages of low mid-IR emittance, good thermal stability and strong mechanical flexibility are outstanding. But fabricating single-crystal thin-film Si using conventional growth methods imposes significant challenges [190–192]. Fortunately, it has recently been demonstrated that direct wet etching of a commercial single-crystal wafer can provide free-standing thin films of high quality [193]. Following an improved, CMOS-compatible procedure, a free-standing single-crystal spectrally-selective thin-film Si absorber/emitter (SSTFS) composite material is fabricated here. It is a simple three-layer structure consisting only of commercially available materials, required for scalability. Its structure excludes any rigid substrate, allowing strong mechanical flexibility. Furthermore, high spectral selectivity has been experimentally proved in this work, matching closely with theory. The SSTFS is also proven to have good thermal stability, capable of withstanding high operating temperatures for many hours at a time. Our work shows that with optimization, SSTFS composites can have a good balance of scalable manufacturing, mechanical flexibility and good high-temperature spectral selectivity and durability.

5.2 Fabrication and High-temperature Characterization

The SSTFS studied in this work preserves some of the best features of the spectrally-selective wafer-based Si (SSWS) investigated in prior work [53]. There is generally a trade-off between suppressing emission ($\overline{\epsilon}$) and maintaining absorption ($\overline{\alpha}$), which varies with thickness. As a result, the optimal thickness of Si is around 10 μm [53].

5.2.1 Fabrication

The fabrication of SSTFS consists of three steps: (1) etching commercial Si wafer to target thickness; (2) Deposition of Ag back reflector; (3) Deposition of Si_3N_4 ARC. Starting from step (1), lightly doped ($1-10\,\Omega\,\mathrm{cm}$) double-side-polished n-type (100) wafers are first masked with a PECVD-deposited 500 nm silicon nitride (SiN_x) layer around the edges, creating a thick handling ring for future ease of handling. The wafers are then loaded into a cassette and dipped into 2% hydrofluoric acid (HF) to etch the native oxide before the Si etching bath. After a DI water rinse, the wafer cassette is placed into a 25% tetramethylammonium hydroxide (TMAH) solution held at 90 °C for the duration of the etch. Once the wafers are etched to the desired thickness, they are removed from the TMAH etch bath, rinsed with DI water, and blown dry with nitrogen gas. For step (2), a 300 nm silver layer is deposited on the backside of the thin-film by e-beam evaporator (CHA) at a rate of 1.5 Å/s. Finally, in step (3), a 92 nm silicon nitride (Si_3N_4) ARC is sputtered at the front side using a magnetron sputtering system (custom-built by PVD Products) using a 100 W AC power supply and 5 mTorr with 15 sccm Ar. The fabrication process flow is graphically shown in Fig. 5.1.

The cross-section of the fabricated SSTFS is shown schematically in Fig. 5.2 (a). The dimension of each layer is extracted by fitting the room-temperature emittance spectrum with numerical simulations. As shown in Fig. 5.2 (d), the blue curve is the emittance spectrum of our non-transparent sample characterized by reflectance (diffuse + specular) measurement, following Kirchhoffs law (emittance = 1 - reflectance),

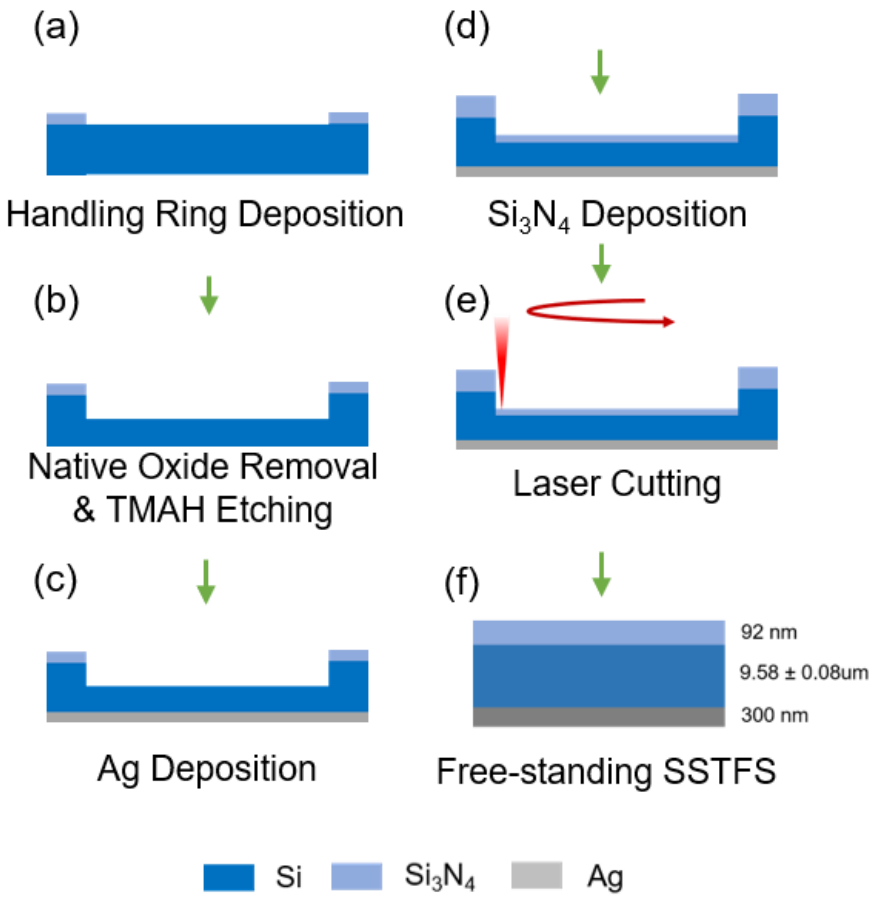

Fig. 5.1. Fabrication process flow of SSTFS. (a) SiN_x handling ring PECVD deposition. (b) Thin-film wafer fabricated by TMAH wet etching. (c) Ag back reflector deposition by e-beam evaporation. (d) Si_3N_4 deposition by sputtering. (e) Handling ring removal by laser cutting. (f) The fabricated free-standing SSTFS composite material.

using a Perkin Elmer Lambda 950 spectrophotometer with an integrating sphere. The spectral range is 300 - 2500 nm with a resolution of 5 nm. The spot size of the incident beam is about $0.5 \times 1.0 cm^2$. The theoretical room-temperature emittance (orange curve) is simulated using S4 [171], and the materials are modelled as in Tian *et al.* [53].

Fig. 5.2 (b) shows the as-fabricated SSTFS. Much like a Si thin film fabricated via KOH etching [193], it can be easily cleaved into smaller pieces to tile surfaces.

As shown in Fig. 5.2 (c), the free-standing SSTFS is quite mechanically flexible - for instance, it conforms to an acrylic rod with 1.27 cm diameter without breaking.

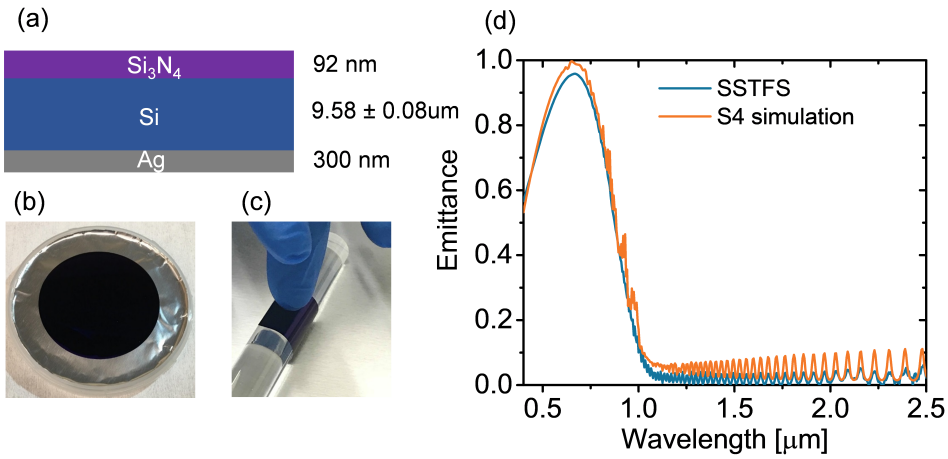

Fig. 5.2. (a) Cross-sectional schematic of the SSTFS. The thickness of Si_3N_4 and Si are determined by fitting the room-temperature emittance spectrum with a simulation in S4. (b) As-prepared SSTFS sample in a 10 cm wafer carrier. (c) The sample is mechanically flexible enough to wrap around a 1.27 cm diameter acrylic rod. (d) The measured room-temperature emittance spectrum matches simulations closely.

5.2.2 High-temperature Thermal Emittance Measurements

Since the optical properties of most selective absorbers/emitters are temperature dependent, high-temperature optical characterization is essential to the proper study of SSTFS. To cover the broad spectral range from visible to mid-IR, two characterization techniques are used. For wavelengths from 0.3 to 2.0 μm, the *in situ* high-temperature emittance is measured using a custom-built high-temperature ellipsometer [194, 195] [see Fig. 5.3]. To capture the high-temperature emittance from 2 to 10 μm, a custom-built direct thermal emittance measurement setup is used [53] [see Fig. 4.1 in Chapter 4].

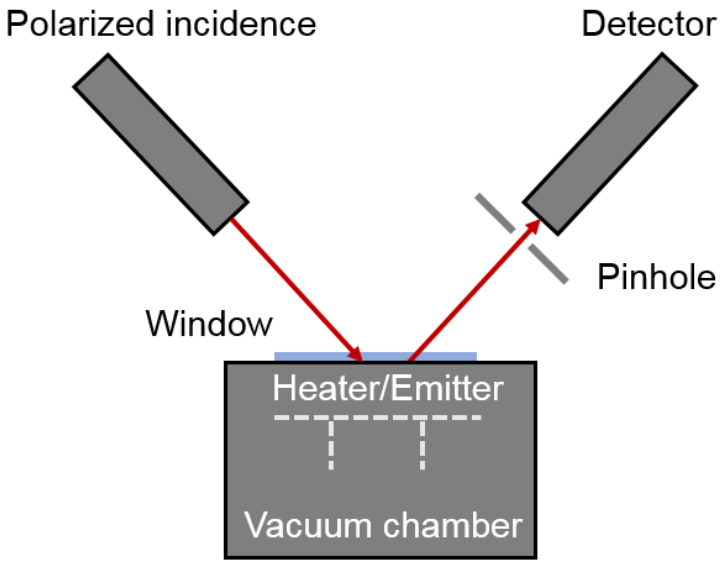

Fig. 5.3. A customized high-temperature variable angle spectroscopic ellipsometer covering wavelengths from 0.3 to 2.0 μm. Samples are heated in a vacuum chamber. Temperature dependent specular reflectance spectra of s- and p-polarizations are measured through a quartz window at 18° angle of incidence. The pinhole blocks most of the background thermal radiation.

The experimental setup of the high-temperature ellipsometer is schematically illustrated in Fig. 5.3. The heating stage is integrated onto a variable angle spectroscopic ellipsometer (J.A. Woollam V-VASE UV-VIS-NIR). A quartz window on the vacuum (10^{-6} Torr) heating stage (Linkam TS1500V) provides optical access to the sample and a pinhole is placed in the reflected beam path to reduce the background thermal emission reaching the detector. Emittance is inferred as $1 - (R_s + R_p)/2$, where R_s and R_p are reflectance of s- and p- polarizations measured at an incident angle of 18°, respectively. The wavelength range of the high-temperature ellipsometry measure-

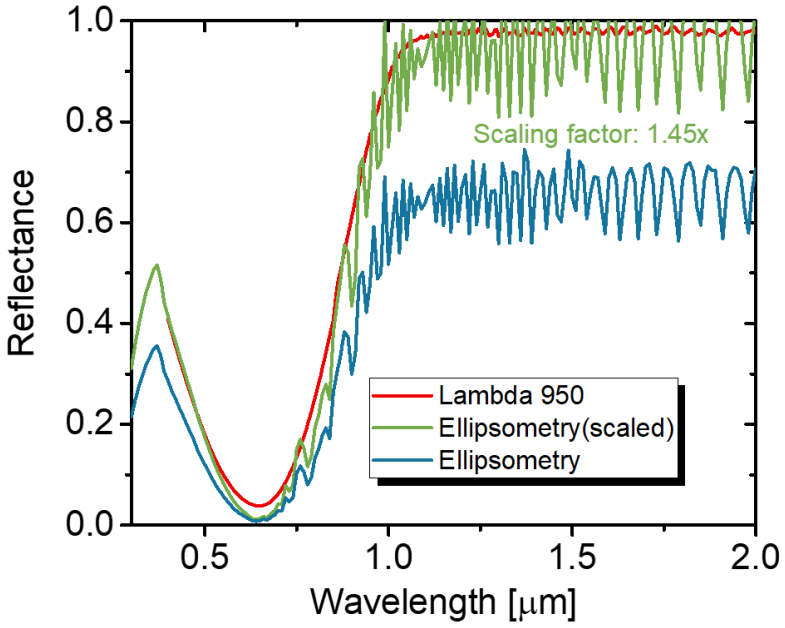

Fig. 5.4. Reflectance spectrum measurement using an ellipsometer, showing the procedure for calibrating the scaling factor. The ellipsometric spectrum measured with quartz window and pinhole installed (blue curve) is re-calibrated to the green curve, to match with the independent specular + diffuse reflectance (red curve) measurement by a Perkin Elmer Lambda 950 spectrophotometer (with an integrating sphere attachment). The scaling factor in this work of 1.45 provides a good match, such that reflectance does not exceed 100%.

ments is $0.3 - 2.0$ μm with 10 nm wavelength steps. Calibration of this method is performed with a reference sample at room temperature. The presence of the window and the pinhole introduces a scaling factor into the calibration. This scaling factor is first calibrated at room-temperature, as shown in Fig. 3, and is used to correct all subsequent high-temperature measurements. The high-temperature spectra are smoothed by a 5 adjacent point moving average to clearly depict the data.

The direct thermal emittance measurement is performed on the setup introduced in Chapter 4. For good thermal contact with the heater, the thin-film samples are

attached to graphite foil using high-temperature silver paste (597-A, Aremco). To measure such a broad band spectrum, a low mirror velocity of 0.1581 $\mathrm{cm} \cdot \mathrm{s}^{-1}$ is set. Each spectrum is averaged over 100 scans for acceptable signal to noise ratio. The thermal cycle is performed using the same setup without optical measurements.

5.2.3 Simulation of High-temperature Emittance

The theoretical high-temperature emittance spectra in the range of $0.4 - 10$ μm are simulated using S4 [171]. For high-temperature simulations, the complex refractive index of Si_3N_4 is extracted from the work by Kischkat *et al.* [196]. Temperature-dependent dielectric constant of Ag is calculated using the Drude-Lorentz parameters derived by Reddy *et al.* [195]. For Si, a semi-empirical model [197][39] is used to calculate high-temperature refractive index. To match different experimental conditions of the two measurement techniques, emittance simulations are performed at 18° in $0.4-2$ μm (for ellipsometry setup), and angular-averaged from 0 to 32° in $2,0-10$ μm (for direct thermal emittance measurement setup).The angular-averaged spectra in $2.0 - 10$ μm are given by $\int_0^{\theta_0} \mathrm{d}\theta \epsilon(\lambda,\theta)\cos(\theta)\sin(\theta) / \int_0^{\theta_0} \mathrm{d}\theta \cos(\theta)\sin(\theta)$, where $\epsilon(\lambda,\theta)$ is the emittance at wavelength λ and angle θ; $\theta_0 = 32°$. In Fig. 5.5(a) - (b), both spectra are separated into two regions (shaded red and unshaded), reflecting different characterization techniques.

5.3 Results

The high-temperature emittance spectra measured at two temperatures using the aforementioned techniques are plotted in Fig. 5.5 (a) - (b). High-temperature simulations are shown for comparison (gray curves). As discussed in Section 2.3, the differences between the two characterization techniques affects our interpretation, giving rise to a jump as we transition between the two techniques at 2.0 μm. For both temperatures (505 °C and 595 °C), the experimental data matches well with our simulations. An increase in the mid-IR emittance is observed as temperature rises,

induced by higher intrinsic carrier concentrations. In Fig. 5.5 (b), the emittance spectrum of an SSWS measured at 535 °C [53] is plotted (green curve) for comparison. Significant suppression of mid-IR emittance is achieved, which would lead to less re-radiation loss for solar thermal applications and less sub-bandgap emission loss in TPV applications, compared to its wafer-based counterpart.

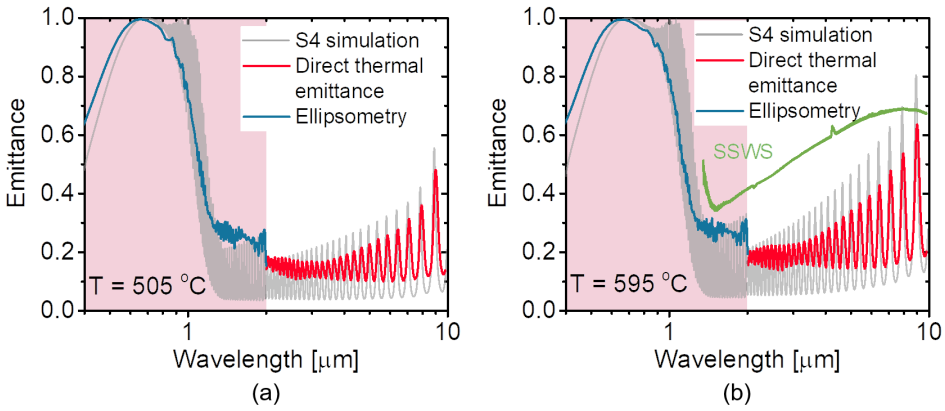

Fig. 5.5. High-temperature T emittance spectra for SSTFS: (a) T = 505 °C, (b) T = 595 °C. The high-temperature ellipsometry data (blue curves) and direct thermal emittance measurement data (red curves) are plotted together with numerical simulation results (gray curves) for comparison. Overall, a good match is observed. The high-temperature emittance of an SSWS measured at 535 °C [53] is also plotted in (b) (green curve). The reduced Si thickness suppresses $\bar{\epsilon}$ from 0.60 to 0.23, even though the temperature is 60 °C higher.

For solar thermal applications, the measured emittance of SSTFS gives $\overline{\alpha} = 0.76$ and $\bar{\epsilon} = 0.23$ at 595 °C. The thermal transfer efficiency η_t, following Eq. 5.1, is 0.61 under 50 suns. However, the SSWS, even at a lower temperature (535 °C), has $\bar{\epsilon} = 0.60$ over the spectral range of the green curve in Fig. 5.5 (b). As expected, reduced Si thickness strongly suppresses thermal re-radiation. Compared with other state-of-the-art selective absorbers reviewed in [179], the SSTFS shows strong suppression of thermal emittance at the operating temperature. Since emittance increases

with temperature, this compares favorably with values summarized in [179], which were mostly measured at low temperature or extrapolated from room temperature. Furthermore, although the solar absorptance of SSTFS is slightly lower than those listed in [179], a near 15% relative improvement can be achieved without sacrificing the structural simplicity using a multi-layer ARC [23]. Importantly, all of the absorbers listed in [179] have substrates, which limit their mechanical flexibility. In contrast, the SSTFS demonstrated in our work is a free-standing thin-film that can conformally cover curved surfaces. Such unique property, combined with its good optical performance at high-temperature, makes our SSTFS more adaptable to real applications.

The SSTFS also shows major advantages as a selective thermal emitter for TPV applications. First, its strong spectral selectivity at high temperatures is desirable for high system efficiencies. One way to quantify this is calculating the spectral averaged emittance for above-bandgap spectrum $\overline{\epsilon}_{above}$ and below-bandgap spectrum $\overline{\epsilon}_{below}$ as:

$$\overline{\epsilon}_{above} = \frac{\int_{0.3}^{\lambda_g} d\lambda \epsilon(\lambda) I_{BB}(\lambda, T)}{\int_{0.3}^{\lambda_g} d\lambda I_{BB}(\lambda, T)}, \tag{5.2}$$

$$\overline{\epsilon}_{below} = \frac{\int_{\lambda_g}^{10} d\lambda \epsilon(\lambda) I_{BB}(\lambda, T)}{\int_{\lambda_g}^{10} d\lambda I_{BB}(\lambda, T)}, \tag{5.3}$$

where λ_g is the wavelength [μm] corresponding to the bandgap of PV diode; $I_{BB}(\lambda, T)$ is the Plancks blackbody radiation function at wavelength λ [μm] and temperature T. Assuming a TPV system with the bandgap of PV diode at 1.1 eV, such as c-Si PV, the above-bandgap spectrally-average emittance $\overline{\epsilon}_{above} = 0.68$ while the sub-bandgap spectrally-average emittance $\overline{\epsilon}_{below} = 0.23$ at a temperature of 595 °C. Second, the low sub-bandgap emittance may reduce PV diode heating, helping to maintain high TPV efficiencies [198]. In real TPV applications, the two factors discussed above depend not only on the thermal emitter, but also on the PV diode and other system parameters. Therefore, a system-level comparison must be performed.

5.4 Discussion

The improvement in spectral selectivity, as demonstrated above, can greatly enhance the performance of semiconductor-metal-dielectric trio in high-temperature applications. To illustrate such enhancement, we compare the performance of an SSTFS with an SSWS [53] in solar thermal and TPV applications. The strong agreement between measured high-temperature emittance and theory indicates our model may be safely interpolated to intermediate temperatures where characterization has not yet been performed. For fair comparison, the thickness of Si_3N_4 in both structures is set to 92 nm, consistent with the fabricated SSTFS. Per Tian *et al.* [53], such thickness of Si_3N_4 is very close to its optimal value.

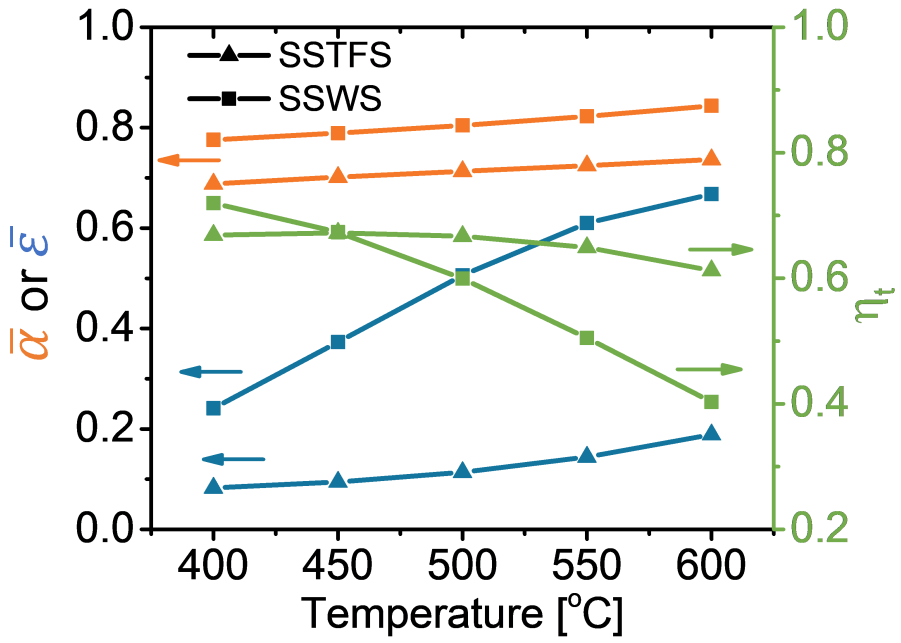

Fig. 5.6. Selective solar absorbers. The (orange curves) and (blue curves) are simulated at different operating temperatures for SSTFS (triangle symbol) and SSWS (square symbol), respectively. The thermal transfer efficiencies (green curves) are calculated assuming 50 sun concentration. SSTFS outperform SSWS at temperatures $> 450\,°C$.

5.4.1 Selective Solar Absorber

Fig. 5.6 shows the $\overline{\alpha}$ (orange curves), $\overline{\epsilon}$ (blue curves) and η_t (green curves) of the SSTFS (triangle symbol) and SSWS (square symbol) as solar absorbers at various SSWS, since Si has an indirect bandgap. However, the $\overline{\epsilon}$ of the SSWS increases rapidly with temperature, while the $\overline{\epsilon}$ of the SSTFS remains low. As a result, the η_t of SSTFS is higher once the temperature passes 450 °C. The improvement in η_t is most pronounced at higher temperatures, corresponding to a 52% relative increase around 600 °C.

5.4.2 Selective TPV Emitter

Another important application is the selective emitter for a TPV system. As mentioned above, reduced spectral selectivity of emitters not only increases losses from sub-bandgap emission, but also decreases PV diode efficiencies through heating. Both factors significantly impact the conversion efficiency. Fig. 5.7 compares the efficiencies of two TPV systems with different selective emitters: an SSTFS and an SSWS. The relative increase in TPV efficiency, given by $RI_{tpv} = (\eta_{tpv-t} - \eta_{tpv-w})/\eta_{tpv-w}$, is calculated for various PV bandgaps and emitter temperatures, where η_{tpv-t} and η_{tpv-w} are the TPV efficiencies for SSTFS and SSWS, respectively. The TPV performance is estimated at various emitter temperatures ($400 - 600$ °C) and PV bandgaps (0.5 - 1.2 eV). For PV diodes at different bandgaps, an external quantum efficiency (EQE) of 0.9 and ideality factor of 1 are assumed. Dark current density at room temperature is calculated by a realistic model that reflects the state-of-the-art PV performances [199]. The view factor F from emitter to PV diode is assumed to be 0.99.

For Fig. 5.7 (a), a more realistic TPV model is used, which incorporates PV diode heating from unused radiation in a self-consistent manner. The temperature of PV diode is determined by solving the power balance equation: $F \cdot P_{emit} = P_{ele}(T_{PV}) + P_{dis}(T_{PV}) + P_{rad}(T_{PV})$, where P_{emit} is the total emitted power from the emitter; $P_{ele}(T_{PV})$ is the electrical power output from PV diodes at temperature T_{PV};

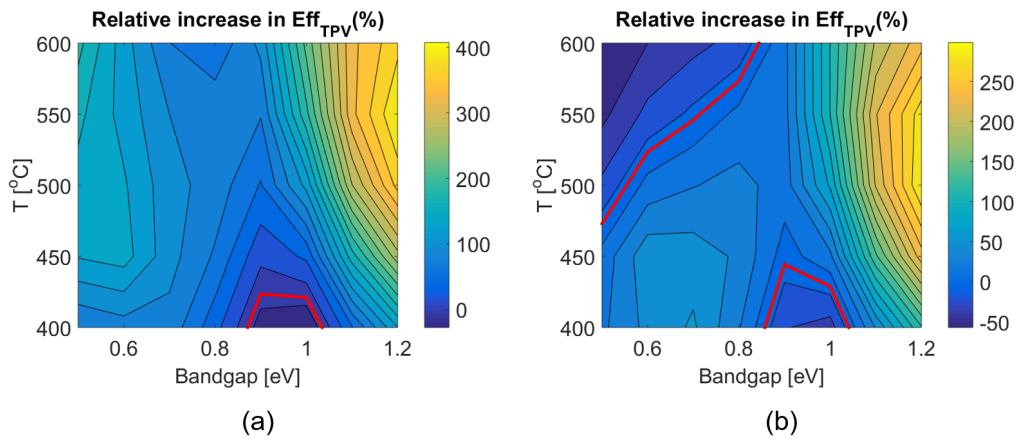

Fig. 5.7. Selective TPV emitters. The relative increase of TPV efficiency (RI_{tpv}) when the SSWS is replaced by the SSTFS, is calculated for different PV bandgaps and emitter temperatures. (a) Parasitic heating of PV diode is considered. (b) The PV diode temperature is assumed to be 300 K. Except for the area enclosed by the red curve, where RI_{tpv} is negative, reduced sub-bandgap emission and PV diode heating significantly improves TPV efficiencies.

$P_{dis}(T_{PV})$ and $P_{rad}(T_{PV})$ are the heat dissipation of PV diodes through non-radiative heat transfer and radiative heat transfer, respectively. An effective cooling coefficient of 20 $\mathrm{mW \cdot K^{-1}}$ is assumed so that the maximum PV temperature is below 200 °C. The PV diodes are assumed to have 100% absorption across the spectral range considered to take into account the fact that most PV diodes have sub-bandgap absorption.

Fig. 5.7 (a) indicates that the SSTFS is superior to the SSWS for most PV bandgaps and emitter temperatures considered, except for the area below the red curve, where RI_{tpv} is negative. Although the absolute TPV efficiency is limited by the operating temperature, the relative increase in efficiency is significant, especially for high emitter temperatures and large bandgap PV diodes (> 1 eV). For example, when a c-Si PV diode with bandgap of 1.1 eV is used and the emitter is at a temperature of 600 °C, RI_{tpv} is as high as 340%. This can be explained by the fact that SSTFSs are more selective than SSWSs at elevated temperatures, suppressing both

the sub-bandgap emission loss and parasitic heating of the PV diode. Even when the PV diode temperature is well-controlled at 300 K, as shown in Fig. 5.7 (b), RI_{tpv} can still reach 200%.

5.5 Thermal Stability

In practical solar thermal and TPV applications, the absorber and the emitter must withstand high-temperature operation at least several hours a day. Typically, the highest concentrations of sunlight are available around 6 hours (hr) per day under clear skies [200]. Therefore, it is important to investigate the thermal stability of SSTFS at such time scales. In this work, an SSTFS is heated up to 600 °C under ultra-high vacuum ($\sim 10^{-7}$ Torr) for two thermal cycles. The first cycle (thermal cycle #1) dwells at the maximum temperature for 1 hr; the second (thermal cycle #2), for 5 hr more. The temperature profile of thermal cycles is shown in Fig. 5.8.

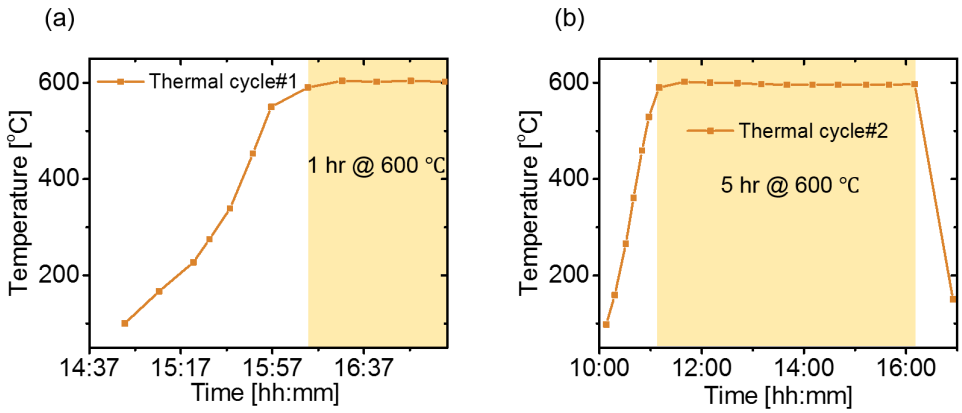

Fig. 5.8. Full temperature profiles of the two thermal cycles used for the thermal stability tests. (a) The first cycle (thermal cycle #1) dwells at 600 °C for 1 hr and (b) the second cycle (thermal cycle #2) dwells at 600 °C for 5 hr. Both cycles are performed on the same sample under ultra-high vacuum ($\sim 10^{-7}$ Torr). The temperature is measured by a type-K thermocouple attached to the sample by silver paste (597-A, Aremco). The same sample remains at 600 °C for 6 hr in total.

After each thermal cycle, a room-temperature emittance spectrum is measured. Fig. 5.9 compares the emittance before and after each thermal cycle. The interference fringe amplitude is smaller than the high-temperature results, due to much weaker absorption in Si and the larger size of the incident beam used in room-temperature reflectance measurements. A slight degradation in IR reflection occurs after thermal cycle #1, while the emittance peak stays nearly intact. After thermal cycle #2, the degradation slows down significantly even with a 5x longer dwell time. The overall spectral selectivity is maintained after 6 hr total annealing.

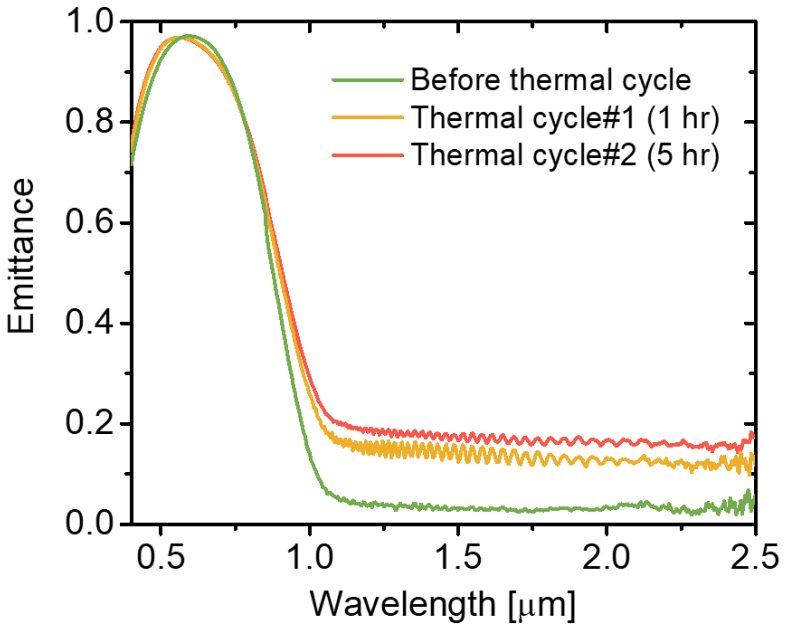

Fig. 5.9. Thermal stability test. Room-temperature emittance spectra of SSTFS are measured before thermal cycle (green curve), after the first thermal cycle that dwells at 600 °C for 1 hr (yellow curve) and after the second thermal cycle that dwells at 600 °C for 5 hr (red curve). Slight elevation in emittance is observed and is mainly caused by the degradation of the Ag back reflector.

To test the lifetime of the SSTFS, 4 consecutive 6-hr thermal cycles are performed on a pristine sample. Maximum temperature for each thermal cycle is still 600 °C.

Room temperature emittance spectra are measured at various spots on the sample surface after the fourth thermal cycle. As shown in Fig. 5.10, more significant degradation is observed. It should be noted as well that the extent of degradation

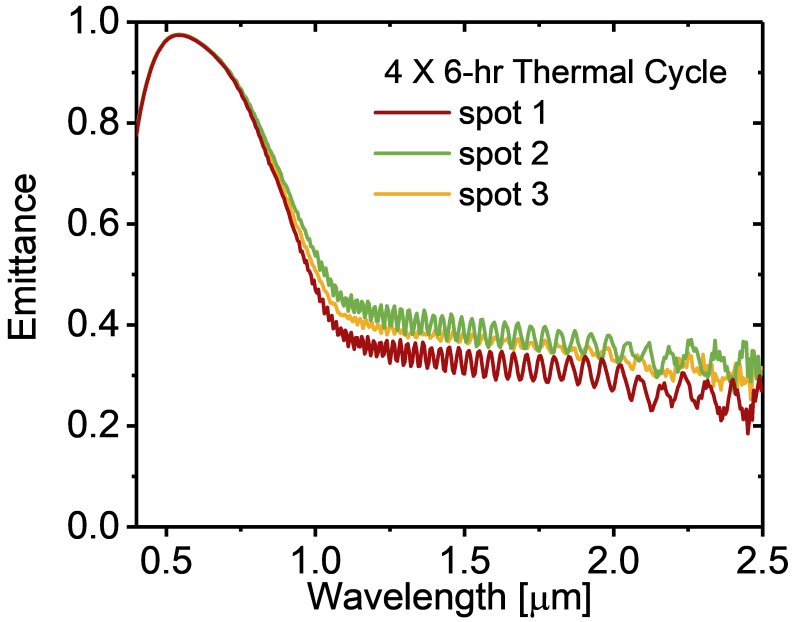

Fig. 5.10. 24 hr Thermal stability test. Room-temperature emittance spectra of SSTFS are measured after the 4th 6-hr thermal cycle that dwells at 600 °C. More significant elevation in emittance is observed and the degradation varies with location.

varies with the location, indicating non-uniform delamination in the structure. To further explore the root cause, Scanning Electron Microscope (SEM) images are taken from the back side of the SSTFS. As shown in Fig. 5.11, discontinuity in the Ag layer is apparent. As we zoom in the view (Fig. 5.11 (a) - (d)), traces of Ag dewetting the Si surface, a well-known effect [195], can be found. Given that most of the degradation happens at energies below the Si bandgap, and that the thin-film Si is stable even at 900 °C for 4 hr, we conclude that the dominant mechanism is the degradation of the Ag back reflector and/or the Si/Ag interface. Therefore, further improvement in

thermal stability lies in replacing Ag with a refractory back reflector. Nonetheless, the SSTFS shows great thermal stability at 600 °C over a 6 hr period of time, closely resembling a real (outdoor) application.

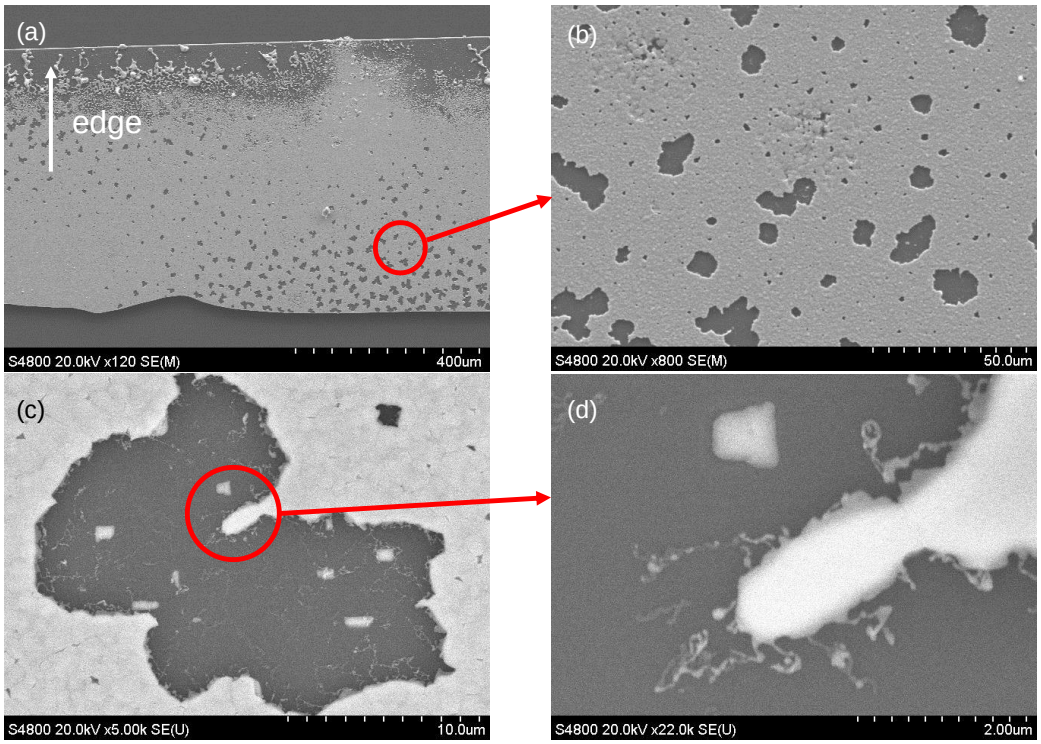

Fig. 5.11. SEM images of the back side of SSTFS after 24 hr Thermal stability test. (b) Corresponds to the circled area in (a). (c) same image, zoomed in further, and (d) corresponds to the circled area in (c). Apparent dewetting effect of Ag from Si surface is observed.

5.6 Conclusions

In summary, we have fabricated a free-standing, high temperature, spectrally-selective thin-film Si absorber/emitter (SSTFS) composite that exhibits a good balance of all three figures of merit for new solar thermal or TPV applications. Its standardized CMOS-compatible fabrication processes make it possible for scalable manufacturing. Its tremendous mechanical flexibility allows it to be adapted to a wide

range of applications. High-temperature emittance characterization has been performed, and shows an excellent match with the corresponding numerical simulations. Compared with its wafer-based counterpart, the thin film design strongly suppresses thermal emittance in the mid-IR, resulting in a stronger spectral selectivity and superior performance across a broad range of operating conditions for solar thermal and TPV. Furthermore, its thermal stability is demonstrated in multiple long-term thermal cycles, corresponding to prospective use cases. The presented selective absorber/emitter design strategy is certainly not restricted to Si, Ag and Si_3N_4. Further improvements are possible for SSTFS composites. For example, a multi-layer ARC may improve the solar absorptance. Direct-bandgap semiconductors may replace Si and effectively suppress free-carrier absorption without sacrificing above-bandgap absorption. Also, thermal stability / lifetime may be further enhanced by replacing Ag with refractory metals in future work. Other thin-film fabrication technologies, such as anisotropic wet etching of a Si boule, epitaxial lift-off, or high-throughput techniques like solution processing/ roll-to-roll printing, may further reduce the combined material and fabrication costs. Most importantly, this work paves the way for large-scale development and deployment of efficient, low-cost, and flexible selective solar thermal absorbers/emitters, which might be particularly beneficial for producing high-temperature steam in low concentrating selective absorbers, as well as opening up new possibilities for future solar and thermal technologies.

RADIATIVE THERMAL MANAGEMENT ON TPV

Chapter 6 and Chapter 7 focus on theoretical studies and experimental demonstrations of applying radiative cooling, as a PV thermal management strategy, to TPV systems and concentrating PV (CPV) systems.

Specifically, Chapter 6 presents designs of a spectrally-selective radiative cooler and its theoretical cooling effect on a TPV system.

Chapter 7 presents an experimental demonstration of radiative cooling on a CPV system. The demonstrated cooling strategy can be extended to a TPV system.

6. IMPROVING TPV THERMAL MANAGEMENT THROUGH RADIATIVE COOLING[1]

Radiative cooling has recently garnered a great deal of attention for its potential as an alternative method for photovoltaic thermal management. Here, we will consider the limits of radiative cooling for thermal management of electronics broadly, as well as a specific application to thermal power generation. We show that radiative cooling power can increase rapidly with temperature, and is particularly beneficial in systems lacking standard convective cooling. This finding indicates that systems previously operating at elevated temperatures (e.g., 80 °C) can be passively cooled close to ambient under appropriate conditions with a reasonable cooling area. To examine these general principles for a previously unexplored application, we consider the problem of thermophotovoltaic (TPV) conversion of heat to electricity via thermal radiation illuminating a photovoltaic diode. Since TPV systems generally operate in vacuum, convective cooling is sharply limited, but radiative cooling can be implemented with proper choice of materials and structures. In this work, realistic simulations of system performance are performed using the rigorous coupled wave analysis (RCWA) techniques to capture thermal emitter radiation, PV diode absorption, and radiative cooling. We subsequently optimize the structural geometry within realistic design constraints to find the best configurations to minimize operating temperature. It is found that low-iron soda-lime glass can potentially cool the PV diode by a substantial amount, even to below ambient temperatures. The cooling effect can be further improved by adding 2D-periodic photonic crystal structures. We find that the improvement of efficiency can be as much as an 18% relative increase, relative to the

[1]Adapted from: Z. Zhou, X. Sun, and P. Bermel, "cooling for thermophotovoltaic systems," in *Infrared Remote Sensing and Instrumentation XXIV*, vol. 9973. International Society for Optics and Photonics, 2016.

non-radiatively cooled baseline, as well as a potentially significant improvement in PV diode lifetime.

6.1 Introduction

Radiative cooling is a strategy to dissipate excess heat into remote heat sinks (such as the clear sky) via thermal radiation [68]. The crucial value of this technique is in enabling additional *passive* cooling for lower temperature operation of a broad range of solid-state devices than otherwise possible. The key for this approach to create a substantial benefit is achieving enhanced radiation over a window where the medium of exchange is highly transmissive [69]; for the sky, this corresponds to a transparency window of approximately $8-13$ μm [70]. Early work showed the potential for limited selectivity in certain materials, notably titanium dioxide [74, 75], amorphous silicon oxides [78], silicon nitrides [77], and zinc sulfides [74]. While the cooling power of zinc sulfides is calculated to be quite significant at 52 W/m^2 [74], it is much smaller in experiments [76]; it is also difficult to find a natural material that has a perfect match to the ideal, and thus a higher radiative cooling power.

Fortunately, with the emergence of new classes of selective infrared emitters [11, 20, 79], based on photonic design principles [80], interest in this approach has increased substantially in the last several years. Recent calculations first indicated, for instance, that 2D nanophotonic structures can provide a cooling power in excess of 100 W/m^2 at reasonable temperatures [81]. A 1D stack of hafnia and silica, consisting of seven bilayers, was shown to be sufficient to achieve cooling below ambient temperatures in experiment [82]. In related work, it was shown that this approach can be applied to solar cells to theoretically achieve cooling as much as 18.3 °C below ambient [83], with an actual 13 °C cooling effect being observed in experiment [84]. Similarly, despite their lower self-heating, GaAs nanowire-based photovoltaics could potentially experience a radiative cooling of 7 °C [85]. As a result, it was estimated that a performance improvement of 2.6% absolute in photovoltaic performance could

be achieved for photovoltaics in near-earth orbit [86].

Given these significant benefits, it seems appropriate to consider what other systems could potentially benefit from the radiative cooling approach. Clearly, the most appealing application space would be devices with considerable self-heating and a significant need for energy efficiency. Within this group, concentrating photovoltaics and thermophotovoltaics stand out as particularly relevant. The former is a clear extension of prior work on flat-plate photovoltaics, where it may be more valuable because of elevated operating temperatures, which can reach 140 °C under 24 suns when using traditional passive cooling techniques [132]. Similarly, thermophotovoltaics can experience radiative heating on the order of hundreds of suns. However, the overall challenges with temperature regulation are likely to be much more severe for two key reasons: (1) reduced opportunities for cooling, given that TPV systems typically operate in vacuum to limit convection from an emitter up to 1500 °C [61]; and (2) greater sensitivity in the open circuit voltage to elevated temperatures, due to the smaller photovoltaic bandgap [153]. Thus, even water-cooled TPV systems typically can only go down to temperatures around 65 °C [201], and often exceed 200 °C with only passive cooling components. The resulting drop in efficiency can be tremendous; potentially, over 50% of the relative performance [88].

As a result, it is critical to develop new strategies for cooling thermophotovoltaic systems that are nearly or fully passive, as opposed to active, to preserve overall system efficiencies and to substantially decrease operating temperatures, improving TPV system performance. In the best case, this additional cooling power could result in operation below ambient, potentially enabling record TPV efficiencies. In this manuscript, we develop a physics-based modeling framework to capture the energy balance observed in a realistic thermophotovoltaic system. We use this model to investigate the impact of introducing radiative cooling in the ideal case, and then consider a small set of simple structures based on real materials, such as low-iron soda-lime glass, some of which take advantage of nanophotonic design principles. We then show the benefit of increasing the area of the radiative cooling element, given a

suitable heat spreader, and then show conditions under which below-ambient cooling can be achieved. We conclude by showing a clear path to experimental demonstration.

6.2 Calculation Framework

To model the performance of the photovoltaic cells in a TPV setup, we must calculate the energy balance of the system, by tracking its heat inputs and outputs as illustrated in Fig. 6.1, which include: (a) P_{abs}, the thermally emitted power absorbed by the photovoltaic (PV) cell; (b) P_{out}, the electrical output from the PV cell to the external load; (c) $P_{rad,cell}$, the emission from radiative recombination in the cell; (d) P_{rad}, the thermal radiation from the cooling emitter to the atmosphere; (e) P_{atm} and P_{sun}, the absorbed radiation from the atmosphere and the Sun; and (f) P_{conv}, the convective heat transfer to the ambient air. In the steady state, these inputs and outputs must balance, which yields this expression:

$$\begin{aligned} P_{abs}(T_{Emitter}) + P_{atm}(T_A) + P_{sun} = P_{rad}(T_A, T_{Cell}) + P_{rad,cell}(T_{Cell}) \\ + P_{out}(T_{Cell}) + P_{conv}(T_A, T_{Cell}), \end{aligned} \tag{6.1}$$

To quantitatively investigate the cooling effects, we have developed an opto-electro-thermal coupled simulation to investigate the temperature of the photovoltaic cell under different cooling conditions. Optically, we calculated the absorbed and emitted power (P_{abs}, P_{atm}, P_{sun}, and P_{rad}) by integrating over the full emissivity/absorptivity spectrum (from 0.3 μm to 40 μm). Electrically, the output power (P_{out}) as well as radiative recombination ($P_{rad,cell}$) from the PV cell is calculated using detailed balance, i.e., the ShockleyQueisser limit [202], for the equilibrium cell temperature and input spectrum. Thermally, the convective power is calculated based on the temperature difference between the cell and the ambient. Finally, we self-consistently solve for the steady-state temperature of the PV cell by solving Eq. 6.1. We have made the following assumptions to investigate the cooling gain in the best case: (i) the selective thermal emitter inside the TPV is at 1500 K, with a unity emissivity profile between E_g and $E_g + 0.07$ eV, where $E_g = 0.7$ eV is the bandgap

of the PV diode and 0.07 eV bandwidth is to maximize the TPV efficiency [11]; (ii) the TPV efficiency is defined as $\eta = P_{out}/P_{abs}$ and photon recycling is not included. Since all the emission from the emitter are above the bandgap and fully absorbed by the PV diode, $P_{abs} = P_{emit}$; (iii) the metal layer sandwiched between PV cell and cooling emitter is assumed to be a perfect thermal conductor, so that the temperature profile is uniform, and there is no lateral temperature gradient; (iv) the atmospheric transmittance profile is for New Delhi at Spring [203]; and (v) the effective convective coefficient h is only 2.5 $\mathrm{W/(K\,m^2)}$, which aids in achieving below-ambient cooling, as will be explained later.

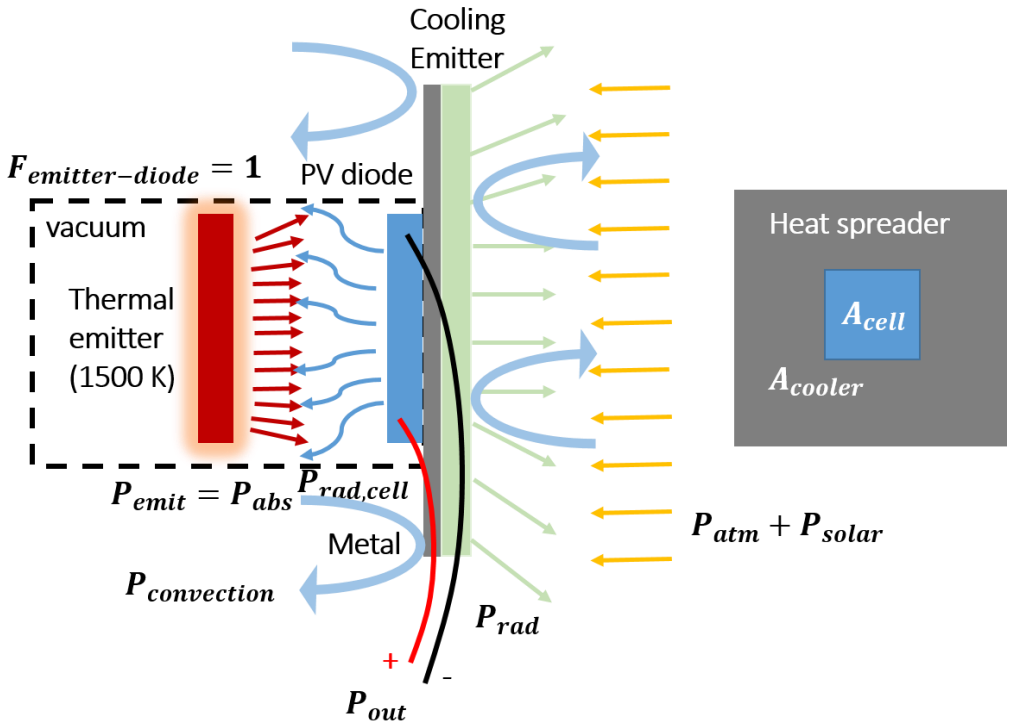

Fig. 6.1. Schematic of a TPV system with outdoor radiative cooling. The thermal emitter and the PV diode are enclosed in a vacuum chamber. The cooling emitter and part of the heat spreader are exposed to ambient with certain amount of convection. The area of the cooling emitter, A_{Cooler}, can be larger than that of the PV diode, A_{Cell}.

Two of the key design factors in the cooling system are the choice of cooling emitter structure and the area ratio between the PV cell and the cooling emitter. We begin by investigating two ideal emitters with emission windows of 2.5 μm−40 μm and 8 μm−13 μm, respectively. The first one is chosen to minimize thermal solar absorption (with a cutoff of 2.5 μm) and ensure that the bandwidth is wide enough to maximize thermal radiation (radiation above 40 μm is negligible for objects at $\sim$ 300 K). The spectral response of the latter emitter perfectly matches the transparent atmospheric window between 8 μm−13 μm [69], which allows direct radiative energy exchange with the cosmic background at $\sim$ 3 K. Fig. 6.2 demonstrates the cooling effect as a function of the area ratio. At a low area ratio, the cell temperature with both cooling radiators is significantly lower than without radiative cooling. But the cooling effect is still unsatisfactory since the efficiency is far below the one with $T_{Cell} =$ 300 K, as shown in Fig. 6.2 (b). As area ratio increases, T_{Cell} drops substantially to even below ambient and then saturates due to convection. It is worth noting that radiative cooling allows the PV diode to operate below 300 K, resulting in an improved TPV efficiency limit. For $T_{Cell} > 300$ K, the 2.5 μm−40 μm cooling emitter provides a superior cooling effect than that of the 8 μm−13 μm emitter, because of larger thermal radiation with broader emission width. However, the opposite result occurs for $T_{Cell} < 300$ K (i.e. 8 μm−13 μm emitter cools more). This can be explained by the reduction in thermal emission from the atmosphere (300 K) associated with using a narrower bandwidth.

In the next section, we will propose realistic designs of the thermal emitters, and demonstrate the corresponding cooling gain using the aforementioned opto-electro-thermal coupled simulation framework.

6.3 Radiative Cooling Emitter Design and Results

The cooling emitter structure proposed in this work consists of a 1.5 mm-thick slab of low-iron soda-lime glass. This material is a good candidate for day-time radiative

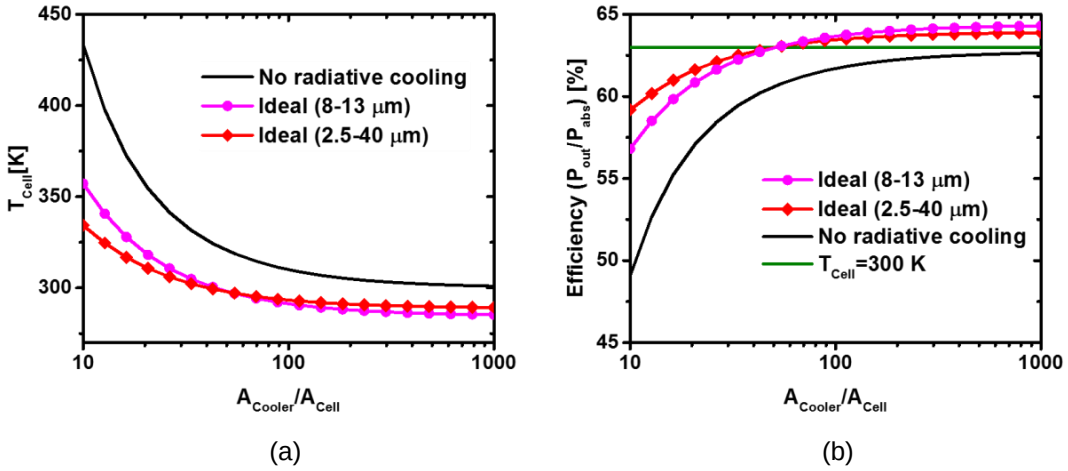

Fig. 6.2. (a) PV diode temperature as a function of the ratio of the cooler to cell areas for convection with $h = 2.5$ W/(K m^2). Both ideal selective cooling emitters represent a great improvement, and may achieve below-ambient cooling for a sufficiently large area ratio. Above ambient temperatures, the ideal selective cooling emitter with an emission band of 2.5 μm−40 μm (red curve) is most effective, while below ambient, the ideal selective cooling emitter with an emission band of 8 μm−13 μm (magenta curve) is most effective; (b) TPV conversion efficiency as a function of area ratios at a given $h = 2.5$ W/(K m^2). For a sufficiently large area ratio, the radiative cooling improves the optimal TPV conversion efficiency via below-ambient cooling.

cooling for solar panels due to its high emittance in mid-IR and low absorption in solar spectrum [120]. The angular dependent emittance spectra are simulated by S4 [171]. For all the optical simulation results in this work, a Drude model silver back reflector with 1 μm thickness is added at the back of the soda-lime glass to capture the reflection from the heat spreader in the proposed structure in Fig. 6.1. The dispersion of low-iron soda-lime glass is taken from [204]. As shown in Fig. 6.3 (b), the emittance spectrum of a bare glass has a dip within the atmospheric window (shaded region). Such non-ideality reduces the radiative cooling power that can transmit through the atmosphere. It has been proposed that properly designed photonic crystal (PhC) structures can enhance the thermal emission over a broad spectral range, including

the atmospheric window, and show better cooling effects [84]. Following the same idea, a simple 2D low-iron soda-lime PhC is proposed in this work to enhance its radiative cooling effect for TPV systems. The schematics of the PhC cooling emitter design is shown in Fig. 6.3 (a). It consists of a square lattice of air holes with a lattice constant of $a = 6$ μm. Each air hole has a radius of $r = 2.5$ μm and depth of $d = 10$ μm. The simulated emittance spectrum of the low-iron soda-lime PhC, as shown in Fig. 6.3 (b), shows a substantial improvement over the bare soda-lime glass. Its emittance in the atmospheric window is closer to unity, while the absorption in solar spectrum is kept below 0.1; this ensures below ambient cooling, *even in the daytime*.

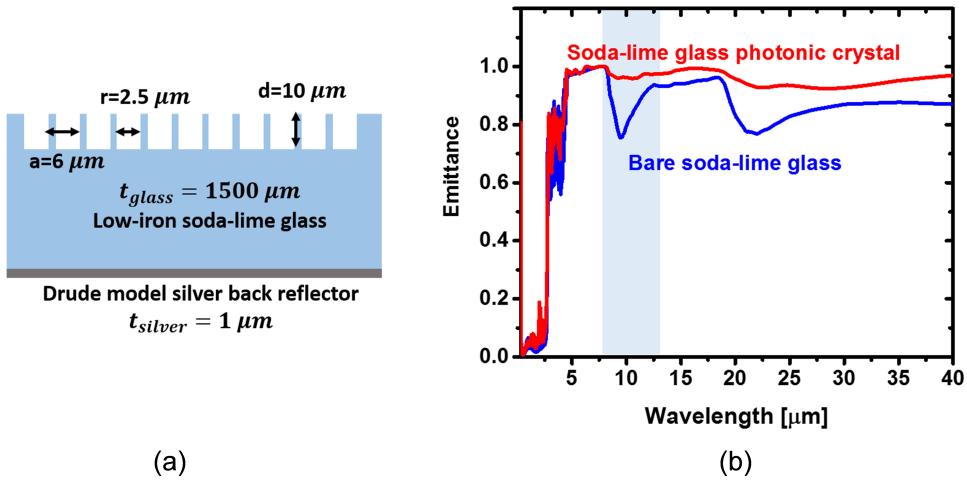

Fig. 6.3. (a) Schematics of the soda-lime PhC cooling emitter structure. The proposed structure has a 2D square lattice of air holes etched into the 1.5 mm-thick low-iron soda-lime glass slab. The radius and the depth of each air hole are 2.5 μm and 10 μm, respectively. The back reflector is a 1 μm thick Drude model silver layer; (b) Simulated emittance spectrum of the bare low-iron soda-lime glass (blue curve); the low-iron soda-lime PhC (red curve). Obviously, the PhC structure improves the emission within the atmospheric window (shaded region).

The performance of the proposed cooling emitters is examined by the same calculation framework discussed in the previous section. As shown in Fig. 6.4 (a), the temperature of the PV diode, T_{Cell}, decreases with the increasing area ratio. Assuming a convection coefficient $h = 2.5$ W/(K m^2), bare low-iron soda-lime glass achieves below-ambient cooling when the area ratio $A_{Cooler}/A_{Cell} = 88.6$. With the thermal emission in atmospheric window enhanced, low-iron soda-lime PhC achieves below-ambient cooling at a slightly lower area ratio of $A_{Cooler}/A_{Cell} = 69.5$. To see the effect of radiative cooling, the area ratio dependency of PV diode temperature without radiative cooling is plotted in Fig. 6.4 (a) for comparison. The inset in Fig. 6.4 (a) shows the comparison of cooling effect with area ratios from 80 to 1000. It is obvious that low-iron soda-lime based cooling emitters reduce the temperature of the PV diode in a TPV system by a fair amount. Furthermore, the PhC structure improves the cooling effect and gives lower T_{Cell}. Under the conditions where $A_{Cooler}/A_{Cell} = 88.6$ and $h = 2.5$ W/(K m^2), for example, the bare low-iron soda-lime glass cooling emitter contributes a 12.3 K temperature drop via radiative cooling and the low-iron soda-lime PhC has a slightly larger cooling of 13.0 K.

In Fig. 6.4 (b), TPV conversion efficiencies are calculated at different area ratios. Apparently, radiative cooling from low-iron soda-lime based cooling emitters can greatly improve the conversion efficiency of a TPV system. When the area ratio is 10, operating temperature drops from 434 K to around 343 K with bare low-iron soda-lime emitter, a difference of 91 K, resulting in an efficiency rise from 49% to 58%, an increase of 9% absolute or 18% relative. Additionally, a recently developed model for photovoltaic reliability suggests that every 20 K drop in operating temperature can increase the mean time between failures a factor of 2 for certain failure modes, which would suggest a lifetime improvement up to a factor of 23, although clearly other failure modes could be much less temperature-dependent [87]. Furthermore, when below-ambient cooling is achieved with a sufficiently large area ratio, the conversion efficiency starts to exceed the optimal value calculated for when $T_{Cell} = 300$ K. Therefore, radiative cooling with low-iron soda-lime glass based emitters not only

has the potential of resolving heating effect on PV diodes, but also improves the TPV performance due to its below-ambient cooling potential. It should be noted as well that daytime operation of outdoor TPV is assumed in all our calculations. In fact, TPV systems are capable of 24-hour operation. During the nighttime, a larger radiative cooling effect and conversion efficiency improvement should be expected, since the radiative cooler no longer risks absorbing solar irradiance.

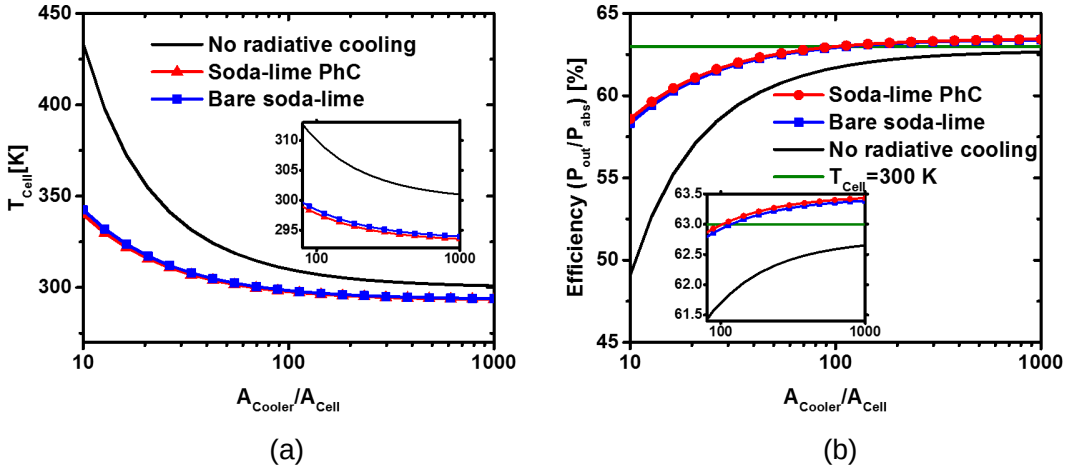

Fig. 6.4. (a) PV diode temperature as a function of area ratios at a given convective coefficient of 2.5 W/(K m^2). For a sufficiently large area ratio, both bare low-iron soda-lime glass and low-iron soda-lime PhC achieve below-ambient cooling. The PhC structure slightly improves the cooling effect; (b) TPV conversion efficiency as a function of area ratios at a given convective coefficient of 2.5 W/(K m^2). For a sufficiently large area ratio, both cases improve the TPV conversion efficiency via below-ambient cooling. The PhC structure gives slightly higher efficiency compared with the bare low-iron soda-lime glass.

6.4 Conclusions

In this work, we propose to exploit radiative cooling as the passive cooling mechanism to resolve the heating effect on the PV diode of a TPV system. The area ratio

between the cooling emitter and the PV diode plays an important role. When the area ratio is sufficiently large, below-ambient cooling can be achieved and TPV conversion efficiency is further improved. Such below-ambient cooling effect can hardly be achieved through other passive cooling mechanisms. Through simulations of realistic materials, we show that low-iron soda-lime glass can potentially cool the PV diode by a substantial amount, even to below ambient temperatures. The cooling effect can be further improved by adding PhC structures. We find that the improvement of efficiency can be as much as an 18% relative increase, and the increase in mean time between failures can be great as 2200%. Our results show that effective radiative cooling in TPV systems may be achieved by using relatively simple materials and structures. In future work, it would be appropriate to experimentally test these predictions and characterize the actual effects on temperature and efficiencies under steady-state operation. Some non-idealities may need to be added to the model to achieve a close match to experimental results.

7. RADIATIVE COOLING FOR LOW-BANDGAP PHOTOVOLTAICS UNDER CONCENTRATED SUNLIGHT[1]

Radiative cooling is a uniquely compact and passive cooling mechanism. Significant applications can be found in energy generation, particularly concentrating photovoltaics (CPV) and thermophotovoltaics (TPV). Both rely on low-bandgap PV cells that experience significant reductions in performance and lifetime when operating at elevated temperatures. This issue creates a significant barrier to widespread adoption. To address this challenge, we demonstrate enhanced radiative cooling for low-bandgap PV cells under concentrated sunlight for the first time. A composite material stack is used as the radiative cooler. Enhanced radiative cooling reduces operating temperatures by 10 °C, translating into a relative increase of 5.7% in open-circuit voltage and an estimated increase of 40% in lifetime at 13 suns. By using a model, we also estimate that the same setup could achieve an improvement of 34% in open-circuit voltage for 35 suns, which could reduce levelized costs of energy up to 33% for high-activation energy failure modes. The radiative cooling enhancement demonstrated here is a simple and straightforward approach, which can be generalized to other optoelectronic systems.

7.1 Introduction

Radiative cooling is a passive cooling mechanism that dissipates excessive heat to the clear sky via thermal radiation [68, 72, 205]. The uniqueness of radiative cooling stems from the existence of atmospheric transmission windows in the infrared [68,69].

[1]Adapted from: Z. Zhou, Z. Wang, and P. Bermel, "Radiative cooling for low-bandgap photovoltaics under concentrated sunlight," *Optics Express*, vol. 27, no. 8, 2019.

Radiation of photons that have wavelengths within these windows (e.g., $8-13$ μm, can be transmitted through the atmosphere to exchange heat with the cosmic background at a temperature of about 3 K [89]. This property creates an effective heat sink that allows passive cooling [82, 102]. Two types of radiative cooling have been studied in the literature: above and below ambient cooling. The distinction is that above-ambient cooling aims to encompass nearly the entire blackbody spectrum for maximal cooling power at temperatures above ambient. For daytime applications specifically, the radiative cooler for above-ambient cooling should have near-zero emittance within the solar spectrum ($0.3-2.5$ μm) and high, broadband emittance otherwise. In below-ambient cooling, exchange is strictly limited to atmospheric transmission windows, to prevent reheating by the ambient outside the transmission window. Therefore, the radiative cooler for below-ambient cooling should have high spectral selectivity with strong emittance only within the atmospheric windows (particularly $8-13$ μm), with near-zero emittance otherwise.

To achieve optimal cooling in both cases, various radiative cooling materials have been proposed and demonstrated. Early work starting in the 1970s focused on below-ambient cooling via bulk materials with strong emittance peaks overlapping the atmospheric transmission windows [69, 77, 105, 109]. In the last decade, improved performance has been achieved using nanophotonic structures to further suppress out-of-band absorption [81, 82, 115]. Recently, radiative coolers suitable for above-ambient cooling have been studied. Multilayer stacks [131, 206], photonic crystals [83, 84, 116, 207] and metamaterials [208] with high broadband mid-IR thermal emittance have been proposed, fabricated, and shown to exhibit passive cooling capabilities in experiments. Daytime radiative cooling may also be further enhanced by angular selectivity, as calculated theoretically [209] and demonstrated experimentally [210]

The unique, passive nature of radiative cooling makes it an important approach to meet increasing demands for thermal management when energy efficiency is at a premium. For instance, using radiative cooling for more energy efficient heating,

ventilation, and air conditioning (HVAC) has recently been demonstrated in several studies [117, 211–213]. The theoretical limit of energy conversion also increases with larger temperature gradients, based on Carnots law. As a result, novel energy [214] and water harvesting strategies [215, 216] based on below-ambient radiative cooling have also been proposed.

Another related application is the thermal management of photovoltaics (PV). First, the overall PV diode efficiency generally drops substantially with operating temperature [217]. Another challenge imposed by the elevated temperature is decreased lifetime, since many failure modes are strongly related to thermal-activated degradation [87, 218]. Above-ambient radiative cooling, with higher cooling power density than below-ambient cooling, is more suitable for supplementing the cooling capability of PV systems. Recent theoretical and experimental studies have applied radiative cooling to flat-plate PV systems [83, 84, 120, 207]. For instance, a comprehensive cooling method combining radiative cooling with sub-bandgap filtering has been proposed [87, 131]. To date, the greatest temperature reduction achieved experimentally without vacuum is about 13 °C [84]. Although an open-circuit voltage (V_{OC}) improvement of a PV cell was not demonstrated in that experiment, if the silicon (Si) absorber were replaced by a state-of-the-art Si solar cell, and its V_{OC} decreased linearly with temperature at a rate of -2.2 mV/°C [217], the reduction in temperature would translate to a relative increase in open-circuit voltage (V_{OC}) of around 4.7%. For PV applications with high incident powers, such as concentrating photovoltaics (CPV) and thermophotovoltaics (TPV), cooling is far more critical due to the higher heat loads and the typical use of low-bandgap PV diodes. A higher heat load will result in higher operating temperatures when cooling is insufficient, and the consequential relative decrease in V_{OC} will usually be greater for lower bandgap PV diodes. Furthermore, the PV reliability challenge is much greater in CPV and TPV systems, because of the higher operating temperatures [87]. Therefore, radiative cooling may yield more benefits in these cases. A configuration of CPV systems with Fresnel lens concentrators is shown in Fig. 7.1. The radiative cooler may surround the solar cell

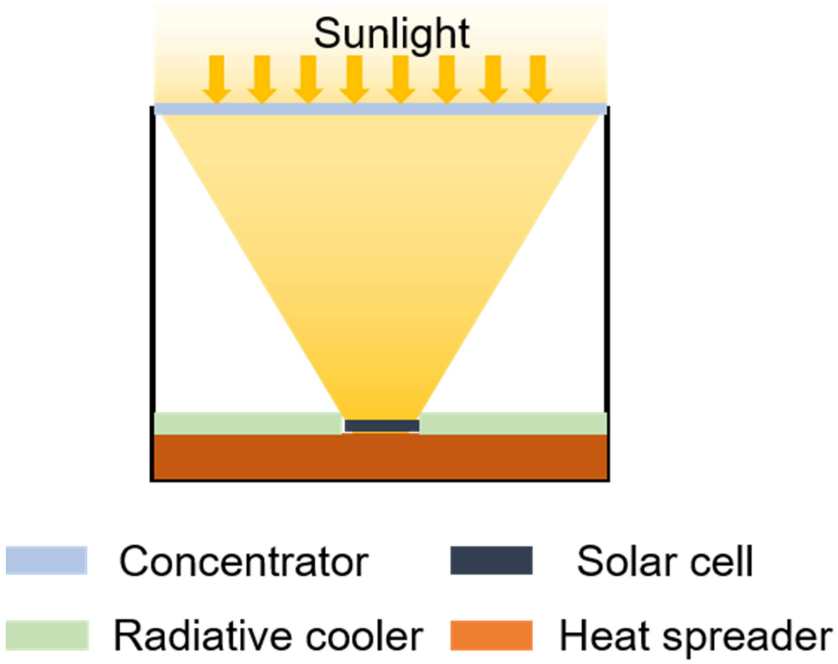

Fig. 7.1. A concentrating photovoltaic (CPV) system with a Fresnel lens concentrator and an enclosure. The radiative cooler can be added to the heat spreader underneath the solar cell.

at the center. The heat spreader below conducts heat from the solar cell to the cooler. Such configuration approximately maintains the footprint of the original structure, as long as the radiative cooler is smaller than the concentrator.

Significant cooling has been predicted by theoretical studies of radiative cooling on CPV [87, 131, 133] and TPV systems [116]. However, few experimental demonstrations have been reported. In this work, we apply enhanced radiative cooling to a low-bandgap GaSb PV diode in a CPV configuration. The enhanced radiative cooling is achieved by a cooling assembly that significantly increases the radiative cooling capability of an off-the-shelf PV diode. The temperature reduction due to radiative cooling and its instantaneous enhancement in PV performance are experimentally demonstrated in a field test. Theoretical models are developed to compare with experimental results for a better understanding of its performance. In the following

sections, the methodologies of the experiment and modeling are introduced first, followed by the discussion of results from the outdoor field test. Finally, we conclude by discussing the key findings in this work and potential directions for future research.

7.2 Methodology

7.2.1 Outdoor Field Test Setup

The demonstration of radiative cooling on low-bandgap PV under high input power resembles the structure shown in Fig. 7.1. Next, we present our experimental design for outdoor tests.

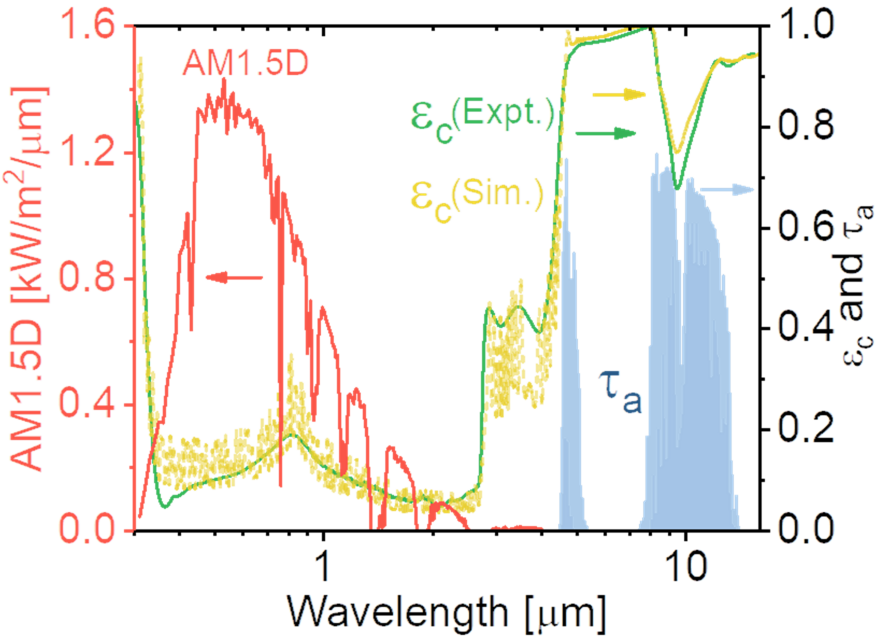

Fig. 7.2. Emittance spectrum of soda-lime glass radiative cooler (ϵ_c). The simulation (dashed yellow curve) matches well with the measurement (solid green curve). The spectrum of AM1.5D (red curve) and atmospheric transmittance (τ_a) of mid-latitude summer sky (blue shaded region) are plotted together. The low absorption in solar spectrum and strong emission in atmospheric window makes the cooler suitable for daytime above-ambient radiative cooling.

The radiative cooler used in this work is a composite material stack that consists of soda-lime glass, an inexpensive material, and aluminum (Al). It combines both the high reflectivity of Al over a broad spectral range and the spectral selectivity of soda-lime glass. Multilayer structures [133] and photonic crystal structures [116] based on soda-lime glass have been proposed as radiative coolers in prior works. For scalability, the radiative cooler used in this work is a 550 μm thick double-side polished soda-lime glass wafer (1631, UniversityWafer Inc.) with 300 nm Al evaporated on its backside. As shown in Fig. 7.2, the measured emittance of soda-lime glass radiative cooler (solid green curve) exhibits desirable spectral selectivity for daytime radiative cooling. Its low emittance in solar spectrum (red curve) suppresses the absorption of incoming solar irradiance. Beyond the solar spectrum, high emittance covers a broad spectral range including the atmospheric window (blue shaded region), allowing strong thermal radiation that is favorable to above-ambient cooling. Furthermore, the measured performance of soda-lime glass radiative cooler can be reproduced via optical simulations using S4 (dashed yellow curve) [171]. The optical constants used to model the cooler are extracted from references [204, 219].

In addition to the aforementioned spectral selectivity, a good radiative cooler for daytime above-ambient cooling should have strong mid-IR emittance over the entire hemisphere. Therefore, the specular reflectance of soda-lime glass radiative cooler is measured using an FTIR (Nexus 670, Thermo Fisher Scientific) at various incident angles (30°, 40°, 50°, 60°). The emittance is calculated by (1reflectance) following Kirchhoffs Law. As shown in Fig. 7.3 (b), the measured emittance shows good uniformity over the measured angles. It also matches well with the simulation, shown in Fig. 7.3 (a), with only minor differences. A close match between experiment and simulation, as indicated in Figs. 7.2 and 7.3, allows us to use simulated cooler emittance in the model discussed in the next section, as it covers a broader spectral range than the measured emittance.

Our experimental setup consists of three polystyrene foam chambers. As shown in Fig. 7.4 (a), each chamber is sealed with a piece of 15 μm thick low-density

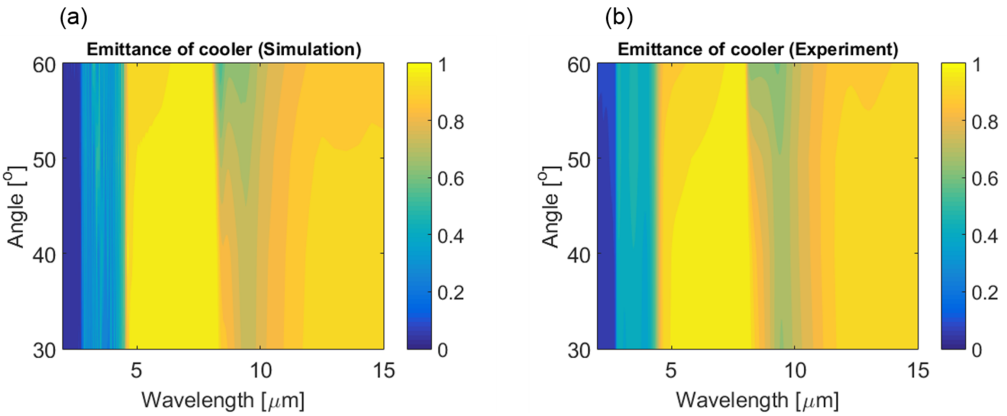

Fig. 7.3. Comparison between simulated and the measured angular dependent emittance of the soda-lime glass radiative cooler. (a) Simulated emittance of the cooler as a function of wavelength and angle. (b) Measured emittance of the cooler as a function of wavelength and angle. The simulation matches closely with the experiment.

polyethylene (LDPE) film (ET311115, Goodfellow Co.). It limits convection and provides high transmission over a broad spectral range, as shown in Fig. 7.5, keeping the radiative heat transfer almost unaffected. The enclosure with polystyrene foam side walls strongly suppresses conduction and convection. To concentrate the incoming sunlight and maintain radiative cooling in mid-IR, a special IR-transparent Fresnel lens (IR Fresnel Lens, Edmund Optics) is mounted above each chamber. Its transmittance spectrum is shown in Fig. 7.6. Its position is adjustable, to tune the focused sunlight beam spot. Inside the chamber sits the cooling assembly [Fig. 7.4 (b)]. It consists of a GaSb PV diode, a copper heat spreader and a radiative cooler. Electrical probes are connected to the diode to measure V_{OC} in real time. A type-K thermocouple (TC, SCASS-020U-12-SHX, Omega) is connected to the rear side of the copper heat spreader to monitor the assembly temperature T_{expt}. Both V_{OC} and T_{expt} are collected by a data acquisition instrument (DI-245, DATAQ Instruments) at a sampling rate of 0.25 Hz at resolutions of 0.12 mV and 0.096 °C, respectively.

Fig. 7.4 (c) is a photo of the cooling assembly in Fig. 7.4 (b). The GaSb PV

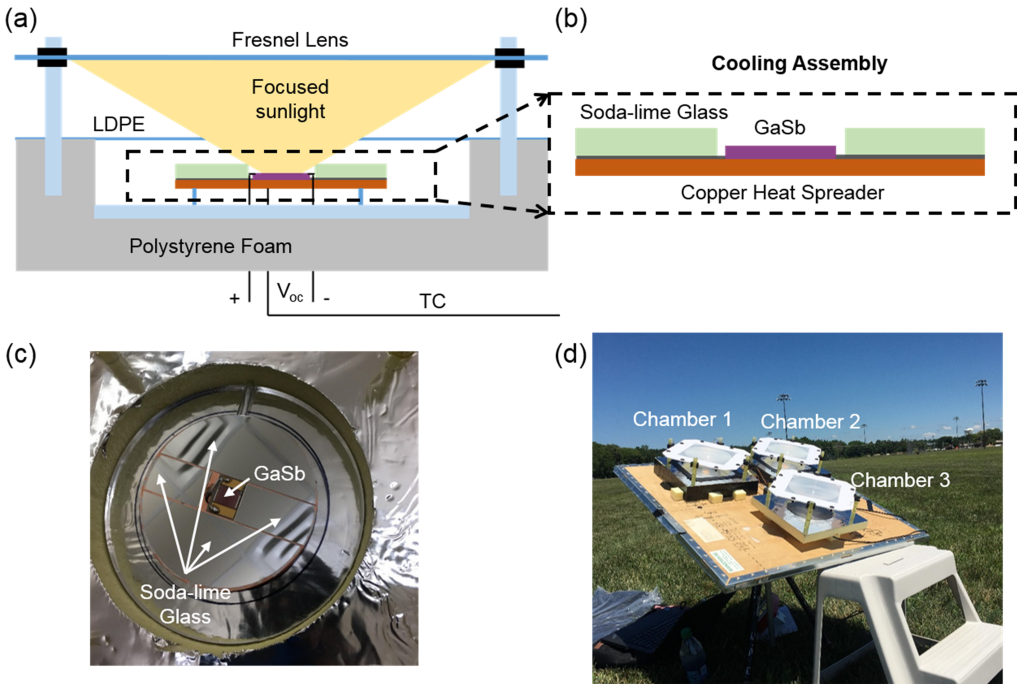

Fig. 7.4. Experimental setup to test radiative cooling in a CPV system. (a) A schematic of the testing chamber. Temperature and open-circuit voltage are measured in real time. (b) An expanded schematic of the cooling assembly consisting of PV diode (GaSb) and the cooler (soda-lime glass). A piece of copper serves as the heat spreader. (c) A picture of the structure in (b). (d) Picture of the entire setup during an outdoor test. Chamber 1 (with radiative cooler) and Chamber 2 (without radiative cooler) are almost identical while chamber 3 measures the concentrated solar power. The setup is capable of manual solar tracking.

diode is bonded to an aluminum nitride (AlN) substrate. Four soda-lime glass radiative coolers surround the PV diode. Both the PV diode and the radiative coolers are pasted (Pyro-Duct 597-A, Aremco) to the copper heat spreader below to conduct heat from the PV diode to the cooler.

Given the finite thickness of the copper heat spreader, the TC is slightly displaced from the exact position of the PV diode. Therefore, the difference between the actual temperature of PV T_{pv} and T_{expt} should be quantified. Furthermore, the lateral temperature uniformity should be verified as well due to the large surface area of the heat

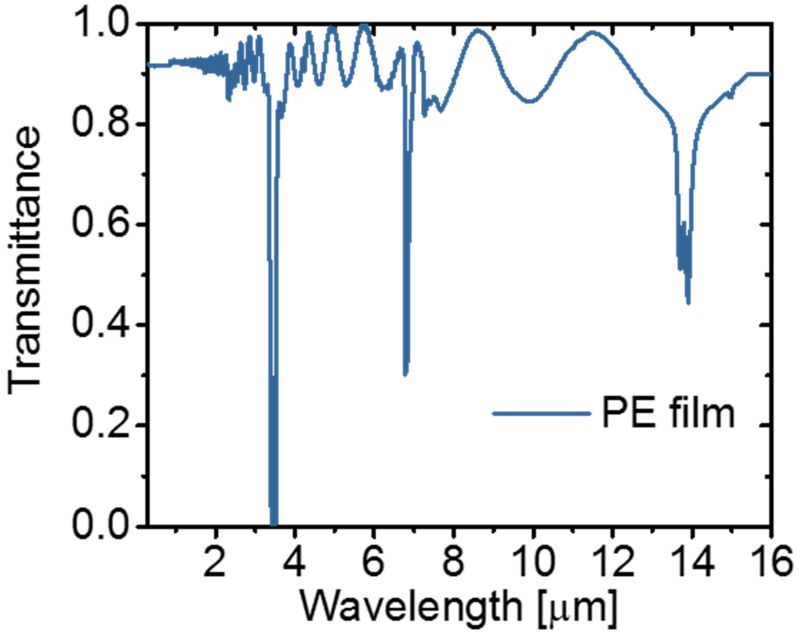

Fig. 7.5. Transmittance spectrum of the low-density polyethylene film. For $0.3-2.5$ μm, the transmittance is measured on a spectrophotometer with an integrating sphere (Lambda 950). For $2.5-15$ μm (yellow shaded region), the transmittance is measured on an FTIR (Nexus 670). In the model, the transmittance beyond 15 μm is extrapolated as 0.899.

spreader. The temperature uniformity (lateral and vertical) of the cooling assembly is determined by first applying a negative DC bias of 1.9 V to the PV diode to raise its temperature. The current is measured to be 1.2 A. Then, two type-K TCs are used to measure the temperature of the PV diode (Front probe) and the rear side of the copper heat spreader (Rear probe), respectively. As shown in Fig. 7.7 (a) and its inset, the rear side temperature is only 1.5 °C below the PV diode. The temperature of the cooling assembly approaches steady state about 1 hr after the heating starts, and the temperature difference stabilizes 5 minutes after the heating starts. As for lateral temperature uniformity: thermal images, as shown in Fig. 7.7 (b), are taken using an IR camera (Therm-App TH) about an hour after applying the bias. The emissivity

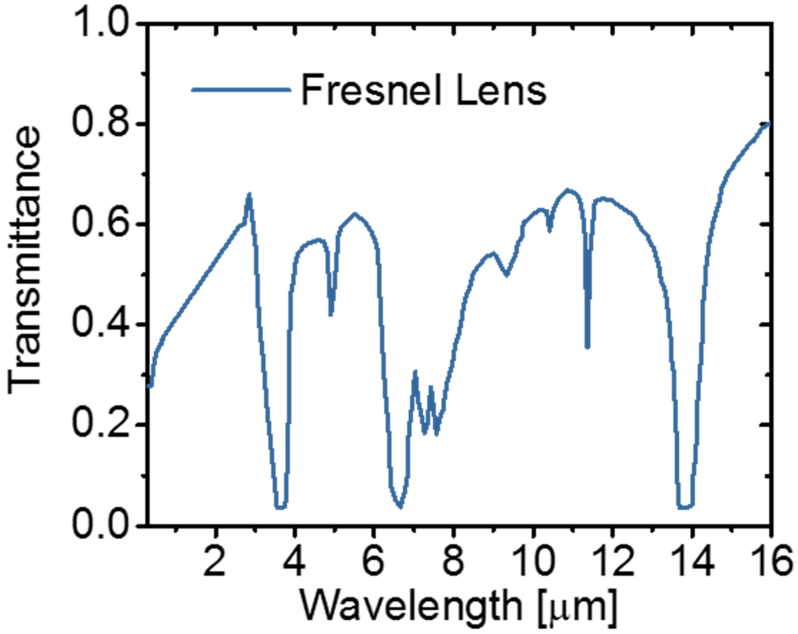

Fig. 7.6. Transmittance spectrum of the IR Fresnel lens, extending up to 25.5 μm is provided by the vendor (Edmund Optics); transmittance beyond is extrapolated to be 0.825.

ϵ is set as 0.72 and the room temperature is set as 20 °C. A uniform temperature distribution is observed across all four pieces of soda-lime glass radiative coolers. The inset of Fig. 7.7 (b) shows a photograph of the cooling assembly. The temperature scale is uncorrected for emissivity; within each material region, it is evident that the temperature is quite uniform. Furthermore, we have shown that good temperature uniformity (within 4 °C) can be achieved at much higher heat loads (up to 30 W/cm^2, equivalent to 300 suns) [133].

Two chambers, Chamber 1 and 2 in Fig. 7.4 (d), are almost identical. Chamber 1 has soda-lime glass radiative cooler on the cooling assembly while Chamber 2, as a reference, has none. The copper heat spreader in the cooling assembly of Chamber 2 is coated with 300 nm Al instead. The emittance of the Al coated copper heat spreader, as shown in Fig. 7.8 , is comparable to the soda-lime glass radiative cooler

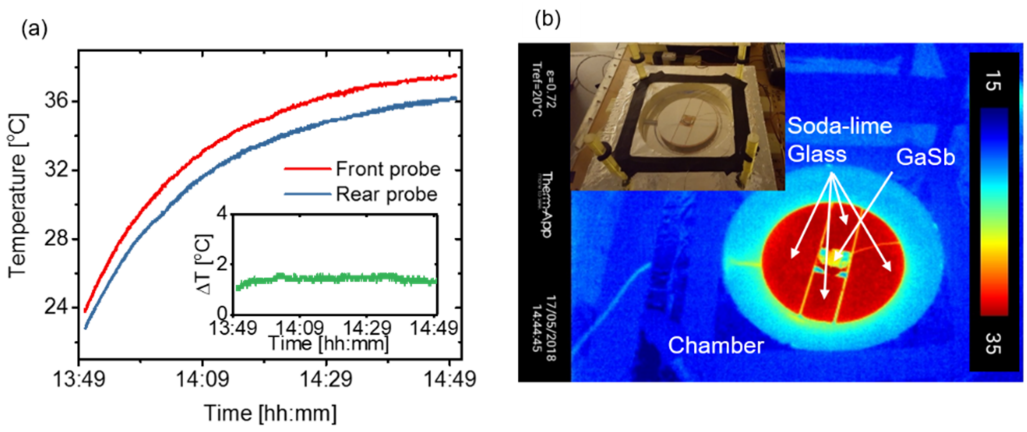

Fig. 7.7. Temperature uniformity of the cooling assembly. (a) The temperature difference between the rear probe (blue line) at the backside of the cooling assembly and the front probe at the GaSb PV diode (red line). Only a slight temperature difference of 1.5 °C is observed. (b) The thermal image of the cooling assembly when a bias is applied to the GaSb PV diode. The temperature scale does not account for differences in emissivity between objects.

throughout the solar spectrum. However, the high DC conductivity of Al ensures low mid-IR emittance. Chamber 3 is designated for concentrated solar power measurements. It resembles the other two in most of its optical components, ensuring the measured solar power is almost identical to that incident on the solar cells in Chamber 1 and 2. A thermal power sensor (S314C, Thorlabs) is inserted. To maintain sufficient convective cooling of the sensor, Chamber 3 is an open compartment. Since it only measures the solar power, it will not be discussed further in subsequent sections. To ensure reliable readings from the thermal power sensor and the data acquisition tool, the setup warms up outside for 30 minutes before tests, to help minimize measurement errors. All three chambers are mounted on a platform, where height, yaw and pitch are manually adjusted to track the sun. Chamber 3 is designate for concentrated solar power measurements. It resembles the other two in aspects of optical components. However, the cooling assembly is replaced by a thermal power sensor (S314C, Thorlabs). To keep sufficient convective cooling to the sensor, Chamber 3 is

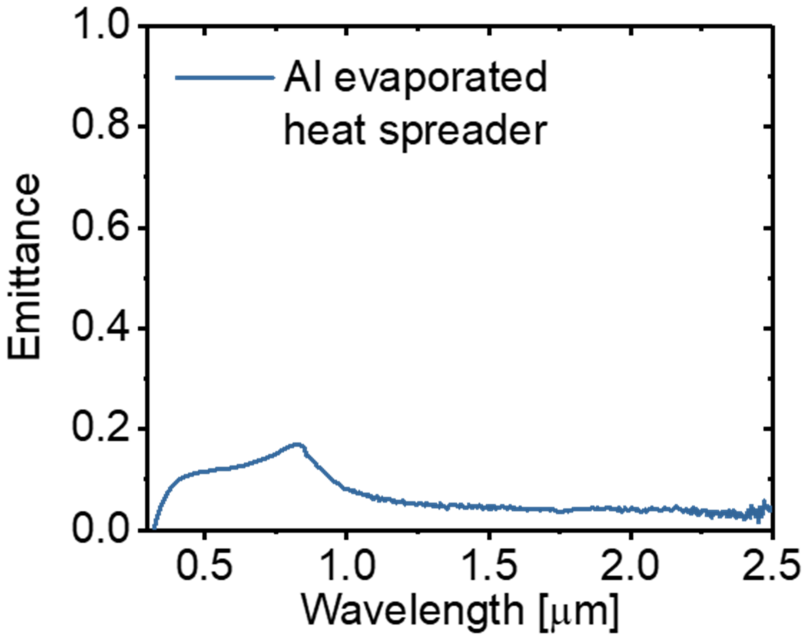

Fig. 7.8. Emittance spectrum of the copper heat spreader evaporated with Al. The emittance is derived from diffuse + specular reflectance measured by a spectrophotometer with an integrating sphere (Lambda 950). In the model, the emittance beyond 2.5 μm is extrapolated as 0.05.

an open compartment. All three chambers are mounted on a platform. Its height, yaw and pitch can be manually adjusted to track the direct sunlight.

7.2.2 Theoretical Models

In conjunction with the experimental setup described above, theoretical models are developed to better understand the outdoor field test results. Two separate models are developed to calculate the steady-state temperature of the cooling assembly and the real-time V_{OC} of the PV diode, respectively.

The first one is to calculate the steady-state temperature of the cooling assembly T_c by solving a power balance equation [82]:

$$P_s + P_a = P_r + P_c, \tag{7.1}$$

where P_s is the total solar power absorbed by the cooling assembly; P_a is the atmospheric thermal emission absorbed by the assembly; P_r is the outgoing radiative power from the assembly at steady-state temperature T_c; and P_c accounts for the outgoing non-radiative heat transfer. This model can be applied to capture the steady-state temperature with and without radiative cooling either in our experimental setup, or a commercially-relevant high-concentration photovoltaic (CPV) setup.

The total absorbed solar power P_s can be calculated as:

$$P_s = P_{cs} + P_{ds}^g + P_{ds}^l, \tag{7.2}$$

where P_{cs} is the absorbed concentrated solar power, P_{ds}^g is the diffuse sunlight absorbed by the cooler through gaps uncovered by the lens, and P_{ds}^l is the diffuse sunlight absorbed by the cooler through the lens.

P_{cs} can be calculated as:

$$P_{cs} = CA_{pv} \int d\lambda \epsilon_{pv}(\lambda) I_{AM1.5D}(\lambda) \tau_{pe}(\lambda) \tau_l(\lambda), \tag{7.3}$$

where C is the solar concentration factor determined by the concentrated solar power P_{sun} measured by Chamber 3 as $C = P_{sun} / \int d\lambda A_{pv} I_{AM1.5D}(\lambda) \tau_{PE}(\lambda) \tau_l(\lambda)$, A_{pv} is the area of the GaSb PV diode; $\epsilon_{pv}(\lambda)$ is the emittance of GaSb PV diodes at wavelength λ (see Fig. 7.9); $I_{AM1.5D}(\lambda)$ is the AM1.5D solar irradiance, and $\tau_{pe}(\lambda)$ and $\tau_l(\lambda)$ are the transmittance of low-density polyethylene film (see Fig. 7.5) and IR Fresnel lens (see Fig. 7.6), respectively.

The absorbed diffuse sunlight can be calculated as:

$$P_{ds}^g = A_c F_g \int d\lambda \overline{\epsilon_c(\lambda)} DHI(\lambda) \tau_{pe}(\lambda), \tag{7.4}$$

$$P_{ds} = A_c F_l \int d\lambda \overline{\epsilon_c(\lambda)} DHI(\lambda) \tau_{pe}(\lambda) \tau_l(\lambda), \tag{7.5}$$

where A_c is the area of the cooler, F_g and F_l are the view factor from the cooling assembly to the uncovered gap and the IR Fresnel lens, respectively. $DHI(\lambda)$ is

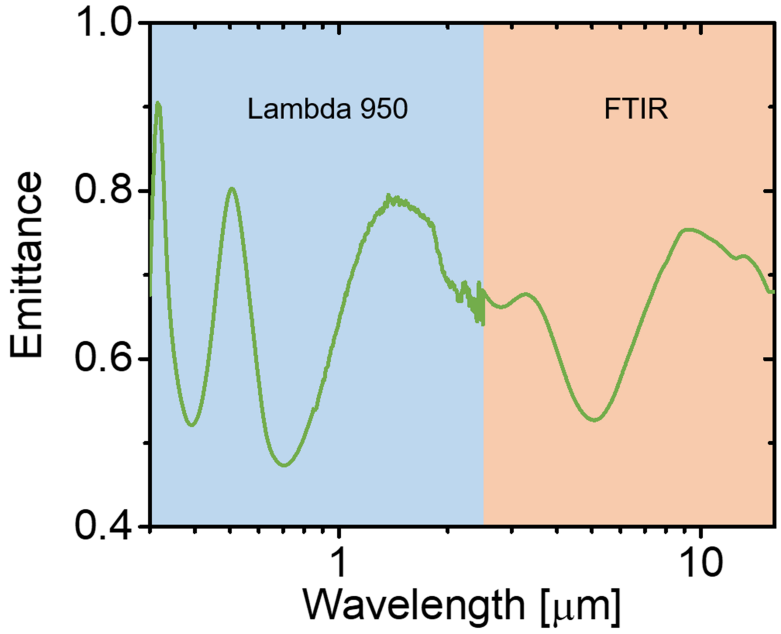

Fig. 7.9. Emittance spectrum of the GaSb PV diode. For $0.3-2.5$ μm (blue shaded region), the emittance is measured by a spectrophotometer with an integrating sphere (Lambda 950). For $2.5-15$ μm (yellow shaded region), the emittance is measured on an FTIR (Nexus 670) at 30° angle of incidence. In the model, the emittance beyond 15 μm is extrapolated as 0.68.

the diffuse horizontal solar irradiance calculated using PVLIB [220], and $\overline{\epsilon_c(\lambda)} = 2\int_0^{\pi/2} d\theta \epsilon_c(\lambda,\theta)\sin(\theta)\cos(\theta)$ is the averaged emittance of the cooler over incident angles θ from 0° to 90°. For the cooling assembly with no radiative cooler, the angular-averaged emittance of the evaporated Al is the same as the experimentally characterized emittance (see Fig. 7.8).

The absorbed atmospheric emission P_a can be calculated as:

$$P_a = F(P_a^{pv} + P_a^{c,g} + P_a^{c,l}), \tag{7.6}$$

where F is the view factor from the radiative cooling platform to the open sky, P_a^{pv} is the atmospheric emission absorbed by the PV diode, $P_a^{c,g}$ is the atmospheric emission

absorbed by the cooler through gaps uncovered by the lens, and $P_a^{c,l}$ is the atmospheric emission absorbed by the cooler through the lens. The quantities in Eq. 7.6 can be calculated as:

$$P_a^{pv} = A_{pv} \int d\lambda \overline{\epsilon_{pv,a}(\lambda)} I_{BB}(\lambda, T_a) \tau_{pe}(\lambda) \tau_l(\lambda), \tag{7.7}$$

$$P_a^{c,g} = A_c F_g \int d\lambda \overline{\epsilon_{c,a}(\lambda)} I_{BB}(\lambda, T_a) \tau_{pe}(\lambda), \tag{7.8}$$

$$P_a^{c,l} = A_c F_l \int d\lambda \overline{\epsilon_{c,a}(\lambda)} I_{BB}(\lambda, T_a) \tau_{pe}(\lambda) \tau_l(\lambda), \tag{7.9}$$

where $\overline{\epsilon_{i,a}(\lambda)} = 2 \int_0^{\pi/2} d\theta \epsilon_i(\lambda, \theta) \epsilon_a(\lambda, \theta) \sin(\theta) \cos(\theta)$ $(i = c \text{ or } pv)$; $\epsilon_a(\lambda, \theta) = 1 - \tau_a(\lambda)^{1/\cos(\theta)}$ is the angular dependent emittance spectrum of the atmosphere with normal transmittance $\tau_a(\lambda)$ [69, 221]. Here, we use a MODTRAN mid-latitude summer sky model is used to represent the transmittance spectrum of the atmosphere at the time of the outdoor field test. $I_{BB}(\lambda, T_a)$ is the blackbody radiation spectrum at ambient temperature T_a.

The radiative cooling power P_r can be calculated as:

$$P_r = F(P_r^{pv} + P_r^{c,g} + P_r^{c,l}), \tag{7.10}$$

where P_r^{pv} is the radiative power emitted from the PV diode, $P_r^{c,g}$ is the radiative power emitted from the cooler through gaps uncovered by the lens, and $P_r^{c,l}$ is the radiative power emitted from the cooler through the lens. The quantities in Eq. 7.10 can be calculated as:

$$P_r^{pv} = A_{pv} \int d\lambda \overline{\epsilon_{pv}(\lambda)} I_{BB}(\lambda, T_c) \tau_{pe}(\lambda) \tau_l(\lambda), \tag{7.11}$$

$$P_r^{c,g} = A_c F_g \int d\lambda \overline{\epsilon_c(\lambda)} I_{BB}(\lambda, T_c) \tau_{pe}(\lambda), \tag{7.12}$$

$$P_r^{c,l} = A_c F_l \int d\lambda \overline{\epsilon_c(\lambda)} I_{BB}(\lambda, T_c) \tau_{pe}(\lambda) \tau_l(\lambda), \tag{7.13}$$

where T_c is the temperature of the cooling assembly. The model assumes that the angular-averaged emittance of the PV diode $\overline{\epsilon_{pv}(\lambda)}$ is the same as the experimentally characterized emittance (see Fig. 7.9).

The non-radiative cooling power P_c is calculated as:

$$P_c = 2A_{cs} h_{eff} (T_c - T_a), \tag{7.14}$$

where h_{eff} is the effective convection coefficient. The assembly surface area is A_{cs}, and the factor of 2 accounts for both top and bottom surfaces.

The second model calculates the real-time V_{OC} of the PV diode at measured temperatures T_{pv} using diode equation. Parameters of the GaSb diode, including dark current density, ideality factor and series/shunt resistance, are determined by fitting its dark I-V measured near room-temperature T_{rt} ($25.2 \pm 0.3\,^{\circ}\mathrm{C}$).

As shown in Fig. 11(b). Using the fitted parameters summarized in the caption of Fig. 7.10, dark current at elevated temperature $I_0(T_{pv})$ is first calculated as [217]:

$$I_0(T_{pv}) = I_0(T_{rt}) \left(\frac{T_{pv}}{T_{rt}}\right)^3 \exp\left[\frac{qE_g^0}{k}\left(\frac{1}{T_{rt}} - \frac{1}{T_{pv}}\right)\right], \tag{7.15}$$

where T_{pv} is the temperature of PV diode, q is the elementary charge, k is the Boltzmann constant, and E_g^0 is the bandgap energy in [eV] of the PV diode at 0 K. An uncertainty of $01.5\,^{\circ}\mathrm{C}$ above the measured T_{expt} is accounted for in the calculation. To remove the noise in temperature measurements, T_{pv} is smoothed using exponentially weighted moving-average with an exponential weighting factor $\alpha = 0.05$.

After $I_0(T_{pv})$ is calculated, the V_{OC} can be calculated by solving the following equation:

$$I_{SC} = I_0(T_{pv}) \left[\exp\left(\frac{qV_{OC}}{nkT_{pv}}\right) - 1\right] + \frac{V_{OC}}{R_{sh}}, \tag{7.16}$$

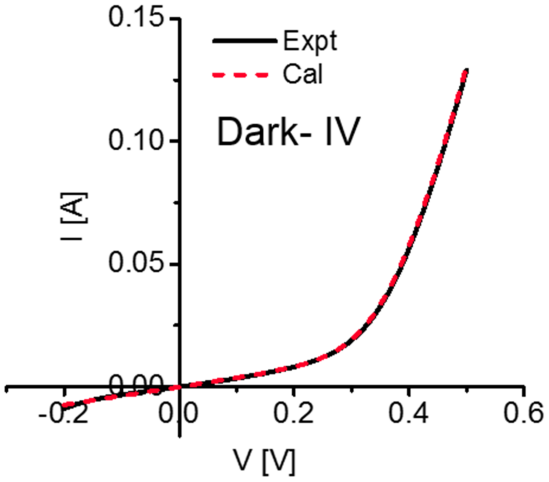

Fig. 7.10. Dark $I-V$ characteristics of the GaSb PV diode. The dark $I-V$ measurement is performed on a temperature-controlled stage ($25.2\pm 0.3\,^{\circ}$C) with 4 probes. The extracted PV parameters are: $I_0 = 9.4798 \times 10^{-6}$ A $n = 1.63134 \pm 0.005$ $R_s = 0.818864\ \Omega$ $R_{sh} = 26.52\ \Omega$

where n is the ideality factor and R_{sh} is the shunt resistance. The short-circuit current I_{SC} is calculated by multiplying the short-circuit current measured under 1 sun (AM1.5G) with the concentration factor C. Here, C is calculated as:

$$C' = \frac{\int d\lambda \Phi_{AM1.5D}(\lambda) EQE(\lambda) \tau_{PE}(\lambda) \tau_l(\lambda)}{\int d\lambda \Phi_{AM1.5G}(\lambda) EQE(\lambda)}, \tag{7.17}$$

where Φ is the photon flux of the solar spectrum and EQE is the external quantum efficiency spectrum of GaSb provided by the vendor (JX Crystal). The uncertainties in PV parameters and temperature measurements are also included in the V_{OC} modeling throughout this work.

7.3 Results and Discussions

The outdoor field test is performed on July 13th, 2018 at West Lafayette, IN. Throughout the outdoor test, the geometrical solar concentration C is about 37, excluding optical losses at the Fresnel lens and the LDPE (13 suns with losses included, 1 sun = 900 W/m^2 for AM1.5D). The real-time temperature T_{expt} and open-circuit voltage V_{OC} are plotted in Fig. 7.11 (a) and 7.11 (b), respectively. As shown in Fig. 7.11 (a), temperature of the cooling assembly in Chamber 1 (with soda-lime glass radiative cooler, solid green curve) is always lower than the cooling assembly in Chamber 2 (without soda-lime glass radiative cooler, solid red curve). The difference in temperature after reaching steady state is 10 °C. Given that the two testing chambers are almost identical, the reduction in temperature is mainly due to the radiative cooling from the soda-lime glass radiative cooler. The theoretical steady state temperature of the cooling assembly T_c is calculated using the model introduced in Section 7.2.2.

The model results, indicated by the dashed lines in Fig. 7.11 (a), show a good match with experiment. Important parameters used in the model are listed in Table 7.1. It should be noted that the effective convection coefficient h_{eff} for the two chambers are not supposed to be the same. The temperature of the cooling assembly in Chamber 2 is higher, leading to stronger convection [67]. An estimate following reference [67] shows that the h_{eff} of the Chamber 2 should be roughly 20% higher than that of Chamber 1. In our model, important quantities such as the net radiative cooling power density $I_{r,net}$ can be estimated by:

$$I_{r,net} = \frac{F[(P_r^{c,g} + P_r^{c,l}) - (P_a^{c,g} + P_a^{c,l})] - (P_{ds}^{g} + P_{ds}^{l})}{A_c}, \tag{7.18}$$

For Chamber 1, $I_{r,net}$ from soda-lime glass cooler is 63 W/m^2. Given the optical losses at the Fresnel lens and the LDPE, the estimated $I_{r,net}$ is comparable to reported values in prior works [206,208]. More importantly, about 43% of the total net cooling power,

$P_c + I_{r,net}A_c$, is contributed by radiative cooling. On the other hand, $I_{r,net}$ without radiative cooler (Chamber 2) is close to zero, as the absorbed diffuse horizontal solar irradiance cancels out the radiated power. Though the cooling assembly in Chamber 1 is 10 °C lower than the one in Chamber 2, its net radiative cooling power is much greater. Furthermore, radiative cooling in Chamber 1 plays a role as important as non-radiative cooling.

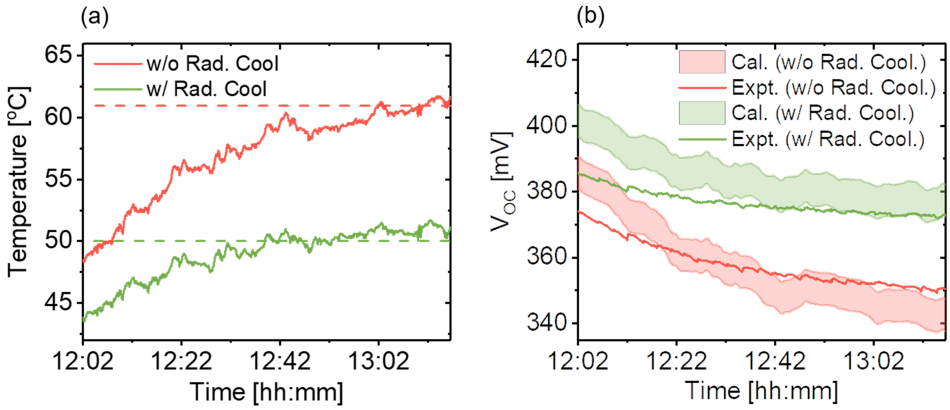

Fig. 7.11. Outdoor testing results on July 13th, 2018. (a) Real-time temperature reading with radiative cooling (green curve) and without radiative cooling (red curve). After about 1 hr of operation, radiative cooling induces a temperature reduction about 10 °C compared with the control sample. Steady state temperatures calculated using a steady state model are indicated by the dashed line in corresponding color. (b) Real-time V_{OC} measurement of the GaSb PV with radiative cooling (green curve) and without radiative cooling (red curve). The temperature reduction due to radiative cooling translates to an increase in V_{OC} of about 20 mV (5.7% relative increase). Theoretical predictions including experimental uncertainties (shaded regions) are plotted for comparison. A reasonable match within the error bars is achieved.

Modifying our experimentally-validated model to account for the key differences between our experimental system and a commercially-relevant high-concentration photovoltaic setup (specifically, increased non-radiative convection, higher concentration factors, and the need for a heat spreader), indicate that potential reduction of temperature in a commercial HCPV system with radiative cooling at 300 suns may

reach as high as 25 °C.

Real-time V_{OC} measurements are shown in Fig. 7.11 (b). Because of its lower operating temperature, the V_{OC} of the GaSb PV diode in Chamber 1 (with radiative cooler, solid green curve) is higher than the one in Chamber 2 (without radiative cooler, solid red curve). The absolute increase in V_{OC} is as large as 20 mV, which is equivalently a 5.7% relative increase. The theoretical V_{OC} at measured temperatures is calculated using the V_{OC} model introduced in Section 7.2.2. The results are plotted in Fig. 7.11 (b) for comparison. Uncertainties due to variations in temperature (T_{pv}) measurements and PV diode characterizations are indicated as the shaded regions. Overall, a reasonable match between experiment and theory is achieved, especially during the second half of the measurement. The discrepancy during the first half of the measurement may have resulted from the larger temperature gradient between the GaSb PV diode and the TC probe before reaching the steady state.

Table 7.1.
Comparison of theoretical steady-state temperatures and experimental results

Chamber	h_{eff} $\mathrm{W/(m^2\,K)}$	**Sky model**	T_c [°**C**]	T_{expt} [°**C**]
1	1.8	Mid-latitude summer	50	51
2	2.15	Mid-latitude summer	61	61

A separate outdoor field test has been performed on July 18th 2018. Fig. 7.12 shows the field test results. Similar to July 13th 2018 outdoor field test, a temperature reduction of 10 °C through radiative cooling is achieved. Such cooling effect translates to an increase of 20 mV in open-circuit voltage V_{OC}. This proves that the results are reproducible even when the environmental conditions are slightly different.

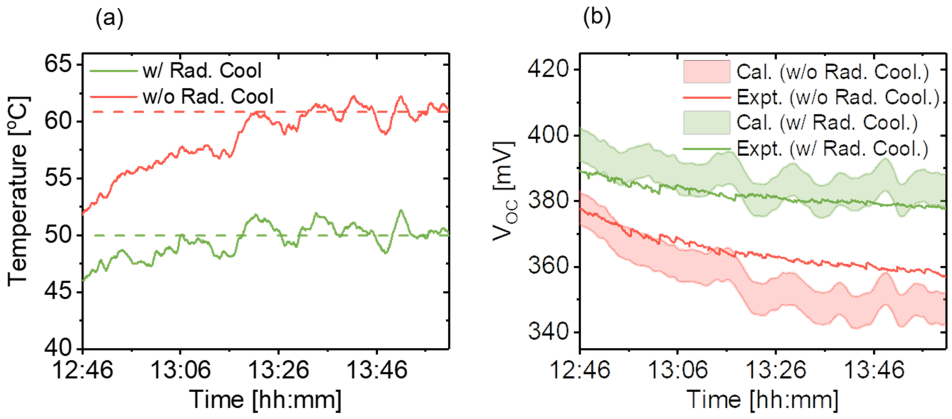

Fig. 7.12. Outdoor testing results on July 18th, 2018. (a) Real-time temperature reading with radiative cooling (green curve) and without radiative cooling (red curve). After about 1 hr of operation, temperature reduction similar to the July 13th results (about 10 °C) is achieved. Steady state temperatures calculated using a steady state model are indicated by the dashed line in corresponding color. (b) Real-time V_{OC} measurement of the GaSb PV with radiative cooling (green curve) and without radiative cooling (red curve). An increase in V_{OC} similar to the July 13th results (about 20 mV) is observed. Theoretical predictions including experimental uncertainties (shaded regions) are plotted for comparison. A reasonable match within the error bars is achieved.

The steady state temperature modeling is summarized in Table 7.2. It should be noted that the wind speed on July 18th is 60% higher than that on July 13th, which increases the convection coefficient by about 10%. Therefore, h_{eff} in Table 7.2 is slightly higher than the value in 7.1 (within 10% difference). The modeled temperature is plotted as dashed lines in Fig. 7.12 (a). The modeling results of V_{OC}, with uncertainties considered (same as the July 13th calculation), is shown in Fig. 7.12 (b) as shaded regions. A reasonable match between experiments and simulations is achieved. It should be noted that the temperature is noisier on July 18th due to the stronger wind. Such noise in temperature affects the calculation on V_{OC}. The measured V_{OC} is less noisy, indicating that the fluctuation in temperature measurements may be more affected by the environment.

Table 7.2.
Comparison of theoretical steady-state temperatures and experimental results

Chamber	h_{eff} $\mathrm{W/(m^2\,K)}$	**Sky model**	T_c [°C]	T_{expt} [°C]
1	1.9	Mid-latitude summer	50	50
2	2.2	Mid-latitude summer	61	61

In addition to instantaneous effects such as the increase in V_{OC}, long term benefits from radiative cooling including prolonged PV lifetime are equally if not more important. It has been shown that for certain temperature-induced failure modes (activation energy around 0.31 eV), every 20 °C reduction in operating temperature would increase PV lifetime by a factor of 2 [222]. Along the same lines, the 10 °C reduction in operating temperature demonstrated in this work could translate to a 40% increase in PV lifetime. For higher activation energy (0.89 eV) failure modes, the increase in PV lifetime could even approach 160% [87].

Yet greater improvements are expected under higher solar concentrations, even with the same system. For example, when C = 100 (35 suns after optical losses), our experimental setup could yield a temperature difference of 27 °C, translating to an increase of 77 mV in V_{OC} (34% relative). For certain high activation energy failure modes, the net effect can be a potential reduction in levelized cost of electricity (LCOE) of 33% for high-efficiency Si HIT cells [223]. Therefore, it is worthwhile to further explore radiative cooling as an important approach for higher performance, enhanced reliability and lower LCOE.

It is important to note that the demonstration in this work is not only limited to GaSb PV diode or one particular CPV configuration. It can be extended to many other outdoor optoelectronic systems, such as thermophotovoltaics, where thermal

management is critical for high-performance and good reliability. Possible configurations are depicted in Fig. 7.13. A CPV system with reflective concentrators, similar to the previously discussed CPV system in Fig. 7.1 is shown in Fig. 7.13 (a). It may share a similar radiative cooling configuration with transparent heat spreader [133, 224] and the cooler on the opposite side of the solar cell.

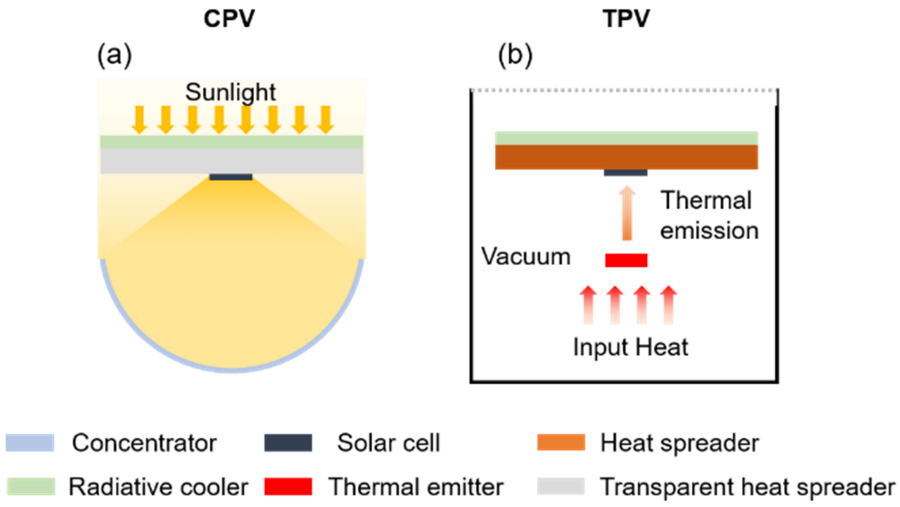

Fig. 7.13. Applications where radiative cooling can supplement the standard cooling capabilities of photovoltaics for improved performance and reliability. (a) A CPV with a reflective concentrator. The radiative cooler can be added to a heat spreader made of transparent conductive dielectric. (b) A thermophotovoltaic (TPV) system, where the radiative cooler is placed above a heat spreader, inside a vacuum chamber.

TPV systems operate differently, converting input heat into electricity via thermal radiation, which illuminates a low-bandgap photovoltaic cell [14,23]. As shown in Fig. 7.13 (b), the thermal emission from the thermal emitter is received by the PV cell. The total power received can be much greater than 1 sun. Furthermore, the vacuum enclosure that prevents non-radiative heat transfer between the emitter and the solar

cell also suppresses the cooling of the solar cell. In such cases, radiative cooling can be implemented by facing the radiative cooler towards the mid-IR transparent side of the chamber (indicated by the dashed line).

7.4 Conclusions

In this work, enhanced radiative cooling of low-bandgap PV diodes in a CPV system is demonstrated in outdoor field tests. Using a composite radiative cooler consisting of soda-lime glass and Al back reflector, a temperature reduction of 10 °C is achieved. The lowered operating temperature translates to a 20 mV absolute increase, or 5.7% relative increase, in V_{OC} from the PV diode. This is the first experimental demonstration of significantly enhanced V_{OC} under concentrated sunlight via enhanced radiative cooling. Furthermore, a substantial improvement in the PV reliability is estimated as a result of the reduction in operating temperature. Both the instantaneous and long-term performance is enhanced. The demonstration shows that radiative cooling can be an important thermal management strategy for outdoor optoelectronic systems, especially those with high heat loads and temperature sensitive performance. Implementing radiative cooling is straightforward in many cases. Such simplicity allows for potential use of a range of different radiative cooling materials. Furthermore, the prototype demonstrated in this work may pave the way for future use of radiative cooling in a wide range of electronic systems used in outdoor and/or space environments not only CPV and TPV systems, but also power electronics, satellites, and more.

8. CONCLUSION AND FUTURE WORK

In this thesis, selective thermal emitters and solar absorbers have been studied first. Photonic designs have been optimized to tailor thermal emission spectrum and enhance TPV/STPV efficiencies. To achieve a good balance among product scalability, mechanical versatility and high-temperature performance, a thin-film selective absorber/emitter has been fabricated and characterized using a customized direct thermal emittance measurement setup. On the system level, thermal management of the PV diode has been studied. The effect of radiative cooling has been investigated via numerical simulations, as well as outdoor experimental demonstrations. These contributions are summarized below.

- Chapter 2 addresses the challenge of suppressing sub-bandgap photon emissions from the thermal emitter. An integrated photonic crystal emitter (IPSE), consisting of a 2D W PhC and a 1D chirped multilayer filter, is proposed. Through numerical simulations, it is shown that the TPV efficiency can be as high as 41.8% at an emitter temperature of 1573 K when paired with a GaSb PV diode. In comparison, the efficiency for a bare 2D W PhC is only 35.2%. The physics of such performance improvement is discussed from the perspective of photon recycling. It is found that the integration of 1D chirped filter induces non-perturbative photon recycling, maximizing the recycled power.

- Chapter 3 addresses one main challenge of selective solar absorbers, which is achieving high thermal transfer efficiency at high temperature while solar concentration is low. This imposes the requirement of very strong spectral selectivity. To achieve that, an integrated photonic crystal selective absorber (IPSA) is proposed. It is a combination of a 2D W PhC and a 1D chirped rugate filter. The thermal transfer efficiency at 1500 K and 100 suns is estimated to be

65%, only 6.9% below the ideal absorber. Because IPSA and IPSE (discussed in Chapter 2) both have W as substrates, they can be combined into a monolithic absorber/emitter assembly. For an STPV system that operates at 1450 K and 100 suns, the assembly provides an STPV efficiency of 24.3%.

- Chapter 4 introduces an experimental setup built for high-temperature direct thermal emittance measurement. The setup is a critical characterization tool for selective thermal emitters and solar absorbers. It consists of a high-vacuum chamber where sample-under-test is heated to high temperature and an FTIR where thermal emission signal is collected. The optical path is carefully designed to ensure sufficient signal and low noise. A calibration procedure has been developed and proved to be consistent and robust. The method was applied to tilted-Ag/TiN nanopillar-based metamaterials and validated in experiment from $2-10$ μm.

- Chapter 5 addresses the challenge of making selective thermal emitters and solar absorbers that are scalable for manufacturing, mechanically flexible to cover various surfaces and high-performance at high operating temperatures. A thin-film Si-based selective absorber/emitter is fabricated and characterized at high temperature, using the setup introduced in Chapter 4. The fabrication process only involves standard wet etching and PVD, making it possible for large scale production. Furthermore, the absence of rigid substrate gives rise to strong mechanical flexibility. High-temperature characterization shows good spectral selectivity at 595 °C, resulting in a thermal transfer efficiency of 61% under 50 suns. Also, thermal stability at operating temperature is experimentally proved. Therefore, the thin-film Si-based absorber/emitter is a good balance of three aforementioned figures of merit, and is a strong candidate for real applications.

- Chapter 6 addresses the challenge of PV diode thermal management in a TPV system via radiative cooling. A cooling structure is proposed to enhance radiative sky cooling. The proposed radiative cooler is a 2D PhC made of low-iron

soda-lime glass. Through an opto-electro-thermal coupled simulation framework, it is found that radiative cooling can lower the PV temperature by as much as 91 K. Such cooling effect translates to a relative increase of 18% in TPV efficiency. Furthermore, it enhances the PV reliability by increasing its lifetime by 2200%.

- Chapter 7 demonstrates the cooling effect of enhanced radiative sky cooling on a CPV system. An outdoor testing setup is built. Soda-lime glass is used as the radiative cooler. For GaSb PV diodes under an effective solar concentration of 13 suns, a 10 °C temperature drop induced by radiative cooling is observed. Such cooling effect causes an unprecedented relative increase of 5.7% in open-circuit voltage. Furthermore, when the temperature induced degradation has an activation energy of 0.31 eV, the 10 °C temperature drop translates to a 40% increase in PV lifetime. Though the demonstration is on a CPV system, the similarity between the tested system and a TPV system makes it possible to extend the cooling strategy to an actual TPV system.

To summarize, the thesis studies selective thermal emitters and solar absorbers for TPV and STPV applications, as well as radiative cooling as a novel strategy of thermal management. The works explore photonic designs for optimized performance (TPV/STPV conversion efficiency and cooling effect) via numerical simulations on both component and system levels. They also experimentally demonstrate viable solutions that can be scaled up for production or generalized across various applications. While these works address challenges in TPV and STPV systems, future works are warranted to achieve better component-level performance and successful system integrations. Summarized below are some future works worth exploring:

- Based on the thin-film Si-based selective absorber/emitter demonstrated in Chapter 5, better performance may be achieved by material and design optimization. One of the primary focuses is the choice of materials for the back reflector. To improve high-temperature stability while maintaining strong broad-

band reflectivity, refractory metals like Mo and rhodium (Rh) are on top of the list. Another direction of improving selectivity at higher temperatures is exploring other thin-film semiconductors that have lower direct bandgap, so that strong above-bandgap absorption can be maintained while layer thickness is significantly reduced to suppress intrinsic carrier absorption. Of course, other factors including high-temperature thermal stability and the shift of cut-off wavelength due to bandgap narrowing should be considered as well. Finally, for applications like selective solar absorbers where broader absorption band can be beneficial, replacing the single-layer ARC with a carefully designed multilayer front coating [23] should improve the conversion efficiency. The absence of in-plane structure still ensures relatively simple fabrication process, and the mechanical flexibility can be preserved if the multilayer is thin.

- The outdoor testing of radiative cooling on CPV systems can be extended to higher solar concentrations (50 - 1000 suns), which is closer to actual industrial applications of HCPV. At such level of concentration, the cooling effect induced by enhanced sky radiative cooling is expected to be greater than the values reported in Chapter 7. As a result, the corresponding improvement in open-circuit voltage will be greater. Furthermore, new radiative coolers like porous low-iron soda-lime glass can be fabricated using sol-gel method [225]. Its near-ideal emittance in the atmospheric window can further improve the cooling effect of. While the demonstration is on a HCPV system, the cooling strategy can certainly be applied to other systems such as TPVs, due to the similarity of having high heat load and the using of low-bandgap PV diode.

- A demonstration of radiative-cooling-enabled TPV system is a critical step towards the development of an all-passive-cooling TPV. The demonstration requires a working TPV testing setup and the capability of switching radiative cooling on and off. As estimated theoretically, a cooling effect of 91 K temperature drop is expected from radiative cooling when the thermal emitter is at

1500 K, and the cooler (low-iron soda-lime glass) is 10 times larger than the PV diode (GaSb) [116]. Fundamentally speaking, a cooler PV diode can raise the efficiency limit (Carnot efficiency) at a given emitter temperature. For long term benefits, lower PV temperature can significantly enhance the reliability of both the PV diode and the TPV system as a whole. There are two ways to have access to sky radiative cooling. The first one is to build a portable TPV device that can operate in outdoor conditions [79]. The second is to simulate sky emission in lab. Basically, a blackbody heat sink can be placed in front of the radiative cooler and be cooled to an effective below-ambient sky temperature.

As a promising renewable energy technology, TPV is undergoing a rapid development thanks to the recent advance in nanophotonics and semiconductor device fabrications. Nonetheless, there are still many challenges to be addressed. While many researchers in TPV have primarily focused on system efficiency, the cost, scalability, and reliability may be equally if not more important factors to realize certain applications. Similarly, radiative cooling, with its unique mechanism, warrants further explorations to make it more effective for various applications. Though the research on radiative cooling started decades ago, its development and applications only started to grow substantially very recently owing to the use of new cooler designs and the ever-increasing demand for cooling. When combined together, the two technologies are complementary to each other. Radiative cooling offers a new path of cooling strategy for TPV system, and the high heat load of TPV system manifests the effect of radiative cooling.

REFERENCES

[1] *Estimated U.S. Energy Consumption in 2018.* Department of Energy and Lawrence Livermore National Laboratory, 2018.

[2] H. Kolm, "Solar-battery power source," *Quarterly Progress Report*, vol. 13, 1956.

[3] R. E. Nelson, "A brief history of thermophotovoltaic development," *Semiconductor Science and Technology*, vol. 18, no. 5, p. S141, 2003.

[4] T. Bauer, *Thermophotovoltaics: basic principles and critical aspects of system design.* Springer Science & Business Media, 2011.

[5] Y. X. Yeng, W. R. Chan, V. Rinnerbauer, J. D. Joannopoulos, M. Soljačić, and I. Celanovic, "Performance analysis of experimentally viable photonic crystal enhanced thermophotovoltaic systems," *Optics Express*, vol. 21, no. 106, pp. A1035–A1051, 2013.

[6] Z. Zhou, Q. Chen, and P. Bermel, "Prospects for high-performance thermophotovoltaic conversion efficiencies exceeding the Shockley–Queisser limit," *Energy Conversion and Management*, vol. 97, pp. 63–69, 2015.

[7] N.-P. Harder and P. Würfel, "Theoretical limits of thermophotovoltaic solar energy conversion," *Semiconductor Science and Technology*, vol. 18, no. 5, p. S151, 2003.

[8] Z. Omair, G. Scranton, L. M. Pazos-Outón, T. P. Xiao, M. A. Steiner, V. Ganapati, P. F. Peterson, J. Holzrichter, H. Atwater, and E. Yablonovitch, "Ultra-efficient thermophotovoltaic power conversion by band-edge spectral filtering," *Proceedings of the National Academy of Sciences*, vol. 116, no. 31, pp. 15 356–15 361, 2019.

[9] D. M. Bierman, A. Lenert, W. R. Chan, B. Bhatia, I. Celanović, M. Soljačić, and E. N. Wang, "Enhanced photovoltaic energy conversion using thermally based spectral shaping," *Nature Energy*, vol. 1, no. 6, p. 16068, 2016.

[10] D. G. Baranov, Y. Xiao, I. A. Nechepurenko, A. Krasnok, A. Alù, and M. A. Kats, "Nanophotonic engineering of far-field thermal emitters," *Nature Materials*, p. 1, 2019.

[11] E. Rephaeli and S. Fan, "Absorber and emitter for solar thermo-photovoltaic systems to achieve efficiency exceeding the Shockley-Queisser limit," *Optics Express*, vol. 17, no. 17, pp. 15 145–15 159, 2009.

[12] G. E. Guazzoni, "High-temperature spectral emittance of oxides of erbium, samarium, neodymium and ytterbium," *Applied Spectroscopy*, vol. 26, no. 1, pp. 60–65, 1972.

[13] B. Bitnar, W. Durisch, J.-C. Mayor, H. Sigg, and H. Tschudi, "Characterisation of rare earth selective emitters for thermophotovoltaic applications," *Solar Energy Materials and Solar Cells*, vol. 73, no. 3, pp. 221–234, 2002.

[14] B. Bitnar, W. Durisch, and R. Holzner, "Thermophotovoltaics on the move to applications," *Applied Energy*, vol. 105, pp. 430–438, 2013.

[15] W. Tobler and W. Durisch, "Plasma-spray coated rare-earth oxides on molybdenum disilicide–high temperature stable emitters for thermophotovoltaics," *Applied Energy*, vol. 85, no. 5, pp. 371–383, 2008.

[16] E. Sakr, Z. Zhou, and P. Bermel, "High efficiency rare-earth emitter for thermophotovoltaic applications," *Applied Physics Letters*, vol. 105, no. 11, p. 111107, 2014.

[17] D. L. Chubb, A. T. Pal, M. O. Patton, and P. P. Jenkins, "Rare earth doped high temperature ceramic selective emitters," *Journal of the European Ceramic Society*, vol. 19, no. 13-14, pp. 2551–2562, 1999.

[18] M. R. Khan, X. Wang, E. Sakr, M. A. Alam, and P. Bermel, "Enhanced selective thermal emission with a meta-mirror following generalized Snells law," *MRS Online Proceedings Library Archive*, vol. 1728, 2015.

[19] N. Yu, P. Genevet, M. A. Kats, F. Aieta, J.-P. Tetienne, F. Capasso, and Z. Gaburro, "Light propagation with phase discontinuities: generalized laws of reflection and refraction," *Science*, vol. 334, no. 6054, pp. 333–337, 2011.

[20] Y. X. Yeng, M. Ghebrebrhan, P. Bermel, W. R. Chan, J. D. Joannopoulos, M. Soljačić, and I. Celanovic, "Enabling high-temperature nanophotonics for energy applications," *Proceedings of the National Academy of Sciences*, vol. 109, no. 7, pp. 2280–2285, 2012.

[21] M. Ghebrebrhan, P. Bermel, Y. X. Yeng, I. Celanovic, M. Soljačić, and J. Joannopoulos, "Tailoring thermal emission via Q matching of photonic crystal resonances," *Physical Review A*, vol. 83, no. 3, p. 033810, 2011.

[22] Y. Nam, Y. X. Yeng, A. Lenert, P. Bermel, I. Celanovic, M. Soljačić, and E. N. Wang, "Solar thermophotovoltaic energy conversion systems with two-dimensional tantalum photonic crystal absorbers and emitters," *Solar Energy Materials and Solar Cells*, vol. 122, pp. 287–296, 2014.

[23] P. Bermel, M. Ghebrebrhan, W. Chan, Y. X. Yeng, M. Araghchini, R. Hamam, C. H. Marton, K. F. Jensen, M. Soljačić, J. D. Joannopoulos *et al.*, "Design and global optimization of high-efficiency thermophotovoltaic systems," *Optics Express*, vol. 18, no. 103, pp. A314–A334, 2010.

[24] I. Celanovic, N. Jovanovic, and J. Kassakian, "Two-dimensional tungsten photonic crystals as selective thermal emitters," *Applied Physics Letters*, vol. 92, no. 19, p. 193101, 2008.

[25] J. Fleming, S. Lin, I. El-Kady, R. Biswas, and K. Ho, "All-metallic three-dimensional photonic crystals with a large infrared bandgap," *Nature*, vol. 417, no. 6884, p. 52, 2002.

[26] X. Liu, T. Tyler, T. Starr, A. F. Starr, N. M. Jokerst, and W. J. Padilla, "Taming the blackbody with infrared metamaterials as selective thermal emitters," *Physical Review Letters*, vol. 107, no. 4, p. 045901, 2011.

[27] C. Wu, B. Neuner III, J. John, A. Milder, B. Zollars, S. Savoy, and G. Shvets, "Metamaterial-based integrated plasmonic absorber/emitter for solar thermophotovoltaic systems," *Journal of Optics*, vol. 14, no. 2, p. 024005, 2012.

[28] J. Liu, U. Guler, W. Li, A. V. Kildishev, A. Boltasseva, and V. M. Shalaev, "High-temperature plasmonic thermal emitter for thermo-photovoltaics," in *2014 Conference on Lasers and Electro-Optics (CLEO)-Laser Science to Photonic Applications*. IEEE, 2014, pp. 1–2.

[29] M. Garín, D. Hernandez, T. Trifonov, and R. Alcubilla, "Three-dimensional metallo-dielectric selective thermal emitters with high-temperature stability for thermophotovoltaic applications," *Solar Energy Materials and Solar Cells*, vol. 134, pp. 22–28, 2015.

[30] P. Nagpal, D. P. Josephson, N. R. Denny, J. DeWilde, D. J. Norris, and A. Stein, "Fabrication of carbon/refractory metal nanocomposites as thermally stable metallic photonic crystals," *Journal of Materials Chemistry*, vol. 21, no. 29, pp. 10 836–10 843, 2011.

[31] M. Chirumamilla, G. V. Krishnamurthy, K. Knopp, T. Krekeler, M. Graf, D. Jalas, M. Ritter, M. Störmer, A. Y. Petrov, and M. Eich, "Metamaterial emitter for thermophotovoltaics stable up to 1400 c," *Scientific Reports*, vol. 9, no. 1, p. 7241, 2019.

[32] G. B. Rybicki and A. P. Lightman, *Radiative processes in astrophysics*. John Wiley & Sons, Weinheim, 2008.

[33] V. Rinnerbauer, A. Lenert, D. M. Bierman, Y. X. Yeng, W. R. Chan, R. D. Geil, J. J. Senkevich, J. D. Joannopoulos, E. N. Wang, M. Soljačić *et al.*, "Metallic photonic crystal absorber-emitter for efficient spectral control in high-temperature solar thermophotovoltaics," *Advanced Energy Materials*, vol. 4, no. 12, p. 1400334, 2014.

[34] V. Stelmakh, V. Rinnerbauer, W. R. Chan, J. J. Senkevich, J. D. Joannopoulos, M. Soljačić, and I. Celanovic, "Performance of tantalum-tungsten alloy selective emitters in thermophotovoltaic systems," in *Energy Harvesting and Storage: Materials, Devices, and Applications V*, vol. 9115. International Society for Optics and Photonics, 2014, p. 911504.

[35] H.-J. Lee, K. Smyth, S. Bathurst, J. Chou, M. Ghebrebrhan, J. Joannopoulos, N. Saka, and S.-G. Kim, "Hafnia-plugged microcavities for thermal stability of selective emitters," *Applied Physics Letters*, vol. 102, no. 24, p. 241904, 2013.

[36] H. Sai, Y. Kanamori, and H. Yugami, "High-temperature resistive surface grating for spectral control of thermal radiation," *Applied Physics Letters*, vol. 82, no. 11, pp. 1685–1687, 2003.

[37] C. Schlemmer, J. Aschaber, V. Boerner, and J. Luther, "Thermal stability of micro-structured selective tungsten emitters," in *AIP Conference Proceedings*, vol. 653, no. 1. AIP, 2003, pp. 164–173.

[38] D. Peykov, Y. X. Yeng, I. Celanovic, J. D. Joannopoulos, and C. A. Schuh, "Effects of surface diffusion on high temperature selective emitters," *Optics Express*, vol. 23, no. 8, pp. 9979–9993, 2015.

[39] W. W. Mullins, "Flattening of a nearly plane solid surface due to capillarity," *Journal of Applied Physics*, vol. 30, no. 1, pp. 77–83, 1959.

[40] K. A. Arpin, M. D. Losego, and P. V. Braun, "Electrodeposited 3D tungsten photonic crystals with enhanced thermal stability," *Chemistry of Materials*, vol. 23, no. 21, pp. 4783–4788, 2011.

[41] K. A. Arpin, M. D. Losego, A. N. Cloud, H. Ning, J. Mallek, N. P. Sergeant, L. Zhu, Z. Yu, B. Kalanyan, G. N. Parsons *et al.*, "Three-dimensional self-assembled photonic crystals with high temperature stability for thermal emission modification," *Nature Communications*, vol. 4, p. 2630, 2013.

[42] W. Li, U. Guler, N. Kinsey, G. V. Naik, A. Boltasseva, J. Guan, V. M. Shalaev, and A. V. Kildishev, "Refractory plasmonics with titanium nitride: broadband metamaterial absorber," *Advanced Materials*, vol. 26, no. 47, pp. 7959–7965, 2014.

[43] Q.-C. Zhang and D. R. Mills, "Very low-emittance solar selective surfaces using new film structures," *Journal of Applied Physics*, vol. 72, no. 7, pp. 3013–3021, 1992.

[44] Q.-C. Zhang, "High efficiency Al-N cermet solar coatings with double cermet layer film structures," *Journal of Physics D: Applied Physics*, vol. 32, no. 15, p. 1938, 1999.

[45] P. Gao, L. Meng, M. Dos Santos, V. Teixeira, and M. Andritschky, "Study of ZrO2-Y2O3 films prepared by RF magnetron reactive sputtering," *Thin Solid Films*, vol. 377, pp. 32–36, 2000.

[46] C. Arancibia-Bulnes, C. Estrada, and J. Ruiz-Suárez, "Solar absorptance and thermal emittance of cermets with large particles," *Journal of Physics D: Applied Physics*, vol. 33, no. 19, p. 2489, 2000.

[47] C. E. Kennedy, "Review of mid-to high-temperature solar selective absorber materials," National Renewable Energy Lab., Golden, CO.(US), Tech. Rep. TP-520-31267, 2002.

[48] D. Chester, P. Bermel, J. D. Joannopoulos, M. Soljacic, and I. Celanovic, "Design and global optimization of high-efficiency solar thermal systems with tungsten cermets," *Optics Express*, vol. 19, no. 103, pp. A245–A257, 2011.

[49] R. Messier, S. Krishnaswamy, L. Gilbert, and P. Swab, "Black a-Si solar selective absorber surfaces," *Journal of Applied Physics*, vol. 51, no. 3, pp. 1611–1614, 1980.

[50] B. Seraphin, "Chemical vapor deposition of thin semiconductor films for solar energy conversion," *Thin Solid Films*, vol. 39, pp. 87–94, 1976.

[51] L. Gilbert, R. Messier, and R. Roy, "Black germanium solar selective absorber surfaces," *Thin Solid Films*, vol. 54, no. 2, pp. 149–157, 1978.

[52] D. Mattox and G. Kominiak, "Deposition of semiconductor films with high solar absorptivity," *Journal of Vacuum Science and Technology*, vol. 12, no. 1, pp. 182–185, 1975.

[53] H. Tian, Z. Zhou, T. Liu, C. Karina, U. Guler, V. Shalaev, and P. Bermel, "High temperature efficient, stable Si wafer-based selective solar absorbers," *Applied Physics Letters*, vol. 110, no. 14, p. 141101, 2017.

[54] N. P. Sergeant, O. Pincon, M. Agrawal, and P. Peumans, "Design of wide-angle solar-selective absorbers using aperiodic metal-dielectric stacks," *Optics Express*, vol. 17, no. 25, pp. 22 800–22 812, 2009.

[55] N. P. Sergeant, M. Agrawal, and P. Peumans, "High performance solar-selective absorbers using coated sub-wavelength gratings," *Optics Express*, vol. 18, no. 6, pp. 5525–5540, 2010.

[56] Z. Zhou, E. Sakr, O. Yehia, A. Mathur, and P. Bermel, "Photonic crystal selective structures for solar thermophotovoltaics," *MRS Advances*, vol. 1, no. 59, pp. 3883–3889, 2016.

[57] V. Rinnerbauer, E. Lausecker, F. Schäffler, P. Reininger, G. Strasser, R. Geil, J. Joannopoulos, M. Soljačić, and I. Celanovic, "Nanoimprinted superlattice metallic photonic crystal as ultraselective solar absorber," *Optica*, vol. 2, no. 8, pp. 743–746, 2015.

[58] B. Bitnar, W. Durisch, D. Grutzmacher, J.-C. Mayor, C. Muller, F. von Roth, J. A. Selvan, H. Sigg, H. R. Tschudi, and J. Gobrecht, "A TPV system with silicon photocells and a selective emitter," in *Conference Record of the Twenty-Eighth IEEE Photovoltaic Specialists Conference-2000 (Cat. No. 00CH37036)*. IEEE, 2000, pp. 1218–1221.

[59] M. Tan, L. Ji, Y. Wu, P. Dai, Q. Wang, K. Li, T. Yu, Y. Yu, S. Lu, and H. Yang, "Investigation of InGaAs thermophotovoltaic cells under blackbody radiation," *Applied Physics Express*, vol. 7, no. 9, p. 096601, 2014.

[60] J. van der Heide, N. Posthuma, G. Flamand, W. Geens, and J. Poortmans, "Cost-efficient thermophotovoltaic cells based on germanium substrates," *Solar Energy Materials and Solar Cells*, vol. 93, no. 10, pp. 1810–1816, 2009.

[61] A. Bett and O. Sulima, "GaSb photovoltaic cells for applications in TPV generators," *Semiconductor Science and Technology*, vol. 18, no. 5, p. S184, 2003.

[62] V. Andreev, S. Sorokina, N. K. Timoshina, V. Khvostikov, and M. Shvarts, "Solar cells based on gallium antimonide," *Semiconductors*, vol. 43, no. 5, pp. 668–671, 2009.

[63] L. M. Fraas, *Low-cost solar electric power*. Springer, Cham, 2014.

[64] R. Tuley, J. Orr, R. Nicholas, D. Rogers, P. Cannard, and S. Dosanjh, "Lattice-matched InGaAs on InP thermophovoltaic cells," *Semiconductor Science and Technology*, vol. 28, no. 1, p. 015013, 2012.

[65] R. Wehrer, M. Wanlass, D. Wilt, B. Wernsman, R. Siergiej, and J. Carapella, "InGaAs series-connected, tandem, MIM TPV converters," in *3rd World Conference onPhotovoltaic Energy Conversion, 2003. Proceedings of*, vol. 1. IEEE, 2003, pp. 892–895.

[66] A. Lenert, D. M. Bierman, Y. Nam, W. R. Chan, I. Celanović, M. Soljačić, and E. N. Wang, "A nanophotonic solar thermophotovoltaic device," *Nature Nanotechnology*, vol. 9, no. 2, p. 126, 2014.

[67] F. P. Incropera and D. P. DeWitt, *Fundamentals of heat and mass transfer*. Wiley & Sons, New York, 1981.

[68] S. Catalanotti, V. Cuomo, G. Piro, D. Ruggi, V. Silvestrini, and G. Troise, "The radiative cooling of selective surfaces," *Solar Energy*, vol. 17, no. 2, pp. 83–89, 1975.

[69] C. Granqvist and A. Hjortsberg, "Radiative cooling to low temperatures: General considerations and application to selectively emitting SiO films," *Journal of Applied Physics*, vol. 52, no. 6, pp. 4205–4220, 1981.

[70] R. A. Craig, *The upper atmosphere: meteorology and physics*. Academic Press, New York, 2016.

[71] M. N. Bahadori, "Passive cooling systems in Iranian architecture," *Scientific American*, vol. 238, no. 2, pp. 144–155, 1978.

[72] F. Trombe, "Perspectives sur lutilisation des rayonnements solaires et terrestres dans certaines régions du monde," *Rev. Gen. Therm*, vol. 6, no. 70, p. 1285, 1967.

[73] B. Bartoli, S. Catalanotti, B. Coluzzi, V. Cuomo, V. Silvestrini, and G. Troise, "Nocturnal and diurnal performances of selective radiators," *Applied Energy*, vol. 3, no. 4, pp. 267–286, 1977.

[74] T. M. Nilsson, G. A. Niklasson, and C. G. Granqvist, "A solar reflecting material for radiative cooling applications: ZnS pigmented polyethylene," *Solar Energy materials and Solar cells*, vol. 28, no. 2, pp. 175–193, 1992.

[75] B. Orel, M. K. Gunde, and A. Krainer, "Radiative cooling efficiency of white pigmented paints," *Solar Energy*, vol. 50, no. 6, pp. 477–482, 1993.

[76] T. M. Nilsson and G. A. Niklasson, "Radiative cooling during the day: simulations and experiments on pigmented polyethylene cover foils," *Solar Energy Materials and Solar Cells*, vol. 37, no. 1, pp. 93–118, 1995.

[77] C. Granqvist, A. Hjortsberg, and T. Eriksson, "Radiative cooling to low temperatures with selectivity ir-emitting surfaces," *Thin Solid Films*, vol. 90, no. 2, pp. 187–190, 1982.

[78] C. Granqvist and A. Hjortsberg, "Surfaces for radiative cooling: Silicon monoxide films on aluminum," *Applied Physics Letters*, vol. 36, no. 2, pp. 139–141, 1980.

[79] W. R. Chan, P. Bermel, R. C. Pilawa-Podgurski, C. H. Marton, K. F. Jensen, J. J. Senkevich, J. D. Joannopoulos, M. Soljačić, and I. Celanovic, "Toward high-energy-density, high-efficiency, and moderate-temperature chip-scale thermophotovoltaics," *Proceedings of the National Academy of Sciences*, vol. 110, no. 14, pp. 5309–5314, 2013.

[80] J. D. Joannopoulos, S. G. Johnson, J. N. Winn, and R. D. Meade, *Photonic crystals: molding the flow of light*. Princeton University Press, Princeton, New Jersey, 2011.

[81] E. Rephaeli, A. Raman, and S. Fan, "Ultrabroadband photonic structures to achieve high-performance daytime radiative cooling," *Nano Letters*, vol. 13, no. 4, pp. 1457–1461, 2013.

[82] A. P. Raman, M. A. Anoma, L. Zhu, E. Rephaeli, and S. Fan, "Passive radiative cooling below ambient air temperature under direct sunlight," *Nature*, vol. 515, no. 7528, p. 540, 2014.

[83] L. Zhu, A. Raman, K. X. Wang, M. A. Anoma, and S. Fan, "Radiative cooling of solar cells," *Optica*, vol. 1, no. 1, pp. 32–38, 2014.

[84] L. Zhu, A. P. Raman, and S. Fan, "Radiative cooling of solar absorbers using a visibly transparent photonic crystal thermal blackbody," *Proceedings of the National Academy of Sciences*, vol. 112, no. 40, pp. 12 282–12 287, 2015.

[85] S.-H. Wu and M. L. Povinelli, "Solar heating of GaAs nanowire solar cells," *Optics Express*, vol. 23, no. 24, pp. A1363–A1372, 2015.

[86] T. S. Safi and J. N. Munday, "Improving photovoltaic performance through radiative cooling in both terrestrial and extraterrestrial environments," *Optics Express*, vol. 23, no. 19, pp. A1120–A1128, 2015.

[87] X. Sun, T. J. Silverman, Z. Zhou, M. R. Khan, P. Bermel, and M. A. Alam, "Optics-based approach to thermal management of photovoltaics: selective-spectral and radiative cooling," *IEEE Journal of Photovoltaics*, vol. 7, no. 2, pp. 566–574, 2017.

[88] M. Francoeur, R. Vaillon, and M. Mengüç, "Performance analysis of nanoscale-gap thermophotovolatic energy conversion devices," in *International symposium on Thermal and Materials Nanoscience and Nanotechnology (TMNN-2011)*, 2011.

[89] D. Fixsen, "The temperature of the cosmic microwave background," *The Astrophysical Journal*, vol. 707, no. 2, p. 916, 2009.

[90] W. B. Grant, "Water vapor absorption coefficients in the 8–13-μm spectral region: a critical review," *Applied Optics*, vol. 29, no. 4, pp. 451–462, 1990.

[91] S. B. Idso and R. D. Jackson, "Thermal radiation from the atmosphere," *Journal of Geophysical Research*, vol. 74, no. 23, pp. 5397–5403, 1969.

[92] E. E. Bell, L. Eisner, J. Young, and R. A. Oetjen, "Spectral radiance of sky and terrain at wavelengths between 1 and 20 microns. ii. sky measurements," *Journal of Optical Society of America*, vol. 50, no. 12, pp. 1313–1320, 1960.

[93] R. McGee, "An analytical infrared radiation model of the earth," *Applied Optics*, vol. 1, no. 5, pp. 649–653, 1962.

[94] R. E. Roberts, J. E. Selby, and L. M. Biberman, "Infrared continuum absorption by atmospheric water vapor in the 8–12-μm window," *Applied Optics*, vol. 15, no. 9, pp. 2085–2090, 1976.

[95] S. B. Idso, "A set of equations for full spectrum and 8-to 14-μm and 10.5-to 12.5-μm thermal radiation from cloudless skies," *Water Resources Research*, vol. 17, no. 2, pp. 295–304, 1981.

[96] K. I. Strabala, S. A. Ackerman, and W. P. Menzel, "Cloud properties inferred from 8–12-μm data," *Journal of Applied Meteorology*, vol. 33, no. 2, pp. 212–229, 1994.

[97] P. Berdahl, M. Martin, and F. Sakkal, "Thermal performance of radiative cooling panels," *International Journal of Heat and Mass Transfer*, vol. 26, no. 6, pp. 871–880, 1983.

[98] J. Garratt and R. Brost, "Radiative cooling effects within and above the nocturnal boundary layer," *Journal of the Atmospheric Sciences*, vol. 38, no. 12, pp. 2730–2746, 1981.

[99] U. Eicker and A. Dalibard, "Photovoltaic-thermal collectors for night radiative cooling of buildings," *Solar Energy*, vol. 85, no. 7, pp. 1322–1335, 2011.

[100] N. Artmann, H. Manz, and P. Heiselberg, "Parameter study on performance of building cooling by night-time ventilation," *Renewable Energy*, vol. 33, no. 12, pp. 2589–2598, 2008.

[101] A. Holtslag and H. De Bruin, "Applied modeling of the nighttime surface energy balance over land," *Journal of Applied Meteorology*, vol. 27, no. 6, pp. 689–704, 1988.

[102] Z. Chen, L. Zhu, A. Raman, and S. Fan, "Radiative cooling to deep sub-freezing temperatures through a 24-h day-night cycle," *Nature Communications*, vol. 7, p. 13729, 2016.

[103] K. Nishioka, Y. Ota, K. Tamura, and K. Araki, "Heat reduction of concentrator photovoltaic module using high radiation coating," *Surface and Coatings Technology*, vol. 215, pp. 472–475, 2013.

[104] A. Harrison and M. Walton, "Radiative cooling of tio2 white paint," *Solar Energy*, vol. 20, no. 2, pp. 185–188, 1978.

[105] P. Grenier, "Réfrigération radiative. effet de serre inverse," *Revue de Physique Appliquee*, vol. 14, no. 1, pp. 87–90, 1979.

[106] B. Landro and P. McCormick, "Effect of surface characteristics and atmospheric conditions on radiative heat loss to a clear sky," *International Journal of Heat and Mass Transfer*, vol. 23, no. 5, pp. 613–620, 1980.

[107] A. Addeo, L. Nicolais, G. Romeo, B. Bartoli, B. Coluzzi, and V. Silvestrini, "Light selective structures for large scale natural air conditioning," *Solar Energy*, vol. 24, no. 1, pp. 93–98, 1980.

[108] T. Eriksson and C. G. Granqvist, "Infrared optical properties of electron-beam evaporated silicon oxynitride films," *Applied Optics*, vol. 22, no. 20, pp. 3204–3206, 1983.

[109] T. Eriksson, E. Lushiku, and C. Granqvist, "Materials for radiative cooling to low temperature," *Solar Energy Materials*, vol. 11, no. 3, pp. 149–161, 1984.

[110] T. Eriksson and C. Granqvist, "Infrared optical properties of silicon oxynitride films: experimental data and theoretical interpretation," *Journal of Applied Physics*, vol. 60, no. 6, pp. 2081–2091, 1986.

[111] A. Hjortsberg and C. Granqvist, "Radiative cooling with selectively emitting ethylene gas," *Applied Physics Letters*, vol. 39, no. 6, pp. 507–509, 1981.

[112] E. Lushiku, A. Hjortsberg, and C. Granqvist, "Radiative cooling with selectively infrared-emitting ammonia gas," *Journal of Applied Physics*, vol. 53, no. 8, pp. 5526–5530, 1982.

[113] C. N. Suryawanshi and C.-T. Lin, "Radiative cooling: lattice quantization and surface emissivity in thin coatings," *ACS Applied Materials & Interfaces*, vol. 1, no. 6, pp. 1334–1338, 2009.

[114] A. R. Gentle and G. B. Smith, "Radiative heat pumping from the earth using surface phonon resonant nanoparticles," *Nano Letters*, vol. 10, no. 2, pp. 373–379, 2010.

[115] L. Zhu, A. Raman, and S. Fan, "Color-preserving daytime radiative cooling," *Applied Physics Letters*, vol. 103, no. 22, p. 223902, 2013.

[116] Z. Zhou, X. Sun, and P. Bermel, "Radiative cooling for thermophotovoltaic systems," in *Infrared Remote Sensing and Instrumentation XXIV*, vol. 9973. International Society for Optics and Photonics, 2016, p. 997308.

[117] A. R. Gentle and G. B. Smith, "A subambient open roof surface under the mid-summer sun," *Advanced Science*, vol. 2, no. 9, p. 1500119, 2015.

[118] E. Taft, "Characterization of silicon nitride films," *Journal of the Electrochemical Society*, vol. 118, no. 8, pp. 1341–1346, 1971.

[119] W. Pliskin, "Comparison of properties of dielectric films deposited by various methods," *Journal of Vacuum Science and Technology*, vol. 14, no. 5, pp. 1064–1081, 1977.

[120] A. Gentle and G. Smith, "Is enhanced radiative cooling of solar cell modules worth pursuing?" *Solar Energy Materials and Solar Cells*, vol. 150, pp. 39–42, 2016.

[121] T. Li, Y. Zhai, S. He, W. Gan, Z. Wei, M. Heidarinejad, D. Dalgo, R. Mi, X. Zhao, J. Song *et al.*, "A radiative cooling structural material," *Science*, vol. 364, no. 6442, pp. 760–763, 2019.

[122] C. Granqvist and A. Hjortsberg, "A letter to the editor," *Solar Energy*, vol. 24, p. 216, 1980.

[123] J. Mandal, Y. Fu, A. C. Overvig, M. Jia, K. Sun, N. N. Shi, H. Zhou, X. Xiao, N. Yu, and Y. Yang, "Hierarchically porous polymer coatings for highly efficient passive daytime radiative cooling," *Science*, vol. 362, no. 6412, pp. 315–319, 2018.

[124] G. B. Smith, "Commentary: Environmental nanophotonics and energy," *Journal of Nanophotonics*, vol. 5, no. 1, p. 050301, 2011.

[125] P. Bermel, C. Luo, L. Zeng, L. C. Kimerling, and J. D. Joannopoulos, "Improving thin-film crystalline silicon solar cell efficiencies with photonic crystals," *Optics Express*, vol. 15, no. 25, pp. 16 986–17 000, 2007.

[126] T. Eriksson, A. Hjortsberg, and C. Granqvist, "Solar absorptance and thermal emittance of Al2O3 films on Al: a theoretical assessment," *Solar Energy Materials*, vol. 6, no. 2, pp. 191–199, 1982.

[127] R. Santbergen and R. C. van Zolingen, "The absorption factor of crystalline silicon PV cells: A numerical and experimental study," *Solar Energy Materials and Solar Cells*, vol. 92, no. 4, pp. 432–444, 2008.

[128] Z. C. Holman, M. Filipič, B. Lipovšek, S. De Wolf, F. Smole, M. Topič, and C. Ballif, "Parasitic absorption in the rear reflector of a silicon solar cell: Simulation and measurement of the sub-bandgap reflectance for common dielectric/metal reflectors," *Solar Energy Materials and Solar Cells*, vol. 120, pp. 426–430, 2014.

[129] P. Bermel, R. Asadpour, C. Zhou, and M. A. Alam, "A modeling framework for potential induced degradation in PV modules," in *Reliability of Photovoltaic Cells, Modules, Components, and Systems VIII*, vol. 9563. International Society for Optics and Photonics, 2015, p. 95630C.

[130] R. Asadpour, R. V. K. Chavali, and M. A. Alam, "Physics-based computational modeling of moisture ingress in solar modules: location-specific corrosion and delamination," in *2016 IEEE 43rd Photovoltaic Specialists Conference (PVSC)*. IEEE, 2016, pp. 0840–0843.

[131] W. Li, Y. Shi, K. Chen, L. Zhu, and S. Fan, "A comprehensive photonic approach for solar cell cooling," *ACS Photonics*, vol. 4, no. 4, pp. 774–782, 2017.

[132] A. Royne, C. J. Dey, and D. R. Mills, "Cooling of photovoltaic cells under concentrated illumination: a critical review," *Solar Energy Materials and Solar Cells*, vol. 86, no. 4, pp. 451–483, 2005.

[133] Y. Sun, Z. Zhou, X. Jin, X. Sun, M. A. Alam, and P. Bermel, "Radiative cooling for concentrating photovoltaic systems," in *Thermal Radiation Management for Energy Applications*, vol. 10369. International Society for Optics and Photonics, 2017, p. 103690D.

[134] S. A. Maier, *Plasmonics: fundamentals and applications*. Springer Science & Business Media, New York, 2007.

[135] W. Cai and V. Shalaev, *Optical metamaterials: fundamentals and applications*. Springer Science & Business Media, New York, 2009.

[136] U. Guler, A. Boltasseva, and V. M. Shalaev, "Refractory plasmonics," *Science*, vol. 344, no. 6181, pp. 263–264, 2014.

[137] H. Sai and H. Yugami, "Thermophotovoltaic generation with selective radiators based on tungsten surface gratings," *Applied Physics Letters*, vol. 85, no. 16, pp. 3399–3401, 2004.

[138] I. Celanovic, D. Perreault, and J. Kassakian, "Resonant-cavity enhanced thermal emission," *Physical Review B*, vol. 72, no. 7, p. 075127, 2005.

[139] D. L. Chan, I. Celanovic, J. Joannopoulos, and M. Soljačić, "Emulating one-dimensional resonant Q-matching behavior in a two-dimensional system via fano resonances," *Physical Review A*, vol. 74, no. 6, p. 064901, 2006.

[140] S. John and R. Wang, "Metallic photonic-band-gap filament architectures for optimized incandescent lighting," *Physical Review A*, vol. 78, no. 4, p. 043809, 2008.

[141] J. M. Gee, J. B. Moreno, S.-Y. Lin, and J. G. Fleming, "Selective emitters using photonic crystals for thermophotovoltaic energy conversion," in *Photovoltaic Specialists Conference, 2002. Conference Record of the Twenty-Ninth IEEE.* IEEE, 2002, pp. 896–899.

[142] M. Florescu, H. Lee, I. Puscasu, M. Pralle, L. Florescu, D. Z. Ting, and J. P. Dowling, "Improving solar cell efficiency using photonic band-gap materials," *Solar Energy Materials and Solar Cells*, vol. 91, no. 17, pp. 1599–1610, 2007.

[143] V. Rinnerbauer, S. Ndao, Y. X. Yeng, W. R. Chan, J. J. Senkevich, J. D. Joannopoulos, M. Soljačić, and I. Celanovic, "Recent developments in high-temperature photonic crystals for energy conversion," *Energy & Environmental Science*, vol. 5, no. 10, pp. 8815–8823, 2012.

[144] V. Rinnerbauer, Y. X. Yeng, W. R. Chan, J. J. Senkevich, J. D. Joannopoulos, M. Soljačić, and I. Celanovic, "High-temperature stability and selective thermal emission of polycrystalline tantalum photonic crystals," *Optics Express*, vol. 21, no. 9, pp. 11 482–11 491, 2013.

[145] Y. Fink, J. N. Winn, S. Fan, C. Chen, J. Michel, J. D. Joannopoulos, and E. L. Thomas, "A dielectric omnidirectional reflector," *Science*, vol. 282, no. 5394, pp. 1679–1682, 1998.

[146] B. G. Bovard, "Rugate filter theory: an overview," *Applied Optics*, vol. 32, no. 28, pp. 5427–5442, 1993.

[147] R. Black, P. Baldasaro, and G. Charache, "Thermophotovoltaics-development status and parametric considerations for power applications," in *Thermoelectrics, 1999. Eighteenth International Conference on.* IEEE, 1999, pp. 639–644.

[148] A. Heinzel, V. Boerner, A. Gombert, B. Bläsi, V. Wittwer, and J. Luther, "Radiation filters and emitters for the nir based on periodically structured metal surfaces," *Journal of Modern Optics*, vol. 47, no. 13, pp. 2399–2419, 2000.

[149] U. Ortabasi and B. Bovard, "Rugate technology for thermophotovoltaic (TPV) applications: a new approach to near perfect filter performance," in *AIP Conference Proceedings*, vol. 653, no. 1. AIP, 2003, pp. 249–258.

[150] F. OSullivan, I. Celanovic, N. Jovanovic, J. Kassakian, S. Akiyama, and K. Wada, "Optical characteristics of one-dimensional Si/ SiO_2 photonic crystals for thermophotovoltaic applications," *Journal of Applied Physics*, vol. 97, no. 3, p. 033529, 2005.

[151] T. D. Rahmlow Jr, D. M. DePoy, P. M. Fourspring, H. Ehsani, J. E. Lazo-Wasem, and E. J. Gratrix, "Development of front surface, spectral control filters with greater temperature stability for thermophotovoltaic energy conversion," in *AIP Conference Proceedings*, vol. 890, no. 1. AIP, 2007, pp. 59–67.

[152] B. Wernsman, R. R. Siergiej, S. D. Link, R. G. Mahorter, M. N. Palmisiano, R. J. Wehrer, R. W. Schultz, G. P. Schmuck, R. L. Messham, S. Murray *et al.*, "Greater than 20% radiant heat conversion efficiency of a thermophotovoltaic radiator/module system using reflective spectral control," *IEEE Transactions on Electron Devices*, vol. 51, no. 3, pp. 512–515, 2004.

[153] P. Bermel, W. Chan, Y. X. Yeng, J. D. Joannopoulos, M. Soljacic, and I. Celanovic, "Design and global optimization of high-efficiency thermophotovoltaic systems," in *THERMO PHOTOVOLTAIC GENERATION OF ELECTRICITY TPV-9 CONFERENCE 2010*, 2010, pp. 1–6.

[154] A. Meulenberg and K. Sinha, "Spectral selectivity from resonant-coupling in microgap-TPV," *arXiv preprint arXiv:0911.0860*, 2009.

[155] M. Francoeur, R. Vaillon, and M. P. Mengüç, "Thermal impacts on the performance of nanoscale-gap thermophotovoltaic power generators," *IEEE Transactions on Energy Conversion*, vol. 26, no. 2, pp. 686–698, 2011.

[156] Y. Guo, S. Molesky, H. Hu, C. L. Cortes, and Z. Jacob, "Thermal excitation of plasmons for near-field thermophotovoltaics," *Applied Physics Letters*, vol. 105, no. 7, p. 073903, 2014.

[157] A. Taflove and S. C. Hagness, *Computational electrodynamics: the finite-difference time-domain method*. Artech house, 2005.

[158] N.-P. Harder and M. A. Green, "Thermophotonics," *Semiconductor Science and Technology*, vol. 18, no. 5, p. S270, 2003.

[159] J. B. Chou, Y. X. Yeng, Y. E. Lee, A. Lenert, V. Rinnerbauer, I. Celanovic, M. Soljačić, N. X. Fang, E. N. Wang, and S.-G. Kim, "Enabling ideal selective solar absorption with 2d metallic dielectric photonic crystals," *Advanced Materials*, vol. 26, no. 47, pp. 8041–8045, 2014.

[160] Y. X. Yeng, J. B. Chou, V. Rinnerbauer, Y. Shen, S.-G. Kim, J. D. Joannopoulos, M. Soljacic, and I. Čelanović, "Global optimization of omnidirectional wavelength selective emitters/absorbers based on dielectric-filled anti-reflection coated two-dimensional metallic photonic crystals," *Optics Express*, vol. 22, no. 18, pp. 21 711–21 718, 2014.

[161] Q. Chen, P. Bermel, R. Shugayev, M. Sumino, Z. Zhiguang, O. R. Yehia, and E. L. Schlenker, "TPV efficiency simulation," Nov 2013. [Online]. Available: https://nanohub.org/resources/tpvtest

[162] A. Mathur, E. S. Sakr, and P. Bermel, "TPXSIM: a modeling tool for high efficiency thermophotovoltaic systems," 2014.

[163] A. F. Oskooi, D. Roundy, M. Ibanescu, P. Bermel, J. D. Joannopoulos, and S. G. Johnson, "MEEP: A flexible free-software package for electromagnetic simulations by the FDTD method," *Computer Physics Communications*, vol. 181, no. 3, pp. 687–702, 2010.

[164] C. K. Carniglia, "Comparison of several shortwave pass filter designs," *Applied Optics*, vol. 28, no. 14, pp. 2820–2823, 1989.

[165] S. Roberts, "Optical properties of nickel and tungsten and their interpretation according to drude's formula," *Physical Review*, vol. 114, no. 1, p. 104, 1959.

[166] E. Eckert and E. Sparrow, "Radiative heat exchange between surfaces with specular reflection," *International Journal of Heat and Mass Transfer*, vol. 3, no. 1, pp. 42–54, 1961.

[167] T. Abendroth, H. Althues, G. Mäder, P. Härtel, S. Kaskel, and E. Beyer, "Selective absorption of carbon nanotube thin films for solar energy applications," *Solar Energy Materials and Solar Cells*, vol. 143, pp. 553–556, 2015.

[168] Z. Zhou, O. Yehia, and P. Bermel, "Integrated photonic crystal selective emitter for thermophotovoltaics," *Journal of Nanophotonics*, vol. 10, no. 1, p. 016014, 2016.

[169] E. Sakr, Z. Zhou, and P. Bermel, "Enhancing selectivity of infrared emitters through quality-factor matching," in *Infrared Remote Sensing and Instrumentation XXIII*, vol. 9608. International Society for Optics and Photonics, 2015, p. 960819.

[170] P. Bermel, J. Lee, J. D. Joannopoulos, I. Celanovic, and M. Soljacie, "Selective solar absorbers," *Annual Review of Heat Transfer*, vol. 15, no. 15, 2012.

[171] V. Liu and S. Fan, "S4: A free electromagnetic solver for layered periodic structures," *Computer Physics Communications*, vol. 183, no. 10, pp. 2233–2244, 2012.

[172] H. Mousazadeh, A. Keyhani, A. Javadi, H. Mobli, K. Abrinia, and A. Sharifi, "A review of principle and sun-tracking methods for maximizing solar systems output," *Renewable and Sustainable Energy Reviews*, vol. 13, no. 8, pp. 1800–1818, 2009.

[173] E. L. Schlenker, Z. Zhiguang, P. Bermel, H. Chung, and H. Chung, "Thermophotovoltaic experiment," Sep 2015. [Online]. Available: https://nanohub.org/resources/tpvexpt

[174] M. A. Green, E. D. Dunlop, D. H. Levi, J. Hohl-Ebinger, M. Yoshita, and A. W. Ho-Baillie, "Solar cell efficiency tables (version 54)," *Progress in Photovoltaics: Research and Applications*, vol. 27, no. 7, pp. 565–575, 2019.

[175] J.-H. Lee, Y.-S. Kim, K. Constant, and K.-M. Ho, "Woodpile metallic photonic crystals fabricated by using soft lithography for tailored thermal emission," *Advanced Materials*, vol. 19, no. 6, pp. 791–794, 2007.

[176] L. Wang, S. Basu, and Z. Zhang, "Direct measurement of thermal emission from a Fabry-Perot cavity resonator," *Journal of Heat Transfer*, vol. 134, no. 7, p. 072701, 2012.

[177] F. Marquier, K. Joulain, J.-P. Mulet, R. Carminati, J.-J. Greffet, and Y. Chen, "Coherent spontaneous emission of light by thermal sources," *Physical Review B*, vol. 69, no. 15, p. 155412, 2004.

[178] X. Wang, J. Jian, Z. Zhou, C. Fan, Y. Dai, L. Li, J. Huang, J. Sun, A. Donohue, P. Bermel, X. Zhang, H.-T. Chen, and H. Wang, "Self-assembled ag–tin hybrid plasmonic metamaterial: Tailorable tilted nanopillar and optical properties," *Advanced Optical Materials*, p. 1801180, 2018.

[179] F. Cao, K. McEnaney, G. Chen, and Z. Ren, "A review of cermet-based spectrally selective solar absorbers," *Energy & Environmental Science*, vol. 7, no. 5, pp. 1615–1627, 2014.

[180] F. Cao, D. Kraemer, T. Sun, Y. Lan, G. Chen, and Z. Ren, "Enhanced thermal stability of w-ni-al2o3 cermet-based spectrally selective solar absorbers with tungsten infrared reflectors," *Advanced Energy Materials*, vol. 5, no. 2, p. 1401042, 2015.

[181] H. Wang, H. Alshehri, H. Su, and L. Wang, "Design, fabrication and optical characterizations of large-area lithography-free ultrathin multilayer selective solar coatings with excellent thermal stability in air," *Solar Energy Materials and Solar Cells*, vol. 174, pp. 445–452, 2018.

[182] P. Li, B. Liu, Y. Ni, K. K. Liew, J. Sze, S. Chen, and S. Shen, "Large-scale nanophotonic solar selective absorbers for high-efficiency solar thermal energy conversion," *Advanced Materials*, vol. 27, no. 31, pp. 4585–4591, 2015.

[183] D. Woolf, J. Hensley, J. Cederberg, D. Bethke, A. Grine, and E. Shaner, "Heterogeneous metasurface for high temperature selective emission," *Applied Physics Letters*, vol. 105, no. 8, p. 081110, 2014.

[184] H. Wang, V. P. Sivan, A. Mitchell, G. Rosengarten, P. Phelan, and L. Wang, "Highly efficient selective metamaterial absorber for high-temperature solar thermal energy harvesting," *Solar Energy Materials and Solar Cells*, vol. 137, pp. 235–242, 2015.

[185] D. Kraemer, B. Poudel, H.-P. Feng, J. C. Caylor, B. Yu, X. Yan, Y. Ma, X. Wang, D. Wang, A. Muto, K. McEnaney, M. Chiesa, Z. Ren, and G. Chen, "High-performance flat-panel solar thermoelectric generators with high thermal concentration," *Nature Materials*, vol. 10, no. 7, p. 532, 2011.

[186] A. Datas and A. Martí, "Thermophotovoltaic energy in space applications: Review and future potential," *Solar Energy Materials and Solar Cells*, vol. 161, pp. 285–296, 2017.

[187] P. N. Dyachenko, S. Molesky, A. Y. Petrov, M. Störmer, T. Krekeler, S. Lang, M. Ritter, Z. Jacob, and M. Eich, "Controlling thermal emission with refractory epsilon-near-zero metamaterials via topological transitions," *Nature Communications*, vol. 7, p. 11809, 2016.

[188] A. Donnadieu and B. Seraphin, "Optical performance of absorber-reflector combinations for photothermal solar energy conversion," *Journal of the Optical Society of America*, vol. 68, no. 3, pp. 292–297, 1978.

[189] J. Gittleman, E. Sichel, H. Lehmann, and R. Widmer, "Textured silicon: a selective absorber for solar thermal conversion," *Applied Physics Letters*, vol. 35, no. 10, pp. 742–744, 1979.

[190] J. Poortmans and V. Arkhipov, *Thin film solar cells: fabrication, characterization and applications*. John Wiley & Sons, Chichester, 2006, vol. 5.

[191] J. C. Sturm and K. H. Chung, "Chemical vapor deposition epitaxy of silicon-based materials using neopentasilane," *ECS Transactions*, vol. 16, no. 10, pp. 799–805, 2008.

[192] D. L. Chubb, D. S. Wolford, A. Meulenberg, and R. S. DiMatteo, "Semiconductor silicon as a selective emitter," in *AIP Conference Proceedings*, vol. 653, no. 1. AIP, 2003, pp. 174–200.

[193] S. Wang, B. D. Weil, Y. Li, K. X. Wang, E. Garnett, S. Fan, and Y. Cui, "Large-area free-standing ultrathin single-crystal silicon as processable materials," *Nano letters*, vol. 13, no. 9, pp. 4393–4398, 2013.

[194] H. Reddy, U. Guler, A. V. Kildishev, A. Boltasseva, and V. M. Shalaev, "Temperature-dependent optical properties of gold thin films," *Optical Materials Express*, vol. 6, no. 9, pp. 2776–2802, 2016.

[195] H. Reddy, U. Guler, K. Chaudhuri, A. Dutta, A. V. Kildishev, V. M. Shalaev, and A. Boltasseva, "Temperature-dependent optical properties of single crystalline and polycrystalline silver thin films," *ACS Photonics*, vol. 4, no. 5, pp. 1083–1091, 2017.

[196] J. Kischkat, S. Peters, B. Gruska, M. Semtsiv, M. Chashnikova, M. Klinkmüller, O. Fedosenko, S. Machulik, A. Aleksandrova, G. Monastyrskyi, Y. Flores, and W. T. Masselink, "Mid-infrared optical properties of thin films of aluminum oxide, titanium dioxide, silicon dioxide, aluminum nitride, and silicon nitride," *Applied Optics*, vol. 51, no. 28, pp. 6789–6798, 2012.

[197] F. Roozeboom, *Advances in Rapid Thermal and Integrated Processing*. Springer Science & Business Media, Dordrecht, 2013, vol. 318.

[198] J. R. Wilcox, A. W. Haas, J. L. Gray, and R. J. Schwartz, "Estimating saturation current based on junction temperature and bandgap," in *AIP Conference Proceedings*, vol. 1407, no. 1. AIP, 2011, pp. 30–33.

[199] P. Bermel, K. Yazawa, J. Gray, X. Xu, and A. Shakouri, "Hybrid strategies and technologies for full spectrum solar conversion," *Energy & Environmental Science*, vol. 9, no. 9, pp. 2776–2788, 2016.

[200] H. Zhang, J. Baeyens, J. Degrève, and G. Cacères, "Concentrated solar power plants: Review and design methodology," *Renewable and Sustainable Energy Reviews*, vol. 22, pp. 466–481, 2013.

[201] N. Cordero, R. Ginige, B. Corbett, and K. Kennedy, "Thermal modelling of tpv systems," in *The Eighth Intersociety Conference on Thermal and Thermomechanical Phenomena in Electronic Systems, 2002. ITHERM 2002.* IEEE, 2002, pp. 605–609.

[202] W. Shockley and H. J. Queisser, "Detailed balance limit of efficiency of p-n junction solar cells," *Journal of Applied Physics*, vol. 32, no. 3, pp. 510–519, 1961.

[203] "ATRAN," 1992. [Online]. Available: https://atran.sofia.usra.edu/cgibin/atran/atran.cgi

[204] M. Rubin, "Optical properties of soda lime silica glasses," *Solar Energy Materials*, vol. 12, pp. 275–288, 1985.

[205] X. Sun, Y. Sun, Z. Zhou, M. A. Alam, and P. Bermel, "Radiative sky cooling: fundamental physics, materials, structures, and applications," *Nanophotonics*, vol. 6, no. 5, pp. 997–1015, 2017.

[206] J.-l. Kou, Z. Jurado, Z. Chen, S. Fan, and A. J. Minnich, "Daytime radiative cooling using near-black infrared emitters," *ACS Photonics*, vol. 4, no. 3, pp. 626–630, 2017.

[207] Y. Lu, Z. Chen, L. Ai, X. Zhang, J. Zhang, J. Li, W. Wang, R. Tan, N. Dai, and W. Song, "A universal route to realize radiative cooling and light management in photovoltaic modules," *Solar RRL*, vol. 1, no. 10, p. 1700084, 2017.

[208] Y. Zhai, Y. Ma, S. N. David, D. Zhao, R. Lou, G. Tan, R. Yang, and X. Yin, "Scalable-manufactured randomized glass-polymer hybrid metamaterial for daytime radiative cooling," *Science*, vol. 355, no. 6329, pp. 1062–1066, 2017.

[209] E. Sakr and P. Bermel, "Angle-selective reflective filters for exclusion of background thermal emission," *Physical Review Applied*, vol. 7, no. 4, p. 044020, 2017.

[210] B. Bhatia, A. Leroy, Y. Shen, L. Zhao, M. Gianello, D. Li, T. Gu, J. Hu, M. Soljačić, and E. N. Wang, "Passive directional sub-ambient daytime radiative cooling," *Nature Communications*, vol. 9, no. 1, p. 5001, 2018.

[211] A. Gentle, J. Aguilar, and G. Smith, "Optimized cool roofs: Integrating albedo and thermal emittance with R-value," *Solar Energy Materials and Solar Cells*, vol. 95, no. 12, pp. 3207–3215, 2011.

[212] K. Zhang, D. Zhao, X. Yin, R. Yang, and G. Tan, "Energy saving and economic analysis of a new hybrid radiative cooling system for single-family houses in the usa," *Applied Energy*, vol. 224, pp. 371–381, 2018.

[213] E. A. Goldstein, A. P. Raman, and S. Fan, "Sub-ambient non-evaporative fluid cooling with the sky," *Nature Energy*, vol. 2, no. 9, p. 17143, 2017.

[214] S. Byrnes, R. Blanchard, and F. Capasso, "Harvesting renewable energy from earth's mid-infrared emissions." *Proceedings of the National Academy of Sciences of the United States of America*, vol. 111, no. 11, pp. 3927–3932, 2014.

[215] M. Zhou, H. Song, X. Xu, A. Shahsafi, Z. Xia, Z. Ma, M. Kats, J. Zhu, B. S. Ooi, Q. Gan, and Z. Yu, "Accelerating vapor condensation with daytime radiative cooling," *arXiv preprint arXiv:1804.10736*, 2018.

[216] H. Kim, S. R. Rao, E. A. Kapustin, L. Zhao, S. Yang, O. M. Yaghi, and E. N. Wang, "Adsorption-based atmospheric water harvesting device for arid climates," *Nature Communications*, vol. 9, no. 1, p. 1191, 2018.

[217] C. Honsberg and S. Bowden, "PVEDUCATION," Dec 2018. [Online]. Available: http://pveducation.org/pvcdrom/solar-cell-operation/effect-of-temperature

[218] P. Hacke, S. Spataru, K. Terwilliger, G. Perrin, S. Glick, S. Kurtz, and J. Wohlgemuth, "Accelerated testing and modeling of potential-induced degradation as a function of temperature and relative humidity," *IEEE Journal of Photovoltaics*, vol. 5, no. 6, pp. 1549–1553, 2015.

[219] H.-J. Hagemann, W. Gudat, and C. Kunz, "Optical constants from the far infrared to the x-ray region: Mg, al, cu, ag, au, bi, c, and al 2 o 3," *Journal of Optical Society of America*, vol. 65, no. 6, pp. 742–744, 1975.

[220] J. S. Stein, W. F. Holmgren, J. Forbess, and C. W. Hansen, "Pvlib: Open source photovoltaic performance modeling functions for matlab and python," in *2016 ieee 43rd photovoltaic specialists conference (pvsc)*. IEEE, 2016, pp. 3425–3430.

[221] A. Berk, L. S. Bernstein, and D. C. Robertson, "Modtran: A moderate resolution model for lowtran," SPECTRAL SCIENCES INC BURLINGTON MA, Tech. Rep., 1987.

[222] A. Ndiaye, A. Charki, A. Kobi, C. M. Kébé, P. A. Ndiaye, and V. Sambou, "Degradations of silicon photovoltaic modules: A literature review," *Solar Energy*, vol. 96, pp. 140–151, 2013.

[223] T. Silverman, M. Deceglie, and K. Horowitz, "NREL comparative PV LCOE calculator," 2018. [Online]. Available: http://pvlcoe.nrel.gov

[224] H. Wu, D. Kong, Z. Ruan, P.-C. Hsu, S. Wang, Z. Yu, T. J. Carney, L. Hu, S. Fan, and Y. Cui, "A transparent electrode based on a metal nanotrough network," *Nature Nanotechnology*, vol. 8, no. 6, p. 421, 2013.

[225] D. Chen, "Anti-reflection (ar) coatings made by sol–gel processes: a review," *Solar Energy Materials and Solar Cells*, vol. 68, no. 3-4, pp. 313–336, 2001.

VITA

Education and Experience

Purdue University, West Lafayette, IN, 2013 - 2019

Ph.D., Dept. of Electrical and Computer Engineering (advisor: Peter A. Bermel), GPA 3.97/4.0.

- Studied nanophotonic designs for power generation technologies including solar cells and thermophotovoltaics.
- Developed experimental techniques to characterize high-temperature properties of nanophotonic structures.
- Developed experimental demonstration of novel passive cooling techniques.
- Hands-on PV Experience program at NREL (13 students across the U.S.).
- Bilsland Dissertation Fellowship.
- Tutored undergraduate and graduate students in research.

Fudan University, Shanghai, China, 2009 - 2013

B.S., Dept. of Physics, GPA 3.7/4.0.

- Senior Thesis: Thermal expansion measurement of graphene by high-temperature Raman spectroscopy.
- Outstanding Student (1 student per department annually).

Publications and Conference Talks

- S. Jin, Z. Zhou, E. S. A. Sakr, M. Motlag, X. Huang, L. Tong, P. Bermel, L. Ye, and G. J. Cheng, "Scalable nanoshaping of hierarchical metallic patterns with multiplex laser shock imprinting using soft optical disks," Small, vol. 15, no. 18, p. 1900481, 2019.
- Z. Zhou, Z. Wang, and P. Bermel, "Radiative cooling for low-bandgap photovoltaics under concentrated sunlight," Optics express, vol. 27, no. 8, pp. A404-A418, 2019.
- X. Wang, J. Jian, Z. Zhou, C. Fan, Y. Dai, L. Li, J. Huang, J. Sun, A. Donohue, P. Bermel et al., "Self-assembled Ag-TiN hybrid plasmonic metamaterial: Tailorable tilted nanopillar and optical properties," Advanced Optical Materials, vol. 7, no. 3, p. 1801180, 2019.
- Z. Zhou, E. Sakr, and P. Bermel, "Modeling non-equilibrium thermal radiation phenomena using a direct simulation method," in APS Meeting Abstracts, 2018.
- Z. Zhou, X. Sun, Y. Sun, M. A. Alam, and P. Bermel, "Optical modeling and characterization of radiative cooling for solar energy applications," in Optics for Solar Energy. Optical Society of America, 2017, pp. RTh1B-1.
- Y. Sun, Z. Zhou, X. Jin, X. Sun, M. A. Alam, and P. Bermel, "Radiative cooling for concentrating photovoltaic systems," in Thermal Radiation Management for Energy Applications, vol. 10369. International Society for Optics and Photonics, 2017, p. 103690D.
- X. Sun, Y. Sun, Z. Zhou, M. A. Alam, and P. Bermel, "Radiative sky cooling: fundamental physics, materials, structures, and applications," Nanophotonics, vol. 6, no. 5, pp. 997-1015, 2017.
- H. Chung, Z. Zhou, and P. Bermel, "Collimated thermal radiation transfer via half Maxwell's fish-eye lens for thermophotovoltaics," Applied Physics Letters, vol. 110, no. 20, p. 201111, 2017.

- H. Tian, Z. Zhou, T. Liu, C. Karina, U. Guler, V. Shalaev, and P. Bermel, "High temperature efficient, stable Si wafer-based selective solar absorbers," Applied Physics Letters, vol. 110, no. 14, p. 141101, 2017.
- X. Sun, T. J. Silverman, Z. Zhou, M. R. Khan, P. Bermel, and M. A. Alam, "Optics-based approach to thermal management of photovoltaics: selective-spectral and radiative cooling," IEEE Journal of Photovoltaics, vol. 7, no. 2, pp. 566-574, 2017.
- Z. Zhou, X. Sun, and P. Bermel, "Radiative cooling for thermophotovoltaic systems," in Infrared Remote Sensing and Instrumentation XXIV, vol. 9973. International Society for Optics and Photonics, 2016, p. 997308.
- Z. Zhou, E. Sakr, Y. Sun, and P. Bermel, "Solar thermophotovoltaics: reshaping the solar spectrum," Nanophotonics, vol. 5, no. 1, pp. 1-21, 2016.
- Z. Zhou, O. Yehia, and P. Bermel, "Integrated photonic crystal selective emitter for thermophotovoltaics," Journal of Nanophotonics, vol. 10, no. 1, p. 016014, 2016.
- Z. Zhou, E. Sakr, O. Yehia, A. Mathur, and P. Bermel, "Photonic crystal selective structures for solar thermophotovoltaics," MRS Advances, vol. 1, no. 59, pp. 3883-3889, 2016.
- E. Sakr, Z. Zhou, and P. Bermel, "Enhancing selectivity of infrared emitters through quality-factor matching," in Infrared Remote Sensing and Instrumentation XXIII, vol.9608. International Society for Optics and Photonics, 2015, p.960819.
- Z. Zhou, Q. Chen, and P. Bermel, "Prospects for high-performance thermophotovoltaic conversion efficiencies exceeding the Shockley-Queisser limit," Energy Conversion and Management, vol. 97, pp. 63-69, 2015.
- E. Sakr, Z. Zhou, and P. Bermel, "High efficiency rare-earth emitter for thermophotovoltaic applications," Applied Physics Letters, vol. 105, no. 11, p.111107, 2014.

Skills

- **Fabrication:** Electron Beam Evaporation, Sputtering, Pulse Laser Deposition (PLD), Plasma Enhanced Chemical Vapor Deposition (PECVD), Interference Lithography, Photolithography, Etching, Wafer Bonding, Wire Bonding.
- **Characterization:** Scanning Electron Microscope (SEM), Electrical Device Measurement (I-V), External Quantum Efficiency (EQE), Fourier Transform Infrared Spectroscopy (FTIR), UV-VIS-NIR Spectrophotometry.
- **General:** High Vacuum Technology, Cleanroom Processing.
- **Programming:** MATLAB, Python, C, Scheme.
- **Software packages:** MEEP, S4, SOLIDWORKS, Origin.